Double Drell-Yan measurement, heavy Higgs searches in the four leptons final state and forward muons performance with the ATLAS detector

The University Of Sheffield.

Dimitrios N. Kyriazopoulos

Department of Physics and Astronomy

The University of Sheffield

A thesis submitted in fulfilment for the degree of

Doctor of Philosophy

July 2016

Abstract

In this thesis, physics studies are presented using data collected by the ATLAS detector at CERN on 2012 corresponding to L = 20.3 fb^{-1}, at the LHC $\sqrt{s}$ = 8 TeV. The studies performed refer to the identification of events in final states with two Z bosons decaying to four leptons (electrons, muons). Furthermore, the effect of QED radiative corrections in the $Z \to \ell\ell$ process and the muon reconstruction efficiency in the forward region of the ATLAS detector have been studied.

The first study is the cross-section of the Double Drell-Yan process $Z + Z \to 4l$. The cross-section is measured to be $0.74^{+0.51}_{-0.44}(\text{stat.})^{+0.21}_{-0.14}(\text{syst.})$ fb. Due to the large uncertainties a 95% CL upper limit in the cross-section is set of 1.54 fb . This result is converted to a 95% CL lower limit on the phenomelogical factor σ_{eff} of 0.38 mb.

The second study is the search for an additional heavy Higgs boson in the $H \to ZZ \to 4l$ final state. The search is performed in the mass range between 140 - 1000 TeV. No significant excess in data with respect to the background expectations are observed, and upper limits are set on the production cross-sections for all the mass points. The cross-section × branching ratio limits are extracted independently for the gluon-gluon fusion (ggF) and vector-boson fusion (VBF) production mechanisms.

Additionally, the effect of non-collinear QED radiative corrections is examined in the H $\to$ ZZ $\to$ $4l$. QED Final State Radiation (FSR) of leptons originating from Z bosons is reconstructed focusing on non-collinear radiation from the lepton ($\Delta R_{(lep,photon)} > 0.15$). The photons are reconstructed with high efficiency ($\approx$ 60%) and purity (> 95%) looking at $Z \to \mu^+\mu^-$ and $Z \to e^+e^-$ events in the 2012 data. At the ATLAS Run-I 2012 $H \to ZZ^{(*)} \to 4l$ mass measurement, 2 out of 30 Higgs candidates in the signal window (120-130 GeV) had their final invariant mass corrected for non-collinear FSR effects.

Lastly, the reconstruction performance of muons in the forward pseudorapidity region of the detector is examined in the 2012 data $Z \to \mu^+\mu^-$ decays. The study focuses on the region $2.5 < |\eta| < 2.7$. The reconstruction efficiency is at the level of > 90%. Efficiency scale factors are extracted which are used to correct the simulation of the muon behaviour at this part of the detector, in order to match data observations.

Acknowledgements

Reaching the end of my doctoral studies, I am thankful to my supervisor Christos Anastopoulos for making the final years of the PhD a very useful experience. I am grateful for everything he has transmitted to me. Also, I would like to thank the people who made this PhD possible: Prof Stathes Paganis (Sheffield, now Taiwan) and Prof Chara Petridou (Thessaloniki). Their encouragement and provision of financial support was essential for me undertaking the doctoral researcher experience.

I would like to thank the Sheffield-ATLAS group (aka ShATLAS): Prof Dan Tovey, Prof Davide Constanzo, Mark Hodgkinson, Paul Hodgson, Elena Korokolva, Paul Miyagawa and Kerim Suruliz. Special thanks to: Ian Dawson for the enthusiasm regarding Double Parton Interactions, Tulay Cuhadar for the induction to ATLAS FSR algorithm, Matt Robinson for constant IT support. From the ATLAS collaboration, my special thanks to Rosy Nicolaidou and Dinos Bachas for the work we conducted on the forward muons. Thank you also to Nick Edwards for his help regarding the heavy Higgs search. I would like to thank also Frank Krauss from Durham University for his theoretical insight in the Double Parton Interactions.

I am also grateful to Richard French for the opportunity to work on hardware systems and to Hector Marin-Reyes for introducing me to the wonderful world of electronics. For all the ATLAS and non-ATLAS D35 people: Brais, Jon, Kerry, Gary, Calum, Andy, Ed, Steve, Sam; thank you for the help, friendship, endless politics discussions and all the ROOT help! Gracias, thank you, Ta! For all these years in Sheffield, I would like to heartily thank all the people who made me find a spiritual home in a foreign country. A big thank you to Fr Edwin and Susan, Jonathan and Catalina, Tatiana and John, Pavlo, Ivan, Vlad, Maria, Stathis, Alice and family. The welcoming community enviroment was a great support in many challenging times. For my good friends, Christos, Pavlos, Christos and Giorgos. "Game over" κύριοι!. Thank you for bearing all of my complaints these years and giving me courage every time I needed it.

I would not have been in this position without the help and support of my parents, Nikolaos and Evangelia. It was a completely new experience for them having me so far away and I hope it was not a stressful one! And to my siblings: Fenia, Maria, Damos, Pavlos, Stella, Elisavet, Nestoras, Katerina, Xaris, Loukia, Myrto. Thank you so much for managing to keep the home spirit alive every time we were talking! Σας ευχαριστώ πάρα πολύ!

For my very beloved wife Ruxandra, to whom I dedicate this thesis. Pentru tine scumpa mea, lumina și bucuria din viața mea! You gave me hope and made me re-discover life in a very difficult moment. Nothing would have been possible without your constant support and help. Your fresh and wondeful thoughts gave me so much love and courage to go on. Waiting now for the arrival of our first child, I thank you again for all the miracles you brought to my life, draga mea.

Sheffield, Christmas 2015

Τὰ γὰρ ἀόρατα αὐτοῦ ἀπὸ κτίσεως κόσμου τοῖς ποιήμασιν νοούμενα καθορᾶται (Προς Ρωμαίους 1,20)

For the invisible things of Him from the creation of the world are clearly seen, being understood by the things that are made (Romans 1:20)

Waiting for you, our little Anna, to appear in our world has been a wonderful journey...
Now that you are with us, we feel so blessed that we have you!

Πᾶσα δόσις ἀγαθὴ καὶ πᾶν δώρημα τέλειον ἄνωθέν ἐστι καταβαῖνον ἀπὸ τοῦ πατρὸς τῶν φώτων. (Ιακώβου 1,17)

Every good and perfect gift is from above, coming down from the Father of the heavenly lights.(James 1:17)

Contents

List of Figures

List of Tables

Thesis synopsis

The first run of the Large Hadron Collider (2009-2012) was characterised by the excellent conditions of the accelarator and the corresponding detectors. The ATLAS Experiment accumulated a significant amount of data which benefitted from the performance of the sub-detector systems and led, among other important contributions in Particle Physics, to the discovery of the Higgs boson in 2012. Operating already after a 3-years long upgrade phase, LHC and ATLAS are investigating unexplored energy regimes, aiming to set new directions in our understanding of the microcosm.

The data recorded during the last period of the Run-I in 2012 are the basic constituent of this thesis. Firstly, the muon reconstruction efficiency of the ATLAS Muon spectrometer is examined, on the forward region of the detector. Next, the effect of particular QED radiative corrections on the $Z \to \ell\ell$ and the $H \to ZZ^{(*)} \to 4l$ processes is shown. Finally, two separate physics analyses are presented which involve the final state of four leptons as decay products of two Z bosons. These are the measurement of the exclusive cross-section for the Double Drell-Yan process and the search for an additional heavy Higgs boson. The outline and structure of the thesis follows.

Chapter 1 contains a short introduction to the theoretical framework of Particle Physics. The Standard Model (SM) is described and the concept of gauge invariance and symmetries is discussed. The electroweak symmetry breaking and the Higgs mechanism are introduced with description about the properties of the Higgs boson. Also, the Double Parton Interactions are introduced in this chapter.

Chapter 2 details the Large Hadron Collider and the ATLAS detector. The main sub-detector systems of ATLAS are featured. The reconstruction of the physics objects follows on Chapter 3.

Chapter 4 outlines the forward muons reconstruction efficiency in ATLAS. The Muon Spectrometer instrumentation in the forward pseudorapidity region ($2.5 < |\eta| < 2.7$) is used for the performance study of the forward muons. The $Z \to \mu^+\mu^-$ channel was used in both data and simulation in order to quantify the reconstruction efficiency. Finally, the corrections were applied on the simulation to match the experimental observations.

The non-collinear QED radiative corrections are described in Chapter 5. The study was performed on $Z \to \mu^+\mu^-$ and $Z \to e^+e^-$ decay on the 2012 data. A Final State Radiation recon-

struction algorithm was applied and the effect in the invariant mass correction of Z boson decays is presented. The chapter finishes with the impact of the correction in the $H \to ZZ^{(*)} \to 4l$ 2012 mass measurement.

The cross-section measurement of the Double Drell-Yan process is the topic of Chapter 6. The analysis studies $Z+Z \to \ell\ell\ell\ell$, decays which originate from Double Parton Interaction. Observables with strong discrimination power between signal and background are constructed and an unbinned maximum likelihood fit is performed in order to calculate the cross-section. Additionally, an upper limit in the cross-section is set and linked to lower limit in the value of the phenomenological factor (σ_{eff}) which describes the multiparton interaction. Also, the prospects of the measurement are presented for higher collision energies and luminosities.

Chapter 7 details the search for an additional heavy Higgs boson in the $H \to ZZ^{(*)} \to 4l$ decay channel. A search is performed in a wide mass range for heavy Higgs-like boson which is postulated by extensions of the Standard Model. The analysis uses the same framework as the low mass SM Higgs. Upper limits are set on the production cross-section having as reference the SM predictions.

Chapter 1

Introduction to the Standard Model of Particle Physics

The theoretical framework for elementary Particle Physics is known as the "Standard Model" . The Standard Model (SM) is a relativistic quantum field theory which describes the properties and the interactions of the elementary particles.

Based on the properties of a relativistic quantum field theory, particles and antiparticles, correspond to excitations of fields which exist around in space. There are two kinds of fields: The matter fields describing the *fermions* and the gauge fields, describing the force carriers, the *bosons*. All the particles assumed by the Standard Model are shown in Figure 1.1. The separation between the two fields is based on the quantum number which describes an intrinsic form of angular momentum, the *spin*. The fermions have half-integer spin whereas the bosons have an integer value.

The fermionic fields are split into two categories. Those which carry only electric and weak charge, the *leptons*, and those which carry electric, weak and color charge, the *quarks*.

The leptons and quarks interact either with the weak or the electromagnetic force which is described by the Electroweak theory developed by Glashow, Weinberg and Salam (GWS model) [2, 3, 4], based on the gauge symmetry group, $SU(2)_L \times U(1)_Y$.

Additionally, the quarks interact due to the color charge through the strong force. This interaction is represented by $SU(3)_C$ color symmetry group and based on the works of Politzer, Wilczek and Gross.[5, 6, 7, 8]

1.1 The Gauge principle in the Standard Model

The development of the Standard Model, has been based on the idea that a symmetry which is related to a transformation corresponds to a conserved quantity, as Noether's theorem states [9]. Therefore, the interaction of particles is connected to groups of transformations symme-

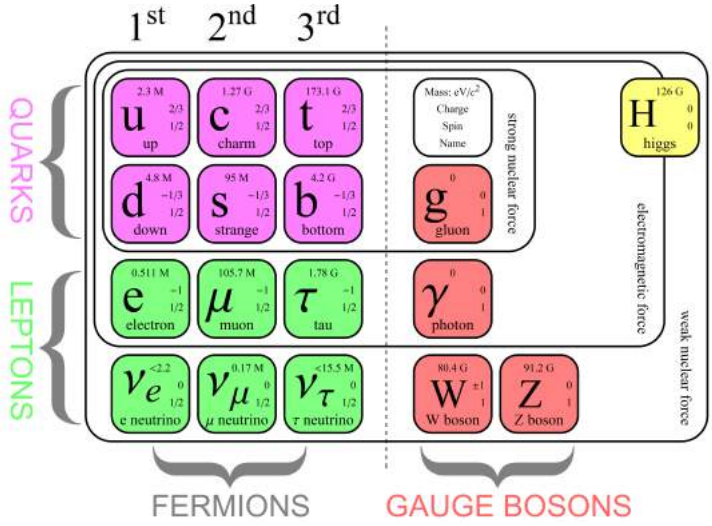

Figure 1.1: The Standard Model particles. Figure from [1]

tries of the Lagrangian. The aforementioned property constitutes a "gauge theory" for particle physics.

The gauge transformations have the form:

$$\begin{aligned} \text{Global transformation} &: \psi \rightarrow \psi' = \Theta\psi \\ \text{Local transformation} &: \psi \rightarrow \psi' = \Theta(x)\psi \end{aligned} \tag{1.1}$$

In the previous notation $\Theta(x)$ denotes an element of a gauge symmetry group. For instance, the Quantum Electrodynamics (QED) is represented by the Abelian group U(1) of 1×1 unitary matrices with complex phases. The Electroweak interaction and the Quantum Chromodynamics (QCD) though are based on the non-Abelian SU(N) groups of $N \times N$ unitary matrices.

The elements of these groups have the form:

$$\Theta(x) = e^{(i \sum_{n=1}^{N^2-1} a_n(x) T_n)}. \tag{1.2}$$

where T_n are the generators of the group. In total, there are $N^2 - 1$ generators whose commutation relations are:

$$[T_i, T_j] = i c_{ijk} T_k \tag{1.3}$$

where c_{ijk} is the structure constant of the group. For the Abelian U(1) group of QED, $c_{ijk} = 0$. For the non-Abelian SU(2) the structure constant is $\epsilon_{ijk} = \pm 1$ and the generators are the Pauli

matrices $T_i = \frac{1}{2}\tau_i$:

$$\tau_1 = \begin{pmatrix} 0 & 1 \\ 1 & 0 \end{pmatrix} \qquad \tau_2 = \begin{pmatrix} 0 & -i \\ i & 0 \end{pmatrix} \qquad \tau_3 = \begin{pmatrix} 1 & 0 \\ 0 & -1 \end{pmatrix} \tag{1.4}$$

For non-Abelian SU(3) which describes QCD the generator $T_i = \frac{1}{2}\lambda_i$, where λ_i are the eight 3x3 Gell-Mann matrices. The structure constant is $f^{\alpha\beta\gamma}$ with a summation for each index from 1 to 8.

1.1.1 Quantum Electrodynamics - QED

An application of the gauge principle is shown in the expression of the free Dirac Lagrangian density describing the electron:

$$\mathcal{L} = i\bar{\psi}\gamma^\mu\partial_\mu\psi - m\bar{\psi}\psi \tag{1.5}$$

where the ψ is the Dirac spinor for the electron with mass m and γ^μ is the set of Dirac matrices.

The Dirac Lagrangian is invariant under global transformations. In local transfomation though, the phases are chosen independently at each space-time point. The corresponding local transformation is expressed as:

$$\begin{aligned} i\bar{\psi(x)}\gamma^\mu\partial_\mu\psi(x) &\rightarrow i\bar{\psi}(x)e^{-i\alpha(x)}\gamma^\mu\partial_\mu[e^{i\alpha(x)}\psi(x)] \\ &= i\bar{\psi}(x)\gamma^\mu\partial_\mu\psi(x) - \bar{\psi}(x)\gamma^\mu\psi(x)[\partial_\mu\alpha(x)] \end{aligned} \tag{1.6}$$

The term $\partial_\mu\alpha(x)$ violates the local gauge invariance. To preserve it, the introduction of a massless vector field A_μ which transforms under $U(1)_Q$ symmetry is needed:

$$A_\mu \rightarrow A'_\mu = A_\mu - \partial_\mu\theta(x) \tag{1.7}$$

and replacing the normal derivative with the covariant derivative (D) in order to preserve the local transformation:

$$D_\mu = \partial_\mu + iqA_\mu D_\mu \rightarrow D'_\mu\psi'(x) = e^{i\theta(x)}D_\mu\psi(x) \tag{1.8}$$

where q denotes the charge.

The field strength tensor is defined as:

$$F^{\mu\nu} = \partial^\nu A^\mu - \partial^\mu A^\nu \tag{1.9}$$

which constitutes the kinematic term for the fields of the Lagrangian $-\frac{1}{4}F_{\mu\nu}F^{\mu\nu}$.

The full Lagrangian with the introduction of the covariant derivative and the kinematic

term, can be expressed in the form:

$$\begin{aligned}\mathcal{L} &= i\bar{\psi}\gamma^{\mu}D_{\mu}\psi - m\bar{\psi}\psi - \frac{1}{4}F^{\mu\nu}F_{\mu\nu} \\ &= i\bar{\psi}\gamma^{\mu}\partial_{\mu}\psi - q\bar{\psi}\gamma^{\mu}\psi A_{\mu} - m\bar{\psi}\psi - \frac{1}{4}F^{\mu\nu}F_{\mu\nu}\end{aligned} \tag{1.10}$$

Equation 1.10 expresses the interaction of a Dirac field through the electromagnetic current $J^{e\mu} \equiv q\bar{\psi}\gamma^{\mu}\psi$ with the massless vector field A_{μ}. The Equation is the Lagrangian for QED and describes the interaction of the electron (Dirac field) with the photon (γ) which is a massless vector boson associated with the vector field.

1.1.2 Quantum Chromodynamics - QCD

The Lagrangian for the description of QCD is invariant under local SU(3) transformations. It describes the interaction of three Dirac fields of equal mass with eight massless vector fields. The Dirac fields are the three colour-charges of a particular quark flavour and the vector fields correspond to the gluons.

$$\mathcal{L} = \bar{\psi}(i\gamma^{\mu}\partial_{\mu} - m)\psi + g_s(\bar{\psi}\gamma^{\mu}T_{\alpha}\psi)G^{\alpha}_{\mu} - \frac{1}{4}G^{\alpha}_{\mu\nu}G^{\mu\nu}_{\alpha} \tag{1.11}$$

where $\alpha = 1, 2, .., 8$.

The quark fields form a triplet due to the quark colour:

$$\psi = \begin{pmatrix} \psi_R \\ \psi_G \\ \psi_B \end{pmatrix}, \bar{\psi} = (\bar{\psi_R}, \bar{\psi_G}, \bar{\psi_B})$$

where each color-spinor is a four-component Dirac spinor.

The field strength tensor is denoted with $G^{\mu\nu}_{\alpha}$ which is similar to the abelian one from QED with the inclusion of coupling constant of gluons "g_s", which accounts for three and four-point self-interactions of gluons and is proportional to the structure constant $f^{\alpha\beta\gamma}$.

$$G^{\alpha}_{\mu\nu} = \partial_{\mu}G^{\alpha}_{\nu} - \partial_{\nu}G^{\alpha}_{\mu} + g_s f^{\alpha\beta\gamma}G^{b}_{\mu}G^{c}_{\nu} \tag{1.12}$$

The self-coupling of gluons is responsible for the fact that the strong force weakens in short distances or high energies due to the phenomenon of antiscreening. In QCD, the polarisation of virtual gluons in the vaccum, results in increasing the colour field and changing its colour charge, instead of cancelling (screening) like virtual quark-antiquark pairs. The effect is due to the fact that gluons apart from colour charge, carry also magnetic moment of "anti-colour". As a final result, the antiscreening effect from the virtual gluons becomes lower whilst approaching a quark. Also, the color charge of the quarks weakens in closer distances, whereas in standard conditions anti-screening prevails.[10] Similarly, this causes the quarks inside the

hadrons to behave like free particles, when probed at large enough energies. This property of the strong force is called asymptotic freedom.[5]

1.1.3 Electroweak interaction

The observation of charged-current weak interactions and neutral-current weak interactions from charged leptons, prompted the idea for a unification of the electromagnetic and weak interactions. The weak interaction involves only "left-handed" particles and "right-handed" antiparticles. Thus, it has been associated with the chirality operator to the Dirac spinors (f):

$$f_{L,R} = \frac{1}{2}(1 - \gamma^5)f \tag{1.13}$$

where the $\gamma^5 = i\gamma^0\gamma^1\gamma^2\gamma^3$.

Based on the chirality, the fermions and the quarks form left-handed doublets and right-handed singlets. Massless neutrinos are assumed to comply with the observed violation of parity on weak interactions, where the neutrinos are considered only "left-handed" and the anti-neutrinos are always "right-handed".

For leptons:

$$\psi_{leptons} = \begin{pmatrix} \nu_e \\ e \end{pmatrix}_L, e_R, \begin{pmatrix} \nu_\mu \\ \mu \end{pmatrix}_L, \mu_R, \begin{pmatrix} \nu_\tau \\ \tau \end{pmatrix}_L, \tau_R,$$

For quarks:

$$\psi_{quarks} = \begin{pmatrix} u \\ d \end{pmatrix}_L, u_R, d_R, \begin{pmatrix} c \\ s \end{pmatrix}_L, c_R, s_R, \begin{pmatrix} t \\ b \end{pmatrix}_L, t_R, b_R,$$

The free Lagrangian for chiral leptons transforms under $SU(2)_L$ transformations with the following form:

$$\begin{aligned} \psi_L &\rightarrow \psi'_L = e^{i\theta(\hat{x})\hat{\tau}}\psi_L \\ \psi_R &\rightarrow \psi'_R = \psi_R \end{aligned} \tag{1.14}$$

In order to preserve the local invariance of the Lagrangian, the covariant derivative is used:

$$\partial_\mu \rightarrow D_\mu = \partial_\mu - ig\frac{\hat{\tau}}{2}W^i_\mu \tag{1.15}$$

where $W_\mu = W^1_\mu, W^2_\mu, W^3_\mu$. From the triplet, W^1_μ and W^2_μ couple to charged currents, whereas the W^3_μ couples to neutral currents.

For the construction of a combined electroweak current, the presence of the electromagnetic field is necessary. The weak hypercharge (Y) is defined in terms of the third component of the

weak isospin (I_3 [1]) and the electric charge (Q_f).

$$Y_f = 2Q_f - 2I_f^3 \tag{1.16}$$

The "left-handed" leptons have weak hypercharge $Y_L = -1$, whereas for "right-handed" leptons $Y_R = -2$. "Left-handed" quarks have $Y_{Q_L} = \frac{4}{3}$ whereas for "right-handed", $Y_{Q_R} = -\frac{2}{3}$. For the $U(1)_Y$ symmetry, a new field B_μ, is introduced to account for the electromagnetic interactions in the combined field.

Therefore, the combination of $SU(2)_L \times U(1)_Y$ is the gauge group for the unified electromagnetic and weak interactions, where the generators of $U(1)_Y$ (weak hypercharge, involving both chiralities) commute with those of $SU(2)_L$ (weak isospin, left-handed).

The transformations in the Lagrangian have now the following form:

$$\begin{aligned} \psi_L &\to \psi'_L = e^{i\theta(x)_i\tau_i + i\alpha(x)Y}\psi_L \\ \psi_R &\to \psi'_R = e^{i\alpha Y}\psi_R \end{aligned} \tag{1.17}$$

$$\partial_\mu \to D_\mu = \partial_\mu - ig\frac{\hat{\tau}}{2}W_\mu^i - i\frac{g'}{2}YB_\mu \tag{1.18}$$

where **g** is the coupling constant of the $SU(2)_L$ weak charged fields and **g'** is the coupling constant for the $U(1)_Y$ neutral field.

The field-strength tensors which correspond to the kinetic energy terms of the bosonic fields:

$$\begin{aligned} W_{\mu\nu}^i &= \partial_\mu W_\nu^i - \partial_\nu W_\mu^i - gW_\mu^k W_\nu^l \epsilon_{jkl} \\ B_{\mu\nu} &= \partial_\mu B_\nu - \partial_\nu B_\mu \end{aligned} \tag{1.19}$$

The weak gauge fields can be associated with the physical vector boson fields, $W_\mu^\pm$ for the weak charged ones, Z_μ for the weak neutral field and A_μ for the QED field:

$$\begin{aligned} W_\mu^\pm &= \frac{1}{\sqrt{2}}(W_\mu^1 \mp iW_\mu^2) \\ Z_\mu &= \cos\theta_w W^3 - \sin\theta_w B_\mu \\ A_\mu &= \sin\theta_w W^3 + \cos\theta_w B_\mu \end{aligned} \tag{1.20}$$

where θ_w is the weak mixing angle, defined by:

$$g\sin\theta_w = g'\cos\theta_w \tag{1.21}$$

[1] $\boldsymbol{I_3} = \frac{1}{2}\boldsymbol{\tau^3} = \frac{1}{2}\begin{pmatrix} \mathbf{1} & \mathbf{0} \\ \mathbf{0} & \mathbf{-1} \end{pmatrix}$

1.1.4 Standard Model - $SU(3)_C \times SU(2)_L \times U(1)_Y$

The unification of the electromagnetic and weak interaction results in the group $SU(2)_L \times U(1)_Y$. Including the quark sector from the $SU(3)_C$ group, , the Standard Model Lagrangian takes the form:

$$\begin{aligned}\mathcal{L}_{SM} = &\bar{\psi}_{\mathrm{Lep}_{Li}} i D_\mu \gamma^\mu \psi_{\mathrm{Lep}_{Li}} + \bar{\psi}_{\mathrm{Lep}_{Ri}} i D_\mu \gamma^\mu \psi_{\mathrm{Lep}_{Ri}} \\ &+ \bar{\psi}_{\mathrm{Q}_{Lj}} i D_\mu \gamma^\mu \psi_{\mathrm{Q}_{Lj}} + \bar{\psi}_{\mathrm{Q}_{Rj}} i D_\mu \gamma^\mu \psi_{\mathrm{Q}_{Rj}} \\ &- \frac{1}{4} G^\alpha_{\mu\nu} G^{\mu\nu}_\alpha - \frac{1}{4} W^a_{\mu\nu} W^{\mu\nu}_a - \frac{1}{4} B_{\mu\nu} B^{\mu\nu}\end{aligned} \tag{1.22}$$

where the covariant derivative is now:

$$D_\mu = \partial_\mu - i g \frac{\hat{\tau}}{2} W^i_\mu - i \frac{g'}{2} Y B_\mu - i g_s T_\alpha G^a_\mu \tag{1.23}$$

The symmetry group is $SU(2)_L \times U(1)_Y \times SU(3)_C$ to which the Lagrangian is invariant under local gauge transformations. Summarizing the described interactions, there are eight massless vector bosons G^α_μ which are the mediators of the strong interaction, and four massless vector bosons for the electroweak interaction $W^{1,2,3}_\mu, Z_\mu$.

The experimental observations show that the gluons, the mediators of the strong interaction, are massless. For the electroweak interaction, only the mediator of the electromagnetic force, the photon (γ), is massless and the vector bosons of the weak interaction ($W^\pm, Z_0$) are massive.

The introduction of massive terms for the bosons and the fermions would break the local gauge invariance of the Lagrangian. Therefore, a mechanism was needed which would generate the mass, while maintaining the photon massless and keeping the QED $U(1)_Q$ unbroken. The solution was given by the introduction of the Brout-Englert-Higgs-Guralnik-Hagen-Kibble mechanism [11, 12, 13], involving the theory of spontaneous symmetry breaking. Using Nambu [14] and Goldstone [15] adaptation of superconductivity Cooper pairs [16], that bosons appear on spontaneous symmetry breaking.

1.2 Spontaneous Symmetry Breaking - Higgs Mechanism

The Higgs Mechanism is based on the spontaneous symmetry breaking. When the breaking occurs on a continuous global symmetry, as a result, massless scalar (spin-0) particles known as "Nambu-Goldstone bosons" appear. The breaking of a continuous symmetry, for example could be the choice of a particular direction across a circle.

The motivation for the Higgs Mechanism was to apply the spontaneous symmetry breaking at the case of local invariance of the $SU(2)_L \times U(1)_Y$ symmetry group. Additionally, one would try to obtain massive three gauge bosons (Z,$W^\pm$) while having the photon (γ) massless.

Initially, a $SU(2)_L$ doublet of complex scalar fields is introduced:

$$\Phi = \begin{pmatrix} \phi^+ \\ \phi^0 \end{pmatrix} \qquad \Phi^\dagger = (\phi^-, \bar{\phi}^0) \tag{1.24}$$

The doublet has weak isospin T= $\frac{1}{2}$ and hypercharge Y = 1 for both components, resulting electromagnetic charge Q = 1,0 for $T^3 = \pm\frac{1}{2}$ upper and lower components of the doublet.

The complex scalar fields, corresponding to four degrees of freedom, can be written in terms of four real scalar fields as:

$$\phi^+ = \frac{\phi_1 + i\phi_2}{\sqrt{2}} \qquad \phi^0 = \frac{\phi_3 + i\phi_3}{\sqrt{2}} \tag{1.25}$$

One can retrieve now the scalar Lagrangian, which is invariant under $SU(2)_L \times U(1)_Y$ gauge transformations:

$$\mathcal{L}_{\text{scalar}} = (D_\mu \Phi)^\dagger D^\mu \Phi - V(\Phi) \tag{1.26}$$

where the covariant derivative is the one from Equation 1.23, excluding the strong interaction term.

The scalar potential V(Φ) is defined as:

$$V(\Phi) = \mu^2(\Phi^\dagger \Phi) - \lambda(\Phi^\dagger \Phi)^2 \tag{1.27}$$

Asking $\lambda < 0$ and $\mu^2 < 0$, the V(Φ) potential has the characteristic shape shown on Figure 1.2.

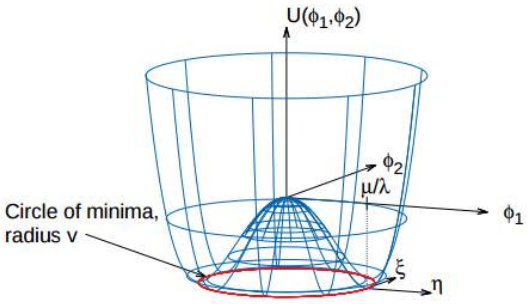

Figure 1.2: Potential of the scalar field Φ

Therefore, the potential has infinite degenerated minima below V(Φ) = 0.

The minima are determined by:

$$\begin{aligned} \frac{dV}{d(\Phi^\dagger\Phi)} = 0 \Rightarrow \mu^2 - 2\lambda(\Phi^\dagger\Phi) = 0 \\ \Phi^\dagger\Phi = \frac{\mu^2}{2\lambda} \\ \frac{1}{2}(\phi_1^2 + \phi_2^2 + \phi_3^2 + \phi_4^2) = \frac{\mu^2}{2\lambda} \end{aligned} \tag{1.28}$$

Performing transitions around the circle of minima does not cost energy and corresponds to massless particles which are quantum excitations. Thus, the $SU(2)_L \times U(1)_Y$ symmetry spontaneously breaks, when a set of minima is arbitrarily chosen since it is associated with a particular direction in the $SU(2)_L \times U(1)_Y$ space.

The set of minima is chosen in a way where all the scalar fields have zero vacuum expectation value (vev) apart from one component of the neutral field (ϕ^0) in order to maintain the photon massless :

$$\begin{aligned} \langle 0|\phi_1|0\rangle = \langle 0|\phi_2|0\rangle = \langle 0|\phi_4|0\rangle = 0 \\ \langle 0|\phi_3|0\rangle = \upsilon^2 \end{aligned} \tag{1.29}$$

where $\upsilon^2 = \frac{\mu^2}{\lambda}$.

An important part of the previous random minima selection is that the QED $U(1)_Q$ is preserved, since the electromagnetic charge remains 0 for the neutral field. Having chosen the new vacuum state, the neutral Higgs field (H) is introduced which will describe quantum fluctuations around this state. So, the field Φ can be expanded around the chosen vacuum:

$$\Phi = \frac{1}{\sqrt{2}} e^{i\theta_i(x)\vec{\tau}/\upsilon} \begin{pmatrix} 0 \\ H + \upsilon \end{pmatrix} \tag{1.30}$$

In the previous notation, it is ensured the presence of four real degrees of freedom (θ_k and H)

Applying now the local gauge transformation, one obtains:

$$\begin{aligned} \Phi \rightarrow \Phi' &= e^{-\left(\frac{i\vec{\tau}\theta(x)}{\upsilon}\right)}\Phi \\ &= \frac{1}{\sqrt{2}} \begin{pmatrix} 0 \\ \upsilon + H \end{pmatrix} \end{aligned} \tag{1.31}$$

Therefore, applying a local gauge transformation at the new field Φ (Eq. 1.31), we observe that three nonphysical degrees of freedom (θ^i) disappear and only the Higgs field remains invariant. Since the Equation 1.31 does not contain nonphysical degrees of freedom, it is called

unitary gauge.

After the introduction of the unitary gauge, the Lagrangian of the scalar field can be calculated (Eq. 1.26). Initially, the covariant derivative (Eq. 1.23) terms for the $SU(2)_L \times U(1)_Y$ symmetry are:

$$\begin{aligned} D_\mu \Phi &= \begin{pmatrix} \partial_\mu + i\frac{g}{2}W_\mu^3 + i\frac{g'}{2}B_\mu & i\frac{g}{2}(W_\mu^1 - iW_\mu^2) \\ i\frac{g}{2}(W_\mu^1 + iW_\mu^2) & \partial_\mu - i\frac{g}{2}W_\mu^3 + i\frac{g'}{2}B_\mu \end{pmatrix} \begin{pmatrix} 0 \\ \upsilon + H \end{pmatrix} \\ &= \begin{pmatrix} i\frac{g}{2}(W_\mu^1 - iW_\mu^2)(\upsilon + H) \\ \partial_\mu - i\frac{g}{2}W_\mu^3 + i\frac{g'}{2}B_\mu(\upsilon + H) \end{pmatrix} \end{aligned} \tag{1.32}$$

Replacing the gauge fields (W_μ^i, B_μ) with the natural fields $W^\pm, Z_\mu, A_\mu$ from Eq. 1.20, the covariant becomes:

$$\begin{aligned} D_\mu \Phi &= \frac{1}{\sqrt{2}} \begin{pmatrix} \frac{ig}{\sqrt{2}}W_\mu^+(\upsilon + H) \\ (\partial_\mu - \frac{i}{2}(g\cos\theta_w + g'\sin\theta_w)Z_\mu)(\upsilon + H) \end{pmatrix} \\ (D_\mu \Phi)^\dagger &= \frac{1}{\sqrt{2}} \begin{pmatrix} -\frac{ig}{\sqrt{2}}W_\mu^-(\upsilon + H) & (\partial_\mu + \frac{i}{2}(g\cos\theta_w + g'\sin\theta_w)Z_\mu)(\upsilon + H) \end{pmatrix} \end{aligned} \tag{1.33}$$

Therefore the Lagrangian of the scalar field Φ is obtained (Eq. 1.26):

$$\begin{aligned} \mathcal{L}_{\text{scalar}} &= (D_\mu \Phi)^\dagger D^\mu \Phi + \mu^2(\Phi^\dagger \Phi) - \lambda(\Phi^\dagger \Phi)^2 \\ &= \frac{1}{2}\partial_\mu H \partial^\mu H \\ &+ (H^2 + 2\upsilon H + \upsilon^2)[\frac{1}{4}g^2 W_\mu^+ W^{-\mu} + \frac{1}{8}(g^2 + g'^2)Z_\mu Z^\mu] \\ &+ \mu^2 H^2 + \frac{\lambda}{4}(H^4 + 4\upsilon H^3) \end{aligned} \tag{1.34}$$

The Lagrangian contains only terms for the weak gauge fields whilst the QED field A_μ is absent ensuring that the mediator, the photon (γ) remains massless. Reading off the quadratic terms for fields, $M_W^2 W_\mu^+ W^{-\mu}$ and $\frac{1}{2}M_Z^2 Z_\mu Z^\mu$, the masses of the weak vector bosons can be identified:

$$\begin{aligned} M_w &= \frac{1}{2}g\upsilon \\ M_z &= \frac{1}{2}\sqrt{(g^2 + g'^2)}\upsilon = \frac{1}{2}\frac{g\upsilon}{\cos\theta_w} \\ M_\gamma &= 0 \end{aligned} \tag{1.35}$$

The masses of the two weak bosons are related:

$$\frac{M_W}{M_Z} = \frac{g'}{\sqrt{g^2 + g'^2}} = \cos\theta_w \tag{1.36}$$

The Higgs field vacuum expectation value (υ) is related to the M_w and Fermi constant ($G_F = 1.166 \times 10^{-5} GeV^{-2}$), through the muon beta decay:

$$\left.\begin{array}{ll} M_w & = \frac{1}{2} g\upsilon \\ M_w & = \sqrt{\frac{\sqrt{2}g^2}{8G_F}} \end{array}\right\} u = \frac{1}{\sqrt{\sqrt{2}G_F}} \approx 246\text{GeV} \tag{1.37}$$

For the Higgs field, the mass of the scalar Higgs boson can be identified from the H^2 coefficient corresponding to $-\frac{1}{2}M_H^2$:

$$M_H = \sqrt{-2\mu^2} = \sqrt{2\lambda\upsilon^2} \tag{1.38}$$

The most recent calculations for the masses of the weak vector bosons are: $M_w = 80.385 \pm 0.015$ GeV and $M_z = 91.188 \pm 0.002$ GeV. [17]

The Higgs boson mass was a free parameter in the Standard Model since the value of the parameter λ is unknown by theory. The discovery of the Higgs boson particle took place on July 2012 [18] and the latest reference value is : $M_H = 125.09 \pm 0.24$ GeV [17]. Also, from the higher order interaction term in the Lagrangian, one observes Higgs self interactions proportional to the square of the mass:

$$\begin{aligned} g_{H^3} &= \frac{M_H^2}{2\upsilon} = \lambda\upsilon \\ g_{H^4} &= \frac{M_H^2}{8\upsilon^2} = \frac{\lambda}{4} \end{aligned} \tag{1.39}$$

At the previously described mechanism, when the complex scalar Higgs field, Φ, gets a vacuum expectation value further from 0, then the $SU(2)_L \times U(1)_Y$ symmetry spontaneously breaks into the invariant $U(1)_Q$ (QED). After the symmetry breaking, three extra degrees of freedom emerge, corresponding to three Nambu-Goldstone bosons. The latter provide extra longitudinal polarization degrees of freedom to the massless weak gauge bosons which become massive.

Therefore, the mechanism of the spontaneous symmetry breaking, succeeds in explaining the massive weak gauge bosons ($W^{\pm}, Z$), respecting in parallel the electric charge and color charge conservation ($U(1)_Q$ and $SU(3)_C$ respectively) keeping massless mediators (photons, gluons).

1.2.1 Lepton and quark mass

The Higgs field is responsible also for the generation of the leptons mass. A Yukawa interaction occurs between the chiral fermionic fields and the Higgs field. An extra Yukawa interaction term enters into the Lagrangian 1.34, which is $SU(2)_L \times U(1)_Y$ invariant.

$$\mathcal{L}_Y = -G_e[\bar{\psi_L}\Phi\psi_R + \bar{\psi}_R\Phi^\dagger\psi_L] \tag{1.40}$$

where G_e is the corresponding Yukawa coupling for every fermion, with total 3×3 couplings. After spontaneous symmetry break at the Lagrangian, there is one term $(\frac{G_e v}{\sqrt{2}}\bar{\psi}\psi)$ which shows the mass of the fermionic field and an extra term, $\bar{\psi}\psi H$, which shows the fermion-Higgs coupling.

There the mass is calculated by:

$$m_f = \frac{G_F \times v}{\sqrt{2}} \tag{1.41}$$

and the coupling to the Higgs boson:

$$G_F = \frac{\sqrt{2} \times m_f}{v} \tag{1.42}$$

The coupling of a fermion to the Higgs field is proportional to the fermion mass, meaning that stronger fermion couplings to the Higgs field, result in heavier fermions.

Also, given the fact that the upper element of the unitary gauge is zero, no mass term will be generated for the upper element of the weak chiral doublet, retaining therefore a massless neutrino.

For quarks, the description is not entirely complete, since one should take into account the quark mixing through the elements of the CKM matrix.

1.3 Higgs boson production channels and decays

The main production mechanisms of the Higgs boson are the following:

1. Gluon-gluon fusion (ggF) : $gg \rightarrow H$
2. Vector boson fusion (VBF) : $q\bar{q} \rightarrow VVq\bar{q} \rightarrow Hq\bar{q}$, V = $W^\pm, Z$
3. Associated production with vector boson: $q\bar{q} \rightarrow VH$, V = $W^\pm, Z$
4. Associated production with top: $gg, q\bar{q} \rightarrow t\bar{t}H$

The lowest order Feynman diagrams for the Higgs production mechanisms are shown on Figure 1.3

In hadron colliders, the dominant production for a Standard Model-like Higgs boson is the gluon-gluon fusion followed by vector boson fusion. The associated productions (WH, ZH, $t\bar{t}H$) have a less than 5% total contribution.

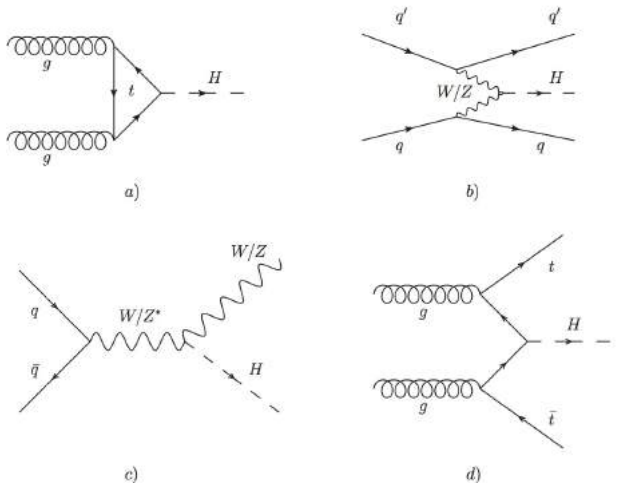

Figure 1.3: Feynman diagrams for the different Higgs production mechanisms: (a) gluon-gluon fusion, (b) vector boson fusion, (c) associated production with vector boson, (d) associated production with $t\bar{t}$ pair.

The Higgs boson decays to a particle-antiparticle pair. The main decay for mass below 130 GeV is a $b\bar{b}$ pair whereas for higher masses, decays to vector boson pairs (WW, ZZ) dominate.

The coupling of the Higgs boson to the weak bosons (V) can be extracted from the interaction terms in the Equation 1.34:

$$g_{H\to VV} = \frac{2m_V^2}{\upsilon} = 2\sqrt{(\sqrt{2}G_F)}M_V^2 \tag{1.43}$$

An overview of the decay probability for each channel (branching ratio) is shown on Figure 1.4.

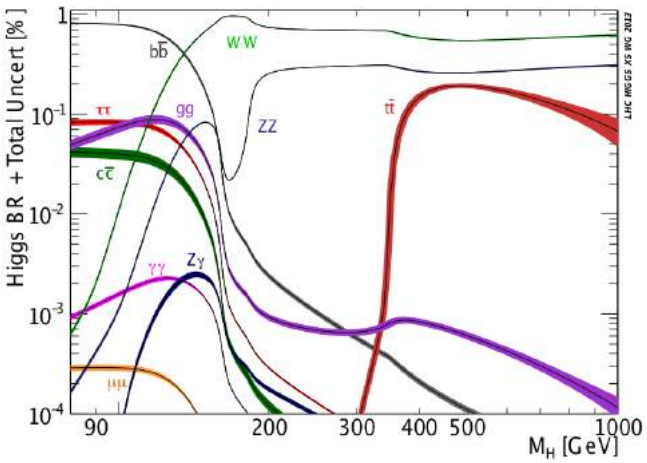

Figure 1.4: Branching ratios for the various Higgs decay channel. Figure from [19].

1.3.1 Additional heavy Higgs searches

The search of the Standard Model Higgs boson was performed in a wide mass range from ≈ 100-1000 GeV. Despite the discovery of ≈ 125 GeV mass particle, the "high-mass" (> 300 GeV) is an important regime for Beyond the Standard Model searches.

The discovery of the light SM Higgs boson (m_H = 125 GeV) and the study of its properties show compatibility with the SM expectations [20]. However, it is not experimentally verified whether the 125 GeV Higgs boson is responsible for the formation of the fermion masses and the unitarisation, at high-energies of the scattering amplitudes of the processes $V_L V_L \rightarrow V_L V_L$ where V is either the W boson or the Z boson. Thus, the possibility of the existence of extra Higgs bosons has to be assesed. The low mass Higgs might be responsible for the unitarisation and an additional Higgs couples to other generations of fermions. Therefore, searches for an additional SM-like heavy Higgs boson are strongly motivated in order to have the Beyond the Standard Model sector explored.

Many models have been developed which try to accommodate the potential existance of an additional heavy Higgs boson with new phenomena like SUSY. Such models assume the existance of an additional electroweak singlet field [21] or two Higgs doublet fields where the presence of five Higgs bosons is speculated [22], either with large or narrow decay width approximations [23].

For a search in the high mass regime, in first approximation SM-like properties are assumed.For a SM Higgs boson the decays are dominated by decays to weak vector bosons pairs, WW and ZZ, with the main decay mechanism to be the semileptonic decay $H \rightarrow WW \rightarrow lvqq$. A summary of all the decay rates is shown in Figure 1.5.

At the full high mass regime, the decay $ZZ \rightarrow l^+l^-l^+l^-$ provides the cleanest experimental channel, similar to the low mass, due to the very small lepton reconstruction uncertainties. The major background source for this channel is the irreducible Standard Model ZZ diboson production. Therefore, the $ZZ \rightarrow l^+l^-l^+l^-$ decay channel, despite the low branching fraction, would provide a clean experimental identification of additional SM-like Higgs bosons.

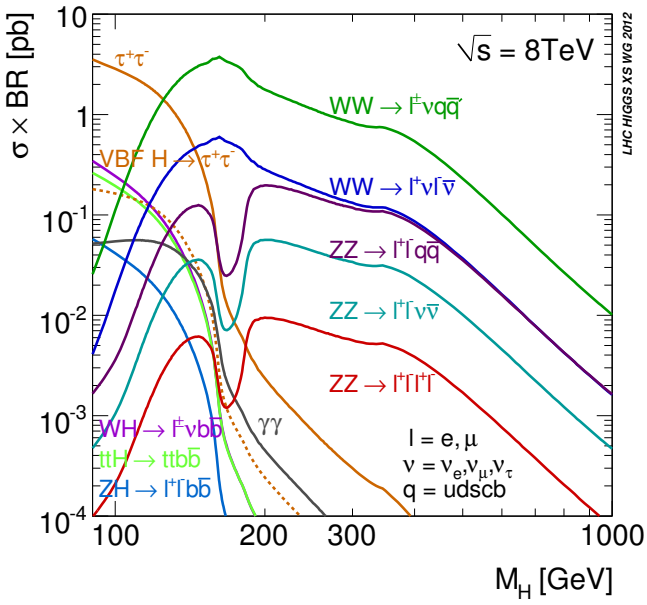

Figure 1.5: Standard Model Higgs boson production cross section times branching ratio at 8 TeV . Figure from [19].

1.4 Proton-Proton collisions

At the head-on proton-proton collisions, the protons are subjected to relativistic energies in very short distance. Therefore, the protons are not considered as point-like particles.

According to the partonic model by Feynman [24], all the proton constituents are considered as *partons*: the up and down quarks, the gluons and all the sea quarks and anti-quarks which arise due to quantum fluctuations. The probability of a particular parton to have a momentum fraction (x) of the total momentum transferred (Q^2) is given by the *Parton Distribution Functions* (PDFs). An example of PDF is shown on Figure 1.6.

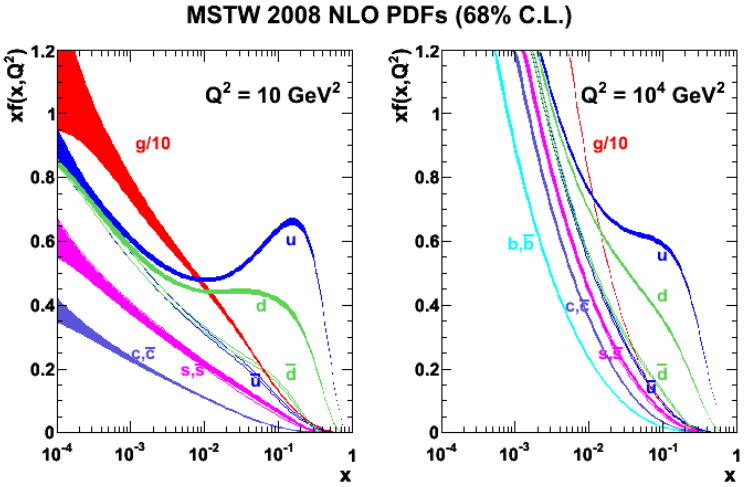

Figure 1.6: MSTW Leading Order PDF for a proton with 10 GeV energy. Figure from [25].

In the proton-proton interaction, there are multiple types of interactions between the partons. All the different kinds of interactions make up the structure of an event.

Initially, the momentum transfer between the protons could be either large around GeV, when it is called *hard* interaction or small at the level of MeV, called *soft* interaction. The hard interactions between the partons can lead to creation of particles. In a single interaction between two proton bunches, there is an increased soft hadronic activity which is defined as defined as *pile-up* events.

Interactions could be observed between remnant partons of the colliding protons which were not involved in the hard interaction. Those interactions comprise the *underlying event (UE)* which are treated as background events. Additionally, it is possible to have multiple partons from one proton to interact with multiple partons from the other ones. These are called *multi-parton interactions (MPI)*. The Double Drell-Yan study which is described in Chapter is a multi-parton interaction.

Lastly, for any particles carrying charge it is possible to emit radiation. In colour charge,

the emission involves hadronising gluons whereas in electromagnetic charge, EM radiation is emitted. Radiation related to the incoming partons is called Initial State Radiation (ISR) and if related to the outgoing partons or the decay products, it is called Final State Radiation (FSR).

An overview of the event structure at p-p collisions is shown in Figure 1.7

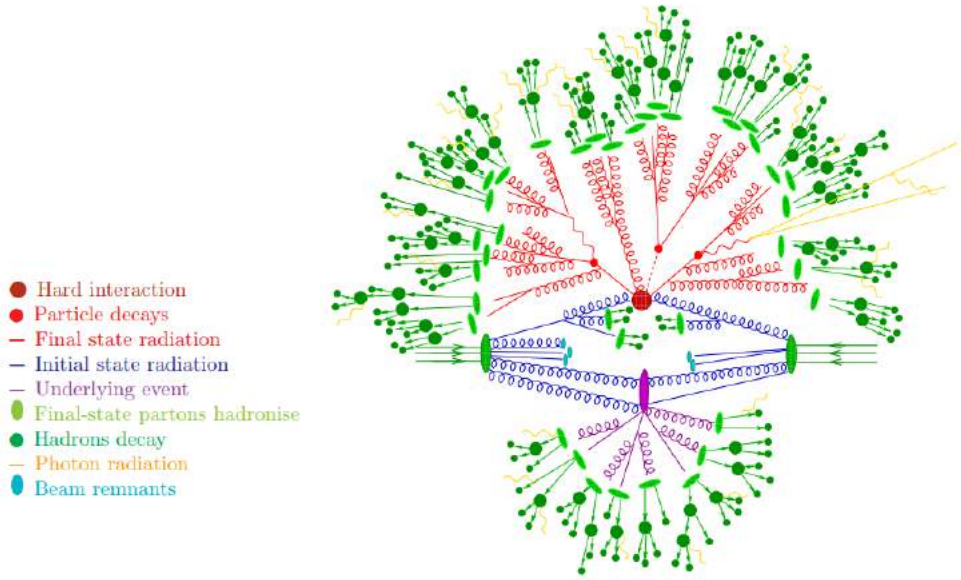

Figure 1.7: Event structure at p-p collision. Figure from [26]

1.5 Double Parton Interaction

The development of the partonic model highlighted the composite structure of the hadrons. During proton-proton interactions it is possible to have independent multiple parton hard scatterings between the two protons. Such a behaviour is observable at higher energies, where according to the Parton Distribution Functions, more sea quarks carry a sizeable fraction of the proton momentum.

In the case where two different partons are involved, the mechanism is called Double Parton Interaction (DPI). It is assumed that the $q\bar{q}$ pairs come from the sea quarks of both protons.

The cross-section of the Double Parton Interaction can be written as a product of double Parton Distribution Functions, assuming two independent single parton interactions A and B[27, 28]:

$$\sigma_{\mathrm{DPI}}^{AB} = \frac{m}{2} \sum_{i,j,k,l} \int \Gamma_{ij}(x_1, x_2, b; t_1, t_2) \times \Gamma_{kl}(x_3, x_4, b; t_1, t_2) \times \hat{\sigma_{ik}^{A}}(x_1, x_3) \hat{\sigma_{jl}^{B}}(x_2, x_4) dx_1 dx_2 dx_3 dx_4 d^2b \tag{1.44}$$

The $\Gamma(x_i, x_j, b; t_i, t_j)$ factor is the generalised double Parton Distribution Functions for the two partons (i,j) which have x_i, x_j proton momentum fractions, at scale $t_i = \ln(Q_i^2)$, which correspond to the energy resolution scale of each interaction. The factor b expresses the transverse distance which separates the two partons. The factor m equals 1 for symmetrical processes or 2 for distinguishable processes.

The double PDF can be written as a product of the two single PDFs, each concerning the separate parton. Such an approach is valid, under the assumption that more partons carry a fraction of momentum, having small values of x and thus there is a higher probability for scatterings between multiple partons to take place.

$$\Gamma_{ij}(x_i, x_j, b) = D_i(x_i) D_j(x_j) F(b) \tag{1.45}$$

where D(x) are the single parton distribution functions. F(b) is a function that expresses the transverse distribution of the partons. The analytical description of F(b) depends on the assumed model that describes the distribution of the partonic constituents inside the proton. The assumed model does not take into account of quark flavours and spins.

All the transverse plane spatial correlations can be described with a scale factor, the σ_{eff}.

$$\sigma_{\mathrm{eff}} = \left[\int [F(b)^2 d^2b]^2 \right]^{-1} \tag{1.46}$$

The scale factor σ_{eff} represents the cross-section where the inclusive rate of the double interactions is similar to the inclusive rate of multiple single interactions. With all the previous

considerations the cross-section of double parton interaction (Eq. 1.44) can be expressed as:

$$\sigma_{\mathrm{DPI}}^{AB} = \frac{m}{2}\frac{\sigma_A \sigma_B}{\sigma_{\mathrm{eff}}} \tag{1.47}$$

Several phenomelogical studies have been performed focusing on the validity of the factorisation equation 1.45. Such studies focus on the expression of the transverse distributions of the partons excluding correlations, and the dispersion of the interactions. On the other side, there are studies focusing mainly on the description of the double PDFs trying to include multi-parton correlations through QCD evolution [29, 30].

In literature, the universality of σ_{eff} and the dependence with collision energy and the process is still an open problem. Neglecting any correlation between the partons and assuming a simple Gaussian distribution of the partons, one obtains an expression of $\sigma_{\mathrm{eff}} = 2\pi R^2$ where R is the radius of the overlapping function (F(b)) between the two hadrons. The radius is equal to $R^2 = 4/3\langle r^2 \rangle$, where $\sqrt{\langle r^2 \rangle}$ is the rms proton radius. Assuming $\sqrt{\langle r^2 \rangle} = 0.6$fm one obtains a value of $\sigma_{\mathrm{eff}} \approx 30$ mb.

Experimental results indicate a strong difference compared to this value, as it can be shown on Figure 1.8. The latest model [29] assumes double Gaussian distribution of the parton at the transverse plane and predict a value of $\sigma_{\mathrm{eff}} = 11$ mb, which is close to the experimental values. The latest measurement for σ_{eff} by ATLAS is $15\pm3(\mathrm{stat.})^{+5}_{-3}(\mathrm{sys.})$ mb derived using W→lv + 2jets [31] originating from DPI. Additionally, ATLAS has published a lower limit of 3.7mb (95% CL) from the Z+J/ψ analysis[32].

1.5.1 Double Drell-Yan process

The Drell-Yan process [34] is part of the Double Parton Interactions and describes the creation of the neutral current lepton pair due to a quark-antiquark annihilation to either virtual photon (γ^*) or Z boson. The phenomenolgical formalism of a Double Drell-Yan mechanism has been developed over the past years [35, 36]. The Double Drell-Yan mechanism is depicted on Figure 1.9

Up to the time of the present thesis, there has not been any clear experimental observation of the process. This is due to the high background rates of similar final state processes, for example Standard Model ZZ→4l production.

A study of the multiparton interactions is essential for further understanding of the proton structure. Through the multiparton studies it is possible to highlight correlations between the PDFs and the distribution of the partons. Lastly, the double PDFs could be formulated in a more concretely whilst taking into account any further correlations between the interacting partons, like spin dependences. Additionally, through the multi-parton interactions the possibility is given to study the distribution of the partons inside the proton and how this affects the interaction.

An in-depth knowledge and description of the way that the partons interact is an important

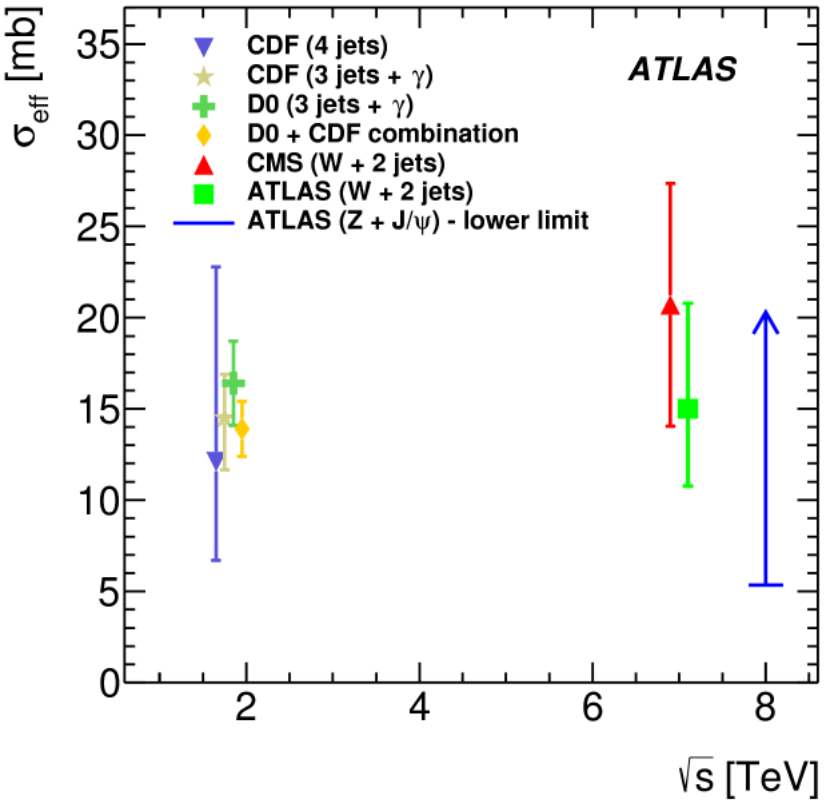

Figure 1.8: Summary of all the effective cross-section (σ_{eff}) measurements. . Figure from [33].

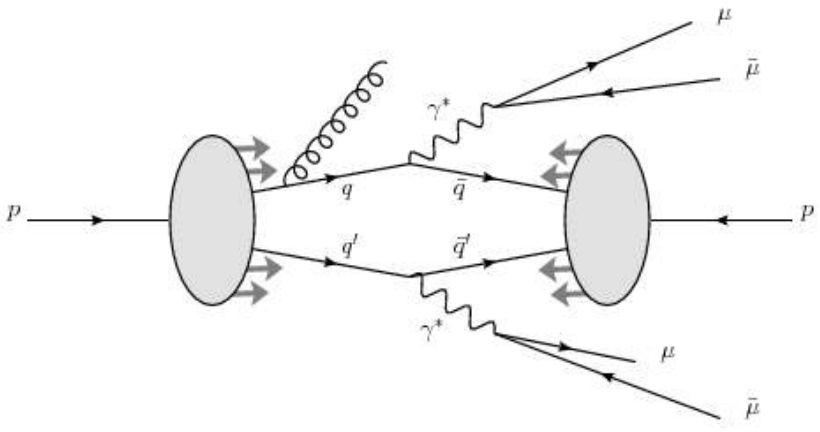

Figure 1.9: Illustration of the Double Drell-Yan mechanism. Figure from [28].

element for p-p collisions. With more precise information, the simulations of the p-p interactions could be more accurate, leading to better estimation of expected event yield from either processes of interest or hadronic background.

In high masses and energy scales where the DDY is examined, a single factor can not universally parametrise two independent interactions. Additionally, recent theory QCD models [37] expect different σ_{eff} behaviour when correlations in the transverse plane involve different initial states ($q_1, q_2/\bar{q}_1, q_2, /q_1, \bar{q}_2/\bar{q}_1, \bar{q}_2/gg$). Lower values are expected when the transverse plane involves a quark-antiquark interaction than a gluon-gluon initiated process due the different parton distributions at the transverse plane.

Chapter 2

The Large Hadron Collider and the ATLAS detector

2.1 Hadron colliders

In Experimental Particle Physics, accelerating particles for probing new phenomena was the basic mechanism since the early 20th century. With technology advances, the accelerating techniques have improved over the years.

Two methods are employed for particles accleration. These are fixed-target and the beams collisions. At fixed target collisions, the particles collide with a static target whereas with the beams case they are brought together through head-on collision.

The head-on collision is the most energy efficient method, since all the energy of the beam is converted to Centre-of-Mass frame rest-mass energy ($\sqrt{s} = 2E_{\text{beam}}$), capable to produce new, heavier particles. For the fixed-target experiments, a fraction of the available energy must be given as kinetic energy to the produced particles, offering less energy for the creation of heavier particles.

The particles are considered relativistic, so their energy is expressed by the equation:

$$E^2 = m_0^2 c^4 + |\vec{p}|^2 c^2 \tag{2.1}$$

From the known stable particles, the electron and the proton have been used in accelerators. The different rest mass values between them (proton: $\approx$ 1000 MeV, electron : 0.511 MeV), has as result a substantial difference at the provided centre-of-mass energy.

Over the past years, circular particle colliders were mainly used for the experimental investigation of particle physics. The main accelerator rings were: the HERA at DESY, Germany, with $e^{\pm}p$ collisions; the LEP at CERN, Switzerland, with $e^{+}e^{-}$ collisions; the TEVATRON at Fermilab, USA, with $p\bar{p}$ collisions; and the LHC at CERN, with pp collisions.

2.2 The Large Hadron Collider

The Large Hadron Collider (LHC) [38] is the most powerful accelerator machine worldwide, operating at the moment with a beam energy of 6.5 TeV, providing a total centre-of-mass ($\sqrt{s}$) energy of 13 TeV. The accelerator works mainly for proton-proton collisions, but provides also conditions for proton-lead (p-Pb) or lead-lead (Pb-Pb) collisions.

The LHC is situated at the European Centre of Nuclear Research (CERN) in Geneva, Switzerland. The construction of the LHC was approved in 1994, started in 1997 and finished in 2007. The 26.7 km long underground tunnel which housed the predecessor accelerating complex of the Large Electron-Positron Collider (LEP) was chosen as the location, spanning across the French-Swiss border. After the end of LEP operation on 2000, necessary configurations were made in the 3.8 metre wide channel for the installation of the LHC.

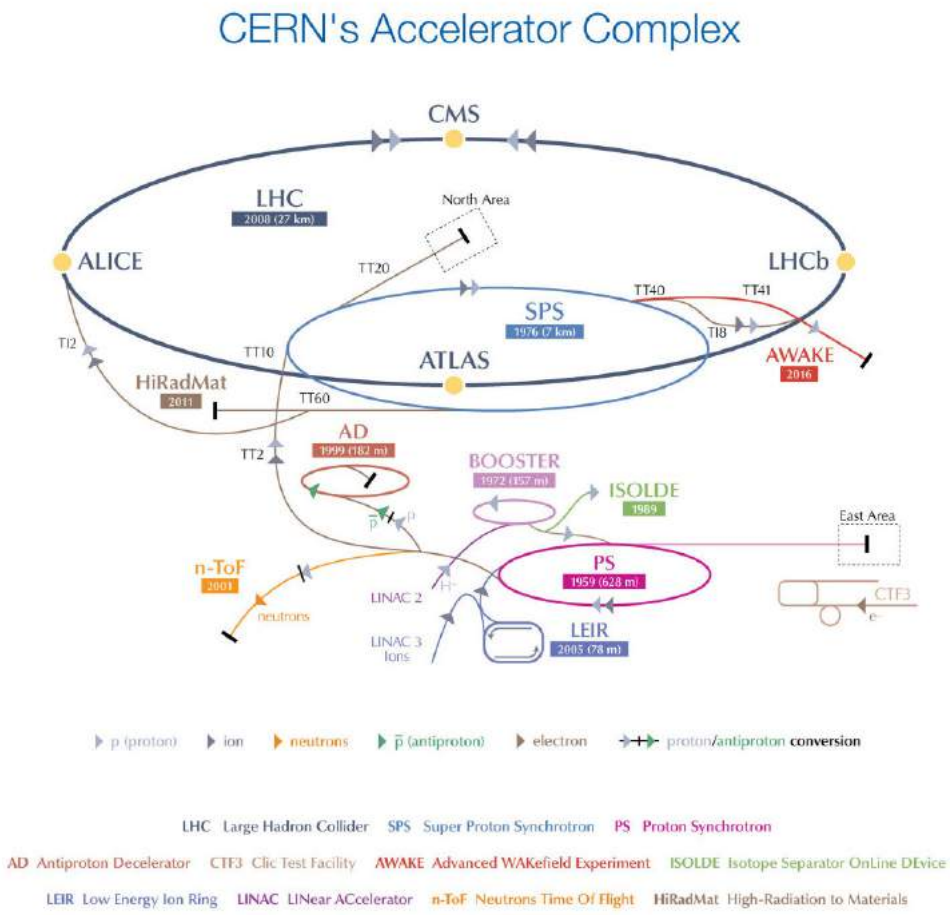

Figure 2.1: The CERN accelerating complex. Figure from [39]

The LHC has been designed to deliver a total centre-of-mass energy, $\sqrt{s}$=14 TeV, (7 TeV per beam) and 2.76 TeV per nucleon during heavy ions collisions. The designed value is 2808 proton bunches per beam, each containing $1.1 * 10^{11}$ protons with collisions every 25ns. To achieve these conditions, the LHC comprises 9593 superconducting magnets and 8 radio-frequency (RF) cavities. The vacuum pressure inside the pipes is 10^{-13} atm in a temperature of 1.9K (-271.3^o C).

In order to reach the desired energy, the protons have to pass through the full acceleration complex. Initially, the protons are stripped off from hydrogen gas using electric fields and afterwards they are injected into the LINAC2 machine. There, they achieve energy of 50 MeV through linear acceleration. Then, they enter the Proton Synchrotron Booster (PSB), reaching the energy of 1.4 GeV. The Proton Synchrotron (PS) and the Super Proton Synchrotron (SPS) follow, where the energy rises to 25 and 450 GeV respectively, before being injected into the main LHC pipes. The bunches circulate in opposite directions between 5 and 24 hours while collisions take place. An overview of the accelarating complex is shown in Figure 2.1.

Inside the pipes, the bunches undergo linear acceleration through the electric field of the RF cavities, with an accelerating field of 5 MV/m at 400 MHz and bend through the magnetic field of the 1232 dipole superconducting magnets. The coils are made from niobium-titanium (NbTi) cables which are superconducting at these temperatures, creating a magnetic field of 8.33 T from the 11850 A flowing current. In addition, in order to maintain the whole system in these low, superconducting temperatures, the magnets are cooled down with super-fluid helium.

The acceleration technology developed by the LHC is utilised by the 7 experiments which serve across its circumference. In alphabetical order, these are: A Large Ion Collider Experiment (ALICE), A Toroidal LHC ApparatuS (ATLAS), Compact Muon Solenoid (CMS), LHC-beauty (LHCb), LHC-forward (LHCf), Monopole and Exotics Detector At the LHC (MoEDAL) and TOTal Elastic and diffractive cross section Measurement (TOTEM).

The physics scope of the LHC spans over a very wide range with a rich physical potential, with an remarkably unprecedented value for collisions energy in the field of Experimental Particle Physics. The most notable achievement during the Run 1, which operated from 2009 until 2012, is the discovery of the Higgs Boson in 2012 by the ATLAS and CMS experiments [18, 40], which led to the award of the 2013 Nobel Prize in Physics. The properties of the Higgs boson will be an important field of research for next LHC Runs. In addition,the validity of the Standard Model parameters has been examined from all the experiments. Many tests of Quantum Chromodynamics (QCD) have been conducted and are planned to be expanded for the second run of LHC, alongside the investigation of Electroweak Interactions and Flavour Physics. A better understanding of Quark-Gluon Plasma state and the CP-violation are the leading motivations for the ALICE and LHCb experiments. Moreover, the Physics Beyond the Standard Model is a key discovery goal for the future of this powerful discovery machine, where theories like Supersymmetry (SUSY), Exotic particles and Dark Matter will be tested at

higher energies with quite definitive outcomes.

2.2.1 LHC Performance

The physics studies detailed in the present thesis use data from the Run-I of the LHC collected up until the end of 2012. A summary of the LHC parameters [41, 42] during Run-I is detailed on Table 2.1.

Table 2.1: Main parameters of LHC during Run-I

Parameter	2010	2011	2012	Designed
Energy per beam [TeV]	3.5	3.5	4.0	7.0
Protons/bunch(10^{11} / bunch)	1.2	1.45	1.7	1.15
Bunches/bunch	368	1380	1380	2808
Bunch spacing [ns]	150	50	50	25
Peak instantaneous luminosity $\mathcal{L}$[cm^{-}2s^{-}]	2.1×10^{32}	3.7×10^{33}	7.7×10^{33}	1.0×10^{34}

The instantaneous luminosity is a factor which defines the rate of proton-proton interactions for particular collision parameters. It is defined as:

$$\mathcal{L} = \frac{N_p^2 k_b f \gamma}{4\pi\beta^* \epsilon_n} F$$

$\mathbf{N_p}$ is the number of protons per bunch, $\boldsymbol{k_b}$ is the number of bunches per beam, $\boldsymbol{f}$ is the revolution frequency of protons around the LHC ring, **F** is a geometry luminosity reduction factor parameter associated with the crossing angle of the beams, $\boldsymbol{\epsilon_n}$ is the beam emittance (spread of particle coordinates), $\boldsymbol{\beta^*}$ is the beta function at the collision point, which is related to the transverse amplitude of the beam, and γ the usual relativistic factor. The product of ϵ_n and β^* is connected to the transverse beam size at the interaction point [42].

Every particular process has its own production rate, called cross-section (σ). The integral of the instantaneous luminosity for a given period of time defines the integrated luminosity which, multiplied with the cross-section of the process, yields the expected number of events:

$$\mathrm{N_{exp}} = \sigma \times \int \mathcal{L} dt = \sigma \times L$$

During the 2012 $\sqrt{s} = 8$ TeV run, the LHC delivered 22.8 fb^{-1}data, out of which ATLAS recorded 21.3 fb^{-1}.

The total interaction cross-section (σ_{tot}) is split into two parts, the elastic (σ_{el}) and the inelastic (σ_{inel}). Roughly, at LHC energies the cross-section ratios are $\approx$ 20% for the elastic and $\approx$ 80% for the inelastic[43]. In particle collisions, the inelastic cross-section is the one of interest.

During LHC Run-I, the intensity of the beam and the instantaneous luminosity values increased the value of the expected inelastic interactions per bunch-crossing during the run pe-

riods. For 8 TeV centre-of-mass energy the inelastic cross-section σ_{inel} has been calculated as $\approx 75mb$ [44]. The 2012 LHC parameters were [42]: $\epsilon_\pi \sim 2.5\mu m$, $\beta^* \sim 0.6m$, $N_p \sim 1.7 \times 10^{11}$, $\gamma = 4.3 \times 10^3$. Using Equation 2.2.1 and assuming a geometrical factor F = 1 (no luminosity reduction), the maximum inelastic interaction per bunch crossing is calculated to be $\mu \approx 44$. The average interaction per bunch crossing on the 2012 run ($< \mu >$) was 20.7. The number of interactions per bunch crossing for the 2012 and 2011 luminosities values are shown in Figure 2.2

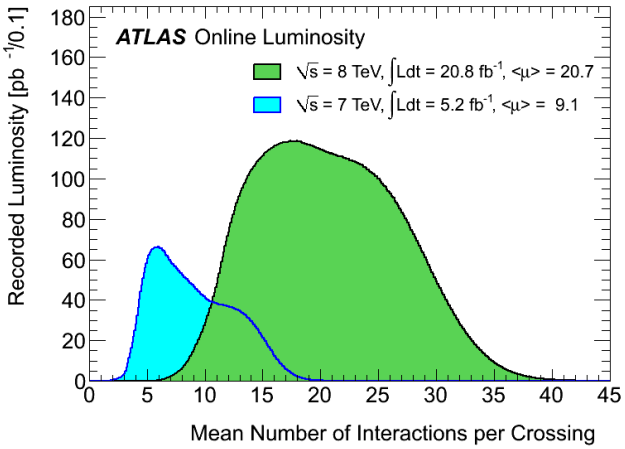

Figure 2.2: Luminosity-weighted distribution of the mean number of interactions per crossing for the 2011 and 2012 data. The mean number of interactions per crossing corresponds the mean of the Poisson distribution on the number of interactions per crossing calculated for each bunch. Figure from [45]

The total cross section for the proton-proton interaction, with the cross sections of various Standard Model processes as a function of the centre-of-mass energy is depicted in Figure 2.3.

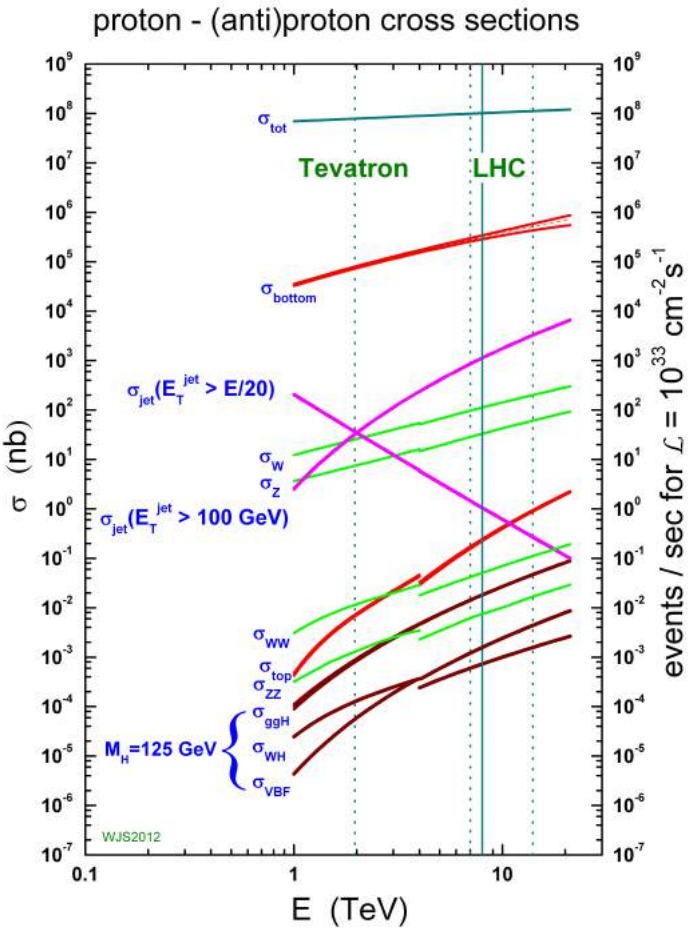

Figure 2.3: Cross sections for various SM processes versus $\sqrt{s}$. An indicative event rate has been calculated on the right side, assuming $\mathcal{L} = 10^{33}$ cm^{-2}s^{-1}. The MSTW[46] NLO PDF set was used. Figure from [47].

2.3 The ATLAS Detector

The ATLAS Detector[48] is a particle physics detector housed 100 meters underground in the Swiss side of the LHC, next to the main CERN campus. The first letter of intent for a new general-purpose detector which would be placed inside the LHC was submitted at CERN in 1992 [49] followed by the approval of CERN Council in 1997. In 2006 it started its test operation and during 2009-2012 it performed the first round of data-taking. After the 3 year long LHC shutdown for maintenance and upgrade, ATLAS restarted operating on April 2015 for a scheduled 3 years run.

The data analysed for the scope of this thesis were obtained during the first run of ATLAS, therefore the detector description of that time will be detailed.

The high amount of particle collisions in the LHC requires that the ATLAS detector comprises electronics and sensor elements which are both fast and radiation-hard. In addition, due to the high particle fluxes and the possibility of having overlapping events, high granularity is needed from the detector. Geometrically, a large acceptance in pseudorapidity with almost full azimuthal angle coverage increases the decay topology and the probability to detect an unidentified new physics signature.

For the particles detected, a good momentum resolution and reconstruction efficiency in the inner tracker are important. Furthermore, efficient calorimetry for electron and photon identification, complemented by hadronic calorimetry for accurate jet and missing transverse energy measurements, are essential. For muons, the requirements are good identification and momentum resolution over a wide range of momenta and the ability to determine the charge of muons with high transverse energy. Lastly, for the detector operation, a highly efficient triggering on objects with low transverse-momentum and sufficient background rejection is an essential goal to achieve an acceptable trigger rate for physics processes.

The ATLAS Detector has an extended diameter of 25 m, length of 46 m and weighs 7000 tonnes. A graphical representation of ATLAS is shown in Figure 2.4. ATLAS comprises three main sub-detector parts: **1) The Inner Detector, 2) The Electromagnetic and Hadronic Calorimeters and 3) The Muon Spectrometer**. The sub-detector parts are arranged concentrically with almost full solid angle coverage and forward-backward detection symmetry. Schematically, a thin superconducting solenoid encompasses the Inner Detector cavity, while three large superconducting toroids (1 barrel and 2 end-caps) are arranged around the calorimeters and the muon detectors, ensuring the generation of a magnetic field with 8-fold azimuthal symmetry. The innermost component of ATLAS, which is closest to the proton beam, is the Inner Detector (ID) and is surrounded by a 2T solenoid magnetic field. The Inner Detector, with its dedicated components, is responsible for measuring the tracks of the particles. Outside the solenoid, two groups of calorimeters exist: the liquid-argon (LAr) electromagnetic sampling calorimeter and the scintillator-tile hadronic calorimeter (TileCal), which are responsible for energy deposition measurements. The outer sub-part of the detector is the Muon Spectrometer, where the muons momentum is measured. A fast-processing trigger, divided in three levels, looks for events which will be further processed for physics analysis.

2.3.1 Geometrical characteristics - Coordinates system

ATLAS employs a right-handed Cartesian coordinates system. The z-axis of the coordinates system follows the beam-pipe with the positive side pointing towards Geneva. The perpendicular plane on the beam defines the x-y plane, with the positive x-axis starting from the Interaction Point pointing inwards the LHC ring, and the positive y-axis pointing upwards.

The layout of the detector ensures cylindrical symmetry and thus the use of cylindrical coordinates (ϕ, θ, R) is favoured.

The azimuthal angle ϕ is defined as the angle around the beam-pipe. The values are $\phi = 0$

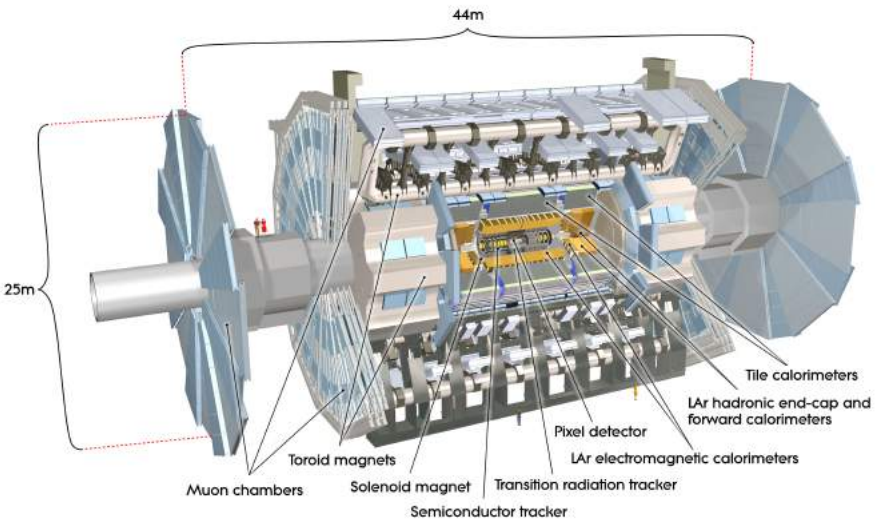

Figure 2.4: The ATLAS detector with the sub-detector systems. Figure from [50]

for the x-axis and $\phi = \pi/2$ for the positive y-axis with maximum values $\phi \in [-\pi, \pi]$. The polar angle θ equals $\theta = 0$ for the positive z-axis, with values range $\theta \in [0, \pi]$. The transverse distance from the z-axis is defined as radius R. An overview of the ATLAS coordination system is presented in Figure 2.5.

The momentum of a particle in cartesian coordinates is expressed as:

$$|\vec{p}| = \sqrt{p_x^2 + p_y^2 + p_z^2} \tag{2.2}$$

The transformation from cartesian to cylindrical coordinates system is achieved through:

$$\tan\phi = \frac{p_x}{p_y} \quad \text{and} \quad \tan\theta = \frac{\sqrt{p_x^2 + p_y^2}}{p_z} \tag{2.3}$$

In the head-on collisions, the momentum of the colliding partons is unknown. Therefore, a quantity is needed which is Lorentz invariant under boosts on the z-axis and can translate the position of the produced particles to the centre-of-mass frame.

The Lorentz invariant parameter is called ***pseudorapidity*** *(η)*, which can describe the position of the particles, and defined as:

$$\eta = -\ln\tan\frac{\theta}{2} = -\frac{1}{2}\ln\frac{|\vec{p}| + p_z}{|\vec{p}| - p_z} \tag{2.4}$$

At the beam direction $\eta \to \pm\infty$, whereas perpendicularly (at the x-y plane) equals $\eta = 0$. Pseudorapidity can describe the position of massless objects, whereas for massive objects, the

Lorentz invariant quantity ***rapidity*** *(y)* is used. In the relativistic limit where $pc \gg mc^2$ the two variables are equal. The rapidity is defined as:

$$y = \frac{1}{2} \ln \frac{E + p_z}{E - p_z} \tag{2.5}$$

Distances in the $\eta - \phi$ space equal the radius R:

$$\Delta R = \sqrt{\Delta\phi^2 + \Delta\eta^2} \tag{2.6}$$

The transverse plane is used for studying head-on particle collisions, since the collisions occur there at rest and the total momentum equals zero. The transverse momentum p_{T} and transverse energy E_{T} can be defined as:

$$p_{\mathrm{T}} = \sqrt{p_x^2 + p_y^2} = |\vec{p}| \times \sin\theta \tag{2.7}$$

$$E_{\mathrm{T}} = E \times \cos\theta \tag{2.8}$$

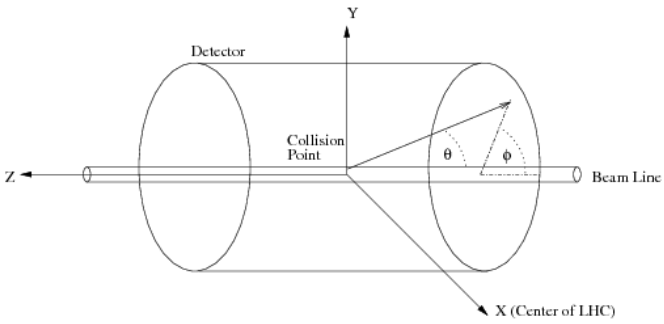

Figure 2.5: The ATLAS detector coordination system. Figure from [51]

Every charged particle track in ATLAS is characterised by a set of 5 variables defining the position and the direction. The point of the particle's trajectory with the minimum distance from the Interaction Point (IP) is chosen. The polar angle $\boldsymbol{\theta}$ and the azimuthal angle of the momentum vector $\boldsymbol{\phi_0}$ at this point are defined. The ratio of the charge with the momentum magnitude $\mathbf{q/p}$ shows the bending of the track. Two additional parameters are: the transverse impact parameter $\boldsymbol{d_0}$, which is the distance of the closest-approach point to the IP, and the longitudinal impact parameter $\boldsymbol{z_0}$, which is the distance of the closest-approach point to the z-axis. A schematic representation of the track's coordinates system is shown in Figure 2.6.

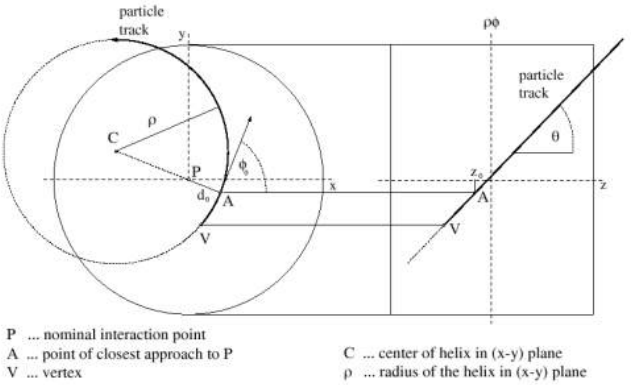

Figure 2.6: Coordination definitions for an ATLAS track. Figure from [52]

2.3.2 Magnet System

The ATLAS magnet system comprises four large superconducting magnets. The main components are:

- A central solenoid aligned with the beam axis

- A barrel toroid and two end-cap toroids

The central solenoid is 5.8m long and has an outer diameter of 2.56m. It consists of a single coil of 5.7 tonnes mass and operates with 7.73 kA current. It encloses the inner detector and is surrounded by the calorimeters, A 2 T axial magnetic field is provided for the inner detector from the solenoid. A full charging or discharging of the solenoid is achieved in 30 mins, while one day is needed for cooling down to 4.5K.

The barrel toroid comprises eight coils encased in stainless steel vacuum vessels. It is 25.3m in length, 20.1m diameter and 830 tonnes weight. The operating current is 20.5 kA and provides a torodial magnetic field of 0.5 T for the muon detector in the central region.

Similarly, the two end-cap toroids are 5m in length, 10.7m in diameter and 240 tonnes in weight. Each of the end-cap toroids contains eight coils. Their main purpose is to optimise the bending power at the end-cap regions of the muon spectrometer, by generating a magnetic field of 1 T. The nominal current under which they operate is 20.5 kA.

Overall, the magnetic system is 22 m in diameter, 26 m in length, with an overall volume of 12000m^3 and a stored magnet energy of 1.6 GJ. The conductors of all the components are aluminium stabilised Nb/Ti for the solenoid and Nb/Ti/Cu for the toroids. An overview of the ATLAS magnetic field is illustrated on Figure 2.7.

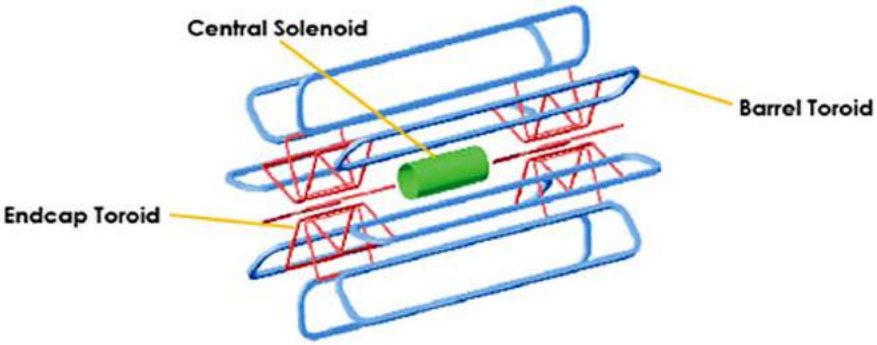

Figure 2.7: Graphical representation of the ATLAS magnet system. Figure from [48]

2.3.3 Inner Detector - Tracking

The Inner Detector of ATLAS is the first apparatus where particle detection takes place. The main operating goals of the Inner Detector are: a fine-granularity position measurement, precise momentum and interaction vertex resolution measurements, and charged particle identification. For this reason, a fine and high detector granularity at the collision vertex is needed to achieve precise measurements.

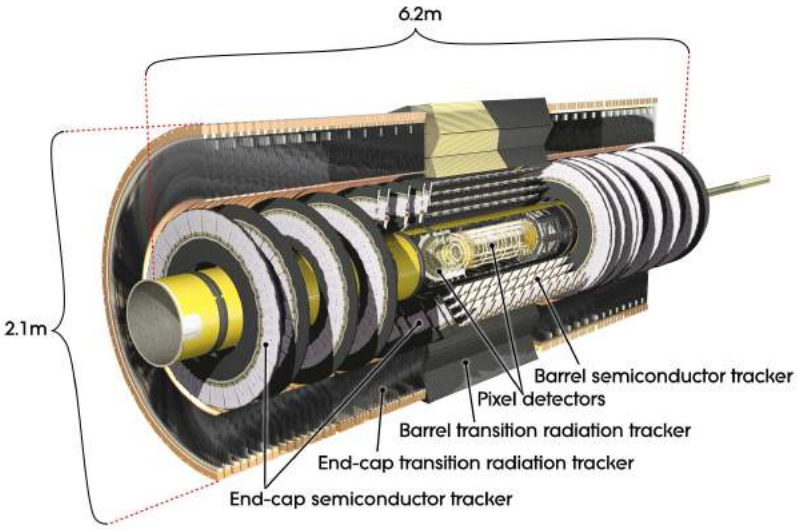

Figure 2.8: Graphical representation of the ATLAS Inner Detector. Figure from [48]

The Inner Detector lies within the 2 T magnetic field generated by the central solenoid. The operation area covers the full ϕ space, whereas in pseudorapidity it can detect particles with minimum energy 0.1 - 0.5 GeV up to $|\eta| < 2.5$. An overview is shown in Figure 2.8. The resolution performance target for the Inner Detector is $\sigma p_T / p_T = 0.05\%\ p_T \oplus 1\%$.

Three independent sub-detectors system constitute the full Inner Detector system:

The **silicon semiconductor pixel (Pixel)** and the **silicon strip tracker (SCT)** are used at small radii for high-precision measurements in the R-ϕ and z coordinates up to $|\eta| \leq 2.5$. At outer radii, **transition radiation trackers (TRT)** are used complementary to the Pixel and SCT for pattern recognition and also for momentum measurements up to $|\eta| \leq 2$.

The innermost Pixel tracking sensors are the closest to the beam-pipe. They offer precise tracking and vertex reconstruction which is important for jet-tagging. At the barrel region, there are three cylindrical layers. At the end-caps, two sets of three disks perpendicular to the beam axis exist.

The SCT tracking sensors are located after the pixel sensors.The barrel component is made of four doublet layers of silicon strips providing eight hits and four space-points for a transversing track. The end cap components are made of two sets of nine disks. The SCT is measuring coordinates in both the angular (R-ϕ) and longitudinal (z) plane and provides information about the impact parameter measurements.

The TRT are the outermost sub-system of the Inner Detector. They comprise drift (straw) tubes which detect transition radiation from charged particles. The main contribution of the TRT is improvement in electron identification. The detection of transition-radiation photons and the energy absorbed from them, differentiates between pions and electrons. Also, more precise momentum measurements are achieved for the charged particles.

The quality of the detection is based on the number of track hits at each station. ATLAS considers that every good track should cross 3 pixel layers, 8 strip layers and 36 straw hits[48]. The accuracy of all the Inner Detector components is presented on Table 2.2.

Table 2.2: Accuracy of the ATLAS Tracking components

Component	Accuracy (μm)
Pixel	
Barrel	10(R-ϕ)× 115(z)
End-cap	10(R-ϕ)× 115(R)
SCT	
Barrel	17(R-ϕ)× 580(z)
End-cap	17(R-ϕ)× 580(R)
TRT	
	130 (R-ϕ)

A plan view of the ATLAS Inner Detector components, with the respective coordinates and positions, is shown in Figure 2.9:

2.3.4 Calorimetry

The calorimetry system is essential for every particles detector where the energy deposition is used for energy measurement. The importance of precision measurements of electron and

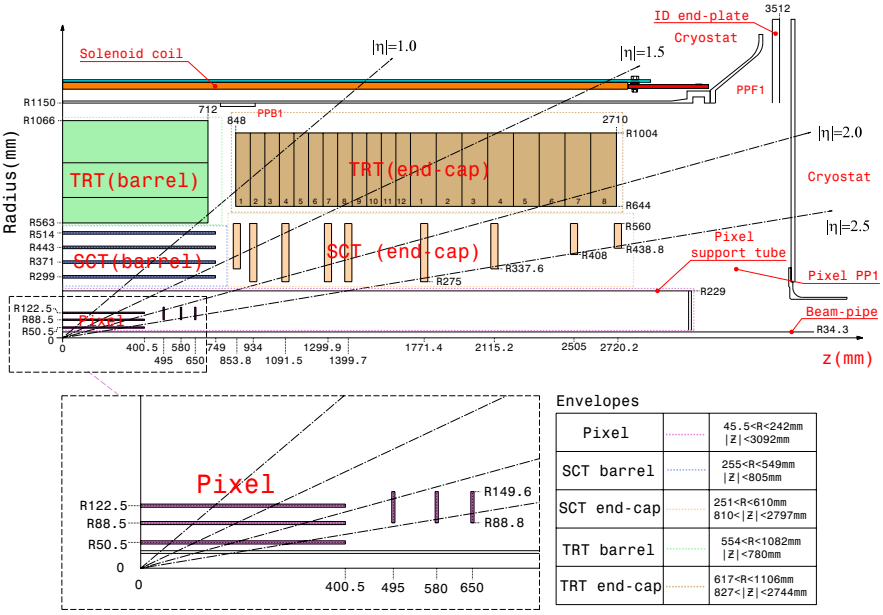

Figure 2.9: Plan view of a quarter-section of the ATLAS inner detector showing each of the major detector elements with its active dimensions and envelopes. Figure from [48]

photon energy, jet reconstruction and $E_{\mathrm{T}}^{\mathrm{miss}}$ measurements, leads to a heightened need for an efficient working calorimetry system.

ATLAS calorimeter system encompasses almost full detector coverage, fine granularity, segmentation in depth and good response. All of these features ensure good containment of the energy showers with precise energy measurement and uniform resolution.

Two separated calorimeters are employed. The Liquid Argon Electromagnetic Calorimeter (LAr EM Cal) and three calorimeters for hadronic showers (Tile Calorimeter, LAr Hadronic end-cap, LAr Forward). The EM calorimeter has total thickness more than 22 radiation lengths (X_0) [1] in the barrel and more than 24 radiation lengths in the end-caps. The hadronic calorimeter has thickness of 9.7 interaction lengths (λ) [2] in the barrel and 10 interaction lengths in the end-caps, including 1.3 λ from the outer support.

The calorimeters are accommodated in three aluminium cryostats: one barrel cryostat which contains the LAr EM calorimeter and the two end-caps where the LAr EM end-cap, the LAr Hadronic end-cap and the LAr Forward Calorimeter are located. Outside, they are surrounded by the scintillator tiles of Tile Hadronic Calorimeter, which contains one central barrel part and two extended barrel parts.

The energy resolution performance goal for electrons and photons at the Electromagnetic

[1] The radiation length X_0 is both (a) the mean distance over which a high-energy electron loses all but 1/e of its energy by bremstrahlung, and (b) $\frac{7}{9}$ of the mean free path for pair production by a high-energy photon. [17]

[2] The interaction length λ is the mean free path distance over which a nuclei will interact with matter producing new lighter nuclei. [17]

Calorimeter is $\sigma_E/E = 10\%/\sqrt{E} \oplus 0.7\%$. For jets, the desired energy resolution at the Hadronic Calorimeter components is $\sigma_E/E = 50\%/\sqrt{E} \oplus 3\%$ at the barrel and end-cap, and $\sigma_E/E = 100\%/\sqrt{E} \oplus 10\%$ at the forward region.

An overall representation of the ATLAS Calorimetry system is shown in Figure 2.10 and the total amount of interaction length (λ) for the calorimeter is shown in Figure 2.11.

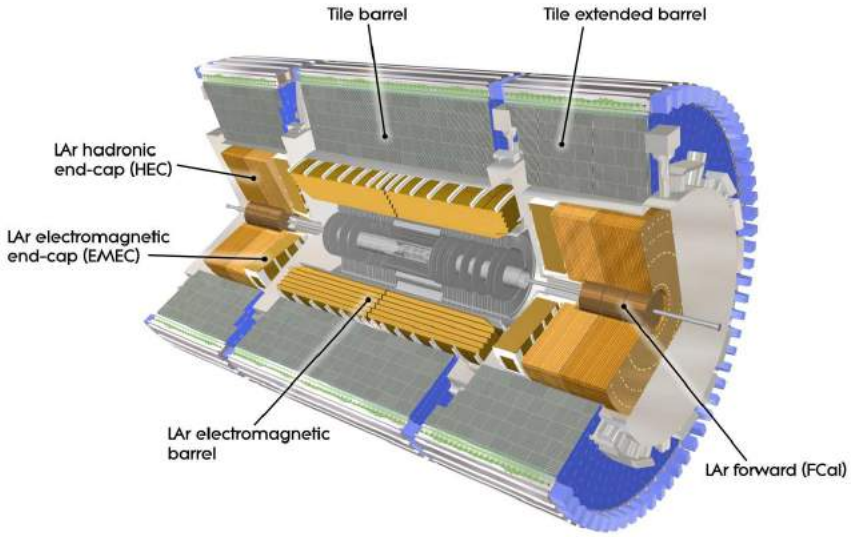

Figure 2.10: Cut-way view of the ATLAS calorimeter system. Figure from [48]

2.3.4.1 Electromagnetic calorimeter

The electromagnetic calorimeter comprises two components. The barrel part, which covers the pseudorapidity area ($|\eta| < 1.475$), and two end-cap parts, which cover the region ($1.375 < |\eta| < 3.2$). Liquid Argon (LAr) is used as active material and lead as passive material.

The barrel part is split in two halves at z = 0, with a 4mm gap for services.Every half barrel is divided in 16 modules each covering $\Delta\phi$ angle = 22.5°. A single module is segmented in three layers in depth, each following a special accordion geometry. This selection offers total coverage in space with fast signal extraction due to the modularity. The accordion-shaped electrode layers are made from the polymer kapton, axial with the respect to the beam, expanding in the ϕ-space and keeping the liquid-argon gap constant between them.

The end-cap component of the EM calorimeter wheel is segmented into three disk layers at the region $1.375 < |\eta| < 2.5$. The same accordion geometry with similar granularity as the barrel components is followed. At the forward region of $2.5 < |\eta| < 3.2$ the wheel is segmented into two layers of coarser granularity, tolerable for cases where extended acceptance is needed.

In the pseudorapidity region $|\eta| < 1.8$, the LAr presampler detector layer is located. The

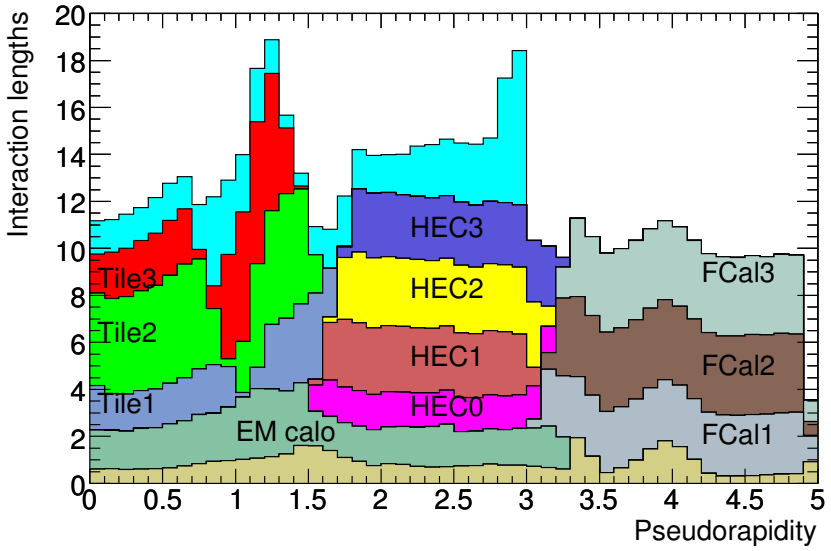

Figure 2.11: Cumulative amount of material, in units of interaction length, as a function of $|\eta|$, for all the calorimetry components. Figure from [48]

presampler provides information about energy losses in the material upstream of the calorimeter.

An image of the barrel module is shown in Figure 2.12. The three longitudinal layers have different granularity, serving multiple purposes. The first layer (closest to the interaction point) has the highest granularity and small thickness. It is able to discriminate EM showers of single isolated photons from multiple ones, produced after hadronic decays in jets. Also, it is used for precise position measurements by measuring the pseudorapidity of the impact point and the photon direction. The second layer (middle) has coarser granularity and the highest thickness. The largest fraction of the shower energy is absorbed at this layer. The third layer (back) has the coarsest granularity and the smallest thickness. It measures the tails of the electromagnetic shower and longitudinal energy leakage before the hadronic calorimeter.

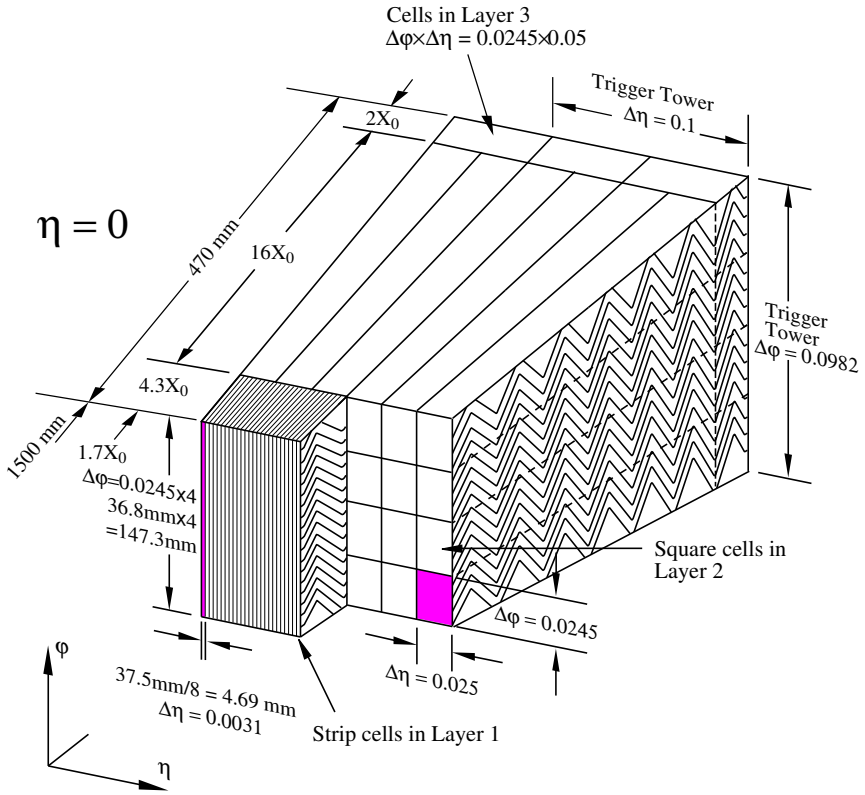

Figure 2.12: Sketch of the barrel module of ATLAS EM calorimeter, where the three layers of the different granularity are shown. Figure from [48]

The main parameters of the ATLAS Electromagnetic system are listed in Table 2.3.

2.3.4.2 Hadronic calorimeter

For particle showers originating from hadrons and heavy flavour quarks, the hadronic calorimeter is employed with three respective components: Tile, LAr Hadronic End-Cap and LAr Forward. A schematical representation of the hadronic calorimeter components is shown in Figure 2.13.

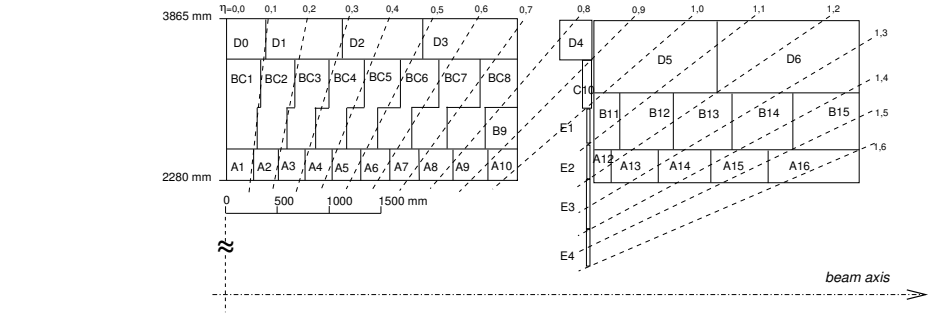

(a) Tile calorimeter (central and extended)

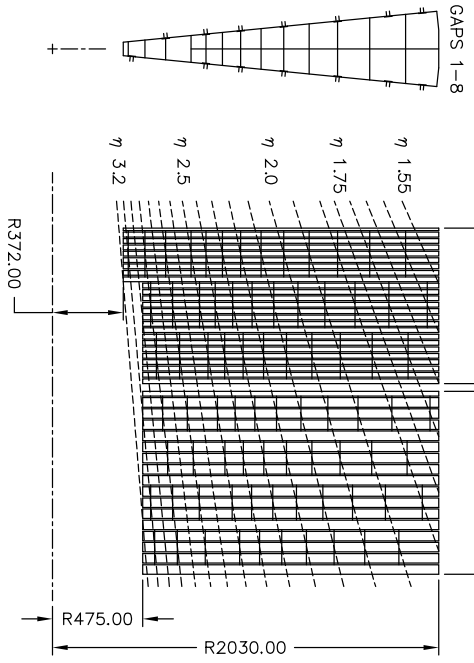

(b) HEC

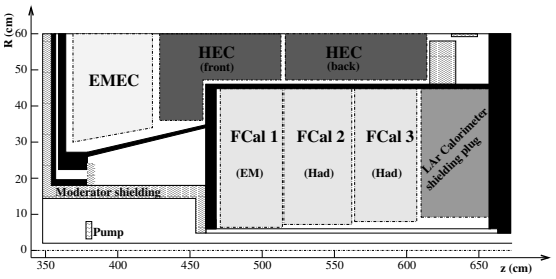

(c) FCal

Figure 2.13: Segmentation and schematic view of the Hadronic Calorimeter components. (a) TileCal central and extended, (b) LAr Hadronic End-cap and (c) LAr Forward Calorimeter. Figures from [48]

Component	Barrel	End-caps		
Number of Layers and $\|\eta\|$ region coverage				
Presampler	1	< 1.52	1	$1.5 < \|\eta\| < 1.8$
Calorimeter	3	< 1.35	2	$1.375 < \|\eta\| < 1.5$
	2	$1.35 < \|\eta\| < 1.475$	3	$1.5 < \|\eta\| < 2.5$
			2	$2.5 < \|\eta\| < 3.2$
Granularity $\Delta\eta \times \Delta\phi$ in $\|\eta\|$ space				
Presampler	0.025×0.1	< 1.52	0.025×0.1	$1.5 < \|\eta\| < 1.8$
Calorimeter 1st layer	$0.025/8 \times 0.1$	< 1.40	0.050×0.1	$1.375 < \|\eta\| < 1.425$
	$0.025/8 \times 0.025$	$1.40 < \|\eta\| < 1.475$	0.025×0.1	$1.425 < \|\eta\| < 1.5$
			$0.025/8 \times 0.1$	$1.5 < \|\eta\| < 1.8$
			$0.025/6 \times 0.1$	$1.8 < \|\eta\| < 2.0$
			$0.025/4 \times 0.1$	$2.0 < \|\eta\| < 2.4$
			0.025×0.1	$2.4 < \|\eta\| < 2.5$
			0.1×0.1	$2.5 < \|\eta\| < 3.2$
Calorimeter 2nd layer	0.025×0.025	< 1.40	0.050×0.025	$1.375 < \|\eta\| < 1.425$
	0.075×0.025	$1.40 < \|\eta\| < 1.475$	0.025×0.025	$1.425 < \|\eta\| < 2.5$
			0.1×0.1	$2.5 < \|\eta\| < 3.2$
Calorimeter 3rd layer	0.050×0.025	< 1.35	0.050×0.025	$1.5 < \|\eta\| < 2.5$
Readout channels - For both side in end-caps				
Presampler	7808		1536	
Calorimeter	101760		62208	

Table 2.3: Main parameters of the electromagnetic calorimeter system

Tile Calorimeter - TileCal

The Tile Calorimeter is the next calorimetric layer after the EM calorimeter. It consists of a barrel component covering the region $|\eta| < 1.0$ and two extended barrels each covering the region $0.8 < |\eta| < 1.7$. Both components are segmented into three longitudinal layers. Each barrel contains 64 modules where steel is used as the absorber and scintillator as the active medium. The operation principle is based on ionising particles either crossing or being produced in the tile and induce ultraviolet scintillation light from the active material. Wavelength-shift fibres read out the two sides of the tiles and transmit to two separate photo-multiplier tubes.

LAr Hadronic end-cap calorimeter - HEC

The hadronic end-cap calorimeter's position is behind the EM end-cap calorimeter. The pseudorapidity region for the HEC is $1.5 \leq |\eta| \leq 3.2$. It consists of two independent wheels per end-cap cryostat. Each wheel is constructed from 32 modules and is divided into two longitudinal layers. The calorimeter utilises liquid argon as active material and copper as passive material.

LAr Forward calorimeter - FCal

The Forward calorimeter is located inside the end-caps cryostats, covering the forward pseudorapidity region of $3.1 < |\eta| < 4.9$. The position of the forward calorimeter has a twofold

purpose. The detection of either electromagnetic or hadronic showers at high-$|\eta|$ regions offering a full $|\eta|$ space coverage for the calorimetry system. Also, it minimises the background and radiation levels, due to the high particle flux in this region, for the Muon Spectrometer which is positioned next. The FCal comprises three modules in each end-cap. The first (FCal1) uses copper as the passive medium and has electromagnetic function where the other two (FCal2,FCal3) have hadronic function and use tungsten as the passive medium which ensures a reduced spread of the hadronic jet. The calorimeter consists of longitudinal array with electrodes containing rods and tubes (coopper or tungsten) parallel to the beam.

An overview of the main parameters of the hadronic calorimeter is listed in Table 2.4.

	Barrel	End-caps	
LAr hadronic end-cap - HEC			
$\|\eta\|$ coverage		$1.5 < \|\eta\| < 3.2$	
Layers		4	
Granularity		0.1×0.1	$1.5 < \|\eta\| < 2.5$
		0.2×0.2	$2.5 < \|\eta\| < 3.2$
Readout channels		5632	
LAr forward calorimeter - FCal			
$\|\eta\|$ coverage		$3.1 < \|\eta\| < 4.9$	
Layers		3	
Granularity $\Delta\phi \times \Delta y$ (cm)		FCal1: 3.0×2.6	$3.15 < \|\eta\| < 4.30$
		FCal1: 4× finer	$3.10 < \|\eta\| < 3.15$
			$4.30 < \|\eta\| < 4.83$
		FCal2: 3.3×4.2	$3.24 < \|\eta\| < 4.50$
		FCal2: 4× finer	$3.20 < \|\eta\| < 3.24$
			$4.50 < \|\eta\| < 4.81$
		FCal3: 5.4×4.7	$3.32 < \|\eta\| < 4.60$
		FCal3: 4× finer	$3.29 < \|\eta\| < 3.32$
			$4.60 < \|\eta\| < 4.75$
Readout channels		3524 (both sides)	
Tile Calorimeter - TileCal			
	Barrel	Extended Barrel	
$\|\eta\|$ coverage	< 1.0	$0.8< \|\eta\| <1.7$	
Layers	3	3	
Granularity $\Delta\phi \times \Delta\eta$	0.1×0.1	0.1×0.1	
		0.2×0.1 (last layer)	
Readout channels	5760	4092 (both sides)	

Table 2.4: Main parameters of the hadronic calorimeter system

2.3.5 ATLAS Muon Spectrometer

The Muon Spectrometer (MS) is the outer part of the ATLAS detector. The main purpose of the spectrometer is to measure the momentum of muons after exiting the barrel and end-cap calorimeter components. The principle of the measurement is based on the muon track bending due to the magnetic field generated by the toroids at the inner part of the detector.

The three large air-core toroid magnets of the ATLAS magnet system are responsible for the generation of the magnetic field: the barrel and the two end-cap toroids. The barrel toroid is accommodated in eight individual cryostats, placed radially and symmetrically around the beam axis. The two end-caps toroids comprise eight coils each are inserted in the barrel toroid and line up with the central solenoid. The magnetic field is orthogonal to the muon trajectories, ensuring the maximum deflection from the original track.

At pseudorapidity region of $|\eta| < 1.4$, the barrel toroid creates the magnetic field, whereas in the region $1.6 < |\eta| < 2.7$, the end-cap magnets are responsible for the magnetic field. The special region of $1.4 < |\eta| < 1.6$ is called the "transition region", where the barrel and the end-cap toroids are combined for the creation of the magnetic field.

An overall representation of the ATLAS Muon Spectrometer is shown in Figure 2.14 and the cross-sections perpendicular and parallel to the beam axis are shown in Figure 2.15.

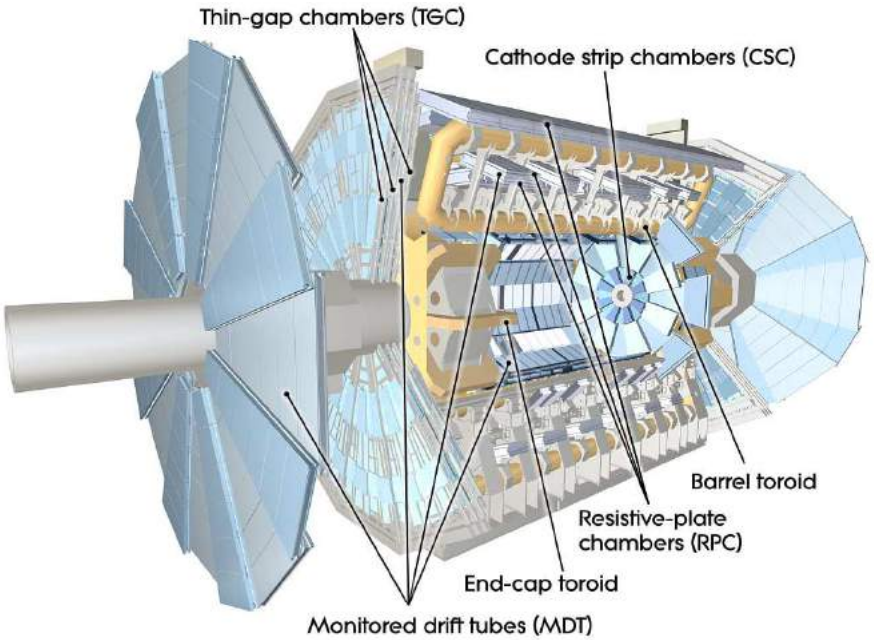

Figure 2.14: Schematic representation of the ATLAS Muon Spectrometer. Figure from [48]

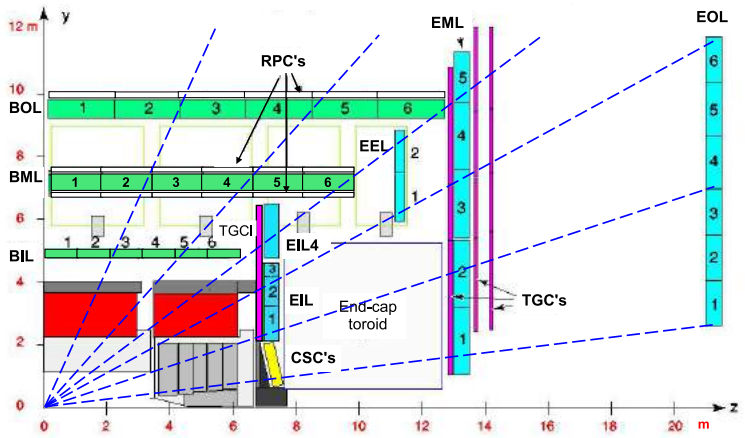

Figure 2.15: Cross-section of the muon system in a plane containing the beam axis (bending plane). Infinite-momentum muons would propagate along straight trajectories which are illustrated by the dashed lines and typically traverse three muon stations. Figures from [48]

2.3.5.1 Muon spectrometer chambers

There are four separate sets of chambers. The Monitored Drift Tube chambers (MDT) and the Cathode-Strip Chambers (CSC) are used for tracking and momentum measurement. The Resistive Plate Chambers (RPC) at barrel and the Thin Gap Chambers (TGC) at the end-caps are used for fast triggering.

At the barrel region, the chambers are arranged in three cylindrical layers around the beam axis, whereas at the transition and end-cap region they are installed in planes perpendicular to the beam axis.

Tracking and momentum chambers

An excellent muon momentum resolution is required from the ATLAS Muon Spectrometer. For example, a muon track with 1 TeV momentum has track sagitta $\approx 500\ \mu m$ at the barrel and 1mm at the end-cap. Therefore, the 10% p_T uncertainty at 1 TeV which is the ATLAS MS performance goal, constrains the error on sagitta to be less than 50 μm.

Monitored Drift Tubes - MDT:

The MDT chambers cover the pseudorapidity region up to $|\eta| < 2.7$, apart from the innermost layer, where they function up to $|\eta| < 2.0$. Every pressurised drift tube has a mixture of gas Ar/CO_2 at 93:7 ratio, ensuring good ageing properties and providing a resolution of 80μm.As the muon transverses the tube and ionises the gas, under the radial electric field, the

ions drift towards the anode and a hit signal is recorded.

A cross-section of a MDT tube and the mechanical structure are shown in Figure 2.17. The chambers have a rectangular shape at the barrel and a trapezoidal shape at the end-caps. Each chamber consists of two groups of tube layers (multi-layers) and each multi-layer contains normally three tube layers. Apart from the $|\eta| < 2.0$ region where they contain four layers, for better pattern recognition. The combination of the multilayers yields a spatial resolution of $35\mu m$ for the three layers chambers and $30\mu m$ for the four layers chambers. After the final detector configuration in 2009, there have been 1150 MDT chambers.

Cathode-strip Chambers - CSC:

The CSC chambers operate at the pseudorapidity region $2.0 < |\eta| < 2.7$, located at the end-caps. The configuration of the CSC comprises two disks each with eight small and eight big chambers, resulting to a total number of 32 chambers, with every chamber containing four CSC planes. A layout of the CSC end-cap is shown in Figure 2.18. This configuration ensures a very precise information is for every track, since there are four independent measurements at $|\eta|$ and ϕ.

The operation technique for CSC is based on multiwire proportional chambers, with the wires aligned in the radial direction. The segmentation of the cathodes follows two orthogonal approaches. One with the strips perpendicular to the wires, to provide the precision coordinate at the bending plane, and the other with the strips parallel to the wires to provide the transverse coordinate. The exact position is given through interpolation between the charge around neighbouring cathode strips. The resolutuion provided by the CSC is 60 μm.

The CSC are placed in a particular region of the detector, where the particle flux is high. However, the operating principle of the chambers, having a good track resolution and the pair of coordinates measurements ($|\eta|$ and ϕ space), provides excellent distinction between different tracks, able to overpass the high background rates.

Trigger chambers

A fast responsive muon trigger system is needed in order to seed the main ATLAS trigger system with the muon track multiplicity and an approximative muon energy.The trigger chambers should have a significantly faster response than the bunch crossing (25ns). Two sets of trigger chambers are used which provide measurements in both $|\eta|$ and ϕ planes. An overview of the Muon trigger system is shown in Figure 2.16.

The region $1.3 \leq |\eta| \leq 1.65$ is excluded from triggering, due to the inhomogenious magnetic field resulting from the combined B-fields of the barrel and end-cap toroid. This results to straight muon tracks, faking muons with high momentum.

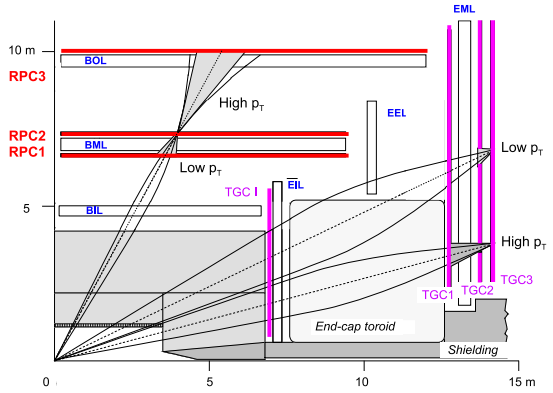

Figure 2.16: Schematics of the muon trigger system. RPC2 and TGC3 are the reference (pivot) planes for barrel and end-cap, respectively. Figure from [48]

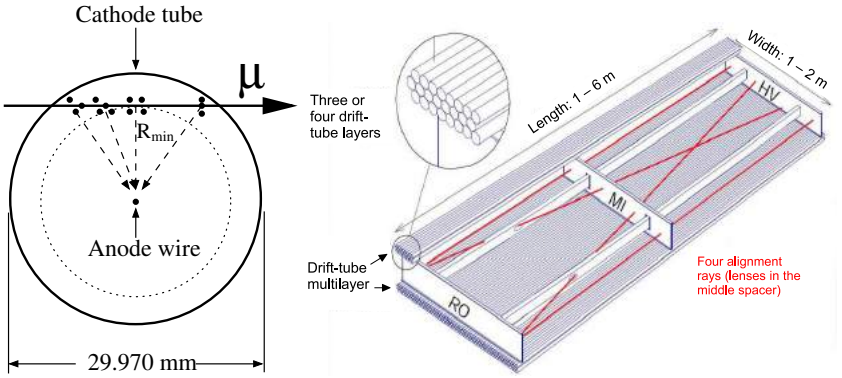

Figure 2.17: (a) Cross-section of the MDT tube. (b) Mechanical structure of a MDT chamber. Figures from [48]

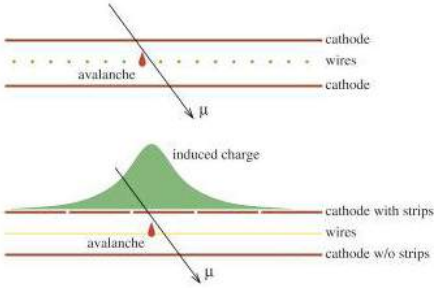

Figure 2.18: Layout of a CSC unit. Figure from [53]

Resistive Plate Chambers - RPC:

The RPC are located at the barrel region ($|\eta| < 1.05$). Every chamber has two rectangular detectors, each containing two independent detection layers. Every layer is made of two resistive plates with a gas gap of 2mm, without the presence of wires. A mixture of organic gases fills the gap between the plates. The muon p_T range which is selected by the RPC triggerring system is 6 to 35 GeV. At the last detector configuration, the Muon Spectrometer contained RPC 606 chambers.

Thin Gap Chambers - TGC:

The TGC are placed at the end-caps ($1.05 < |\eta| < 2.7$) and they complement the coordination measurements with the MDT. They are positioned in two groups. The innermost (small wheel) is at $1.05 < |\eta| \leq 1.92$ with two non-overlapping planes and the big wheel is at the region $1.05 \leq |\eta| \leq 2.7$ (big wheel- MDTs middle station), with three planes outside the end-cap toroid. An overview of the TGC structure is shown in Figure 2.19.

At the small wheel, each plane has two layers of two TGC. At the big wheel, there is one plane of a triplet chamber and two layers of doublet chambers, yielding overall seven detection layers at this region (See Figure 2.16). However, only the region up to $|\eta| = 2.4$ is used for triggering.

The TGC are multi-wire proportional chambers, with a variation of wire groups for fine granularity and high momentum resolution. The ϕ coordinate is read-out by the radial pick-up strips which cover the cathod planes, where the $|\eta|$ coordinate is read from the wires. The time resolution of the TGC is 25ns which ensures extraction of signal in less time than the proton bunch crossing. In total, there are 1578 TGC units assembled to 3588 chambers.

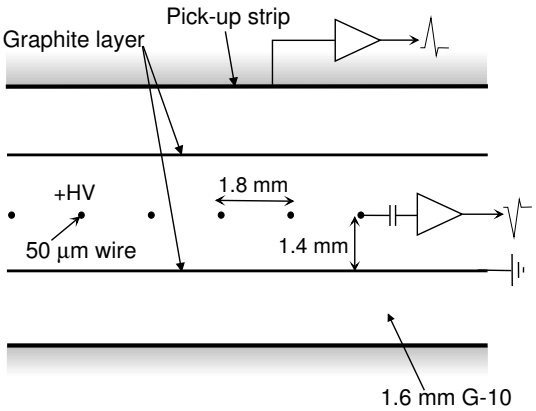

Figure 2.19: TGC structure showing anode wires, graphite cathodes, the thermosetting industrial fibre glass composite laminate (G-10) layers and a pick-up strip, orthogonal to the wires. Figure from [48]

2.3.6 Trigger and Data Acquisition

The LHC designed bunch crossing of 25ns (equivalent to rate of 40 MHz) requires from ATLAS the adoption of a fast and efficient trigger system, able to estimate the significance of the event before the next bunch crossing. ATLAS employs a three-level system for triggering: Level-1 (L1), Level-2 (L2), Event-Filter (EF). The last two levels, L2 and EF, have the collective name "High Level Trigger" (HLT). The trigger system follows a bottom-up approach, starting from L1 and ending on EF.

The Level-1 trigger is hardware based and uses information from the sub-detectors. It looks for physics objects (muons, electrons, photons, jets, tau decays to hadrons) with high transverse momentum. Various selections are applied to the objects called "trigger menus". The objects which pass the selection are transferred to the detector front-end and data-acquisition drivers, being formatted from digitised signals to raw data. Ultimately, the L1 triggers define a Region of Interest (RoI) in the $\eta - \phi$ space, where interesting features were detected and the objects passed the criteria. The RoI information is passed to the higher level triggers. The total event rate for L1 is 75 kHz with a decision latency of $2.5\mu s$.

The Level-2 trigger focuses on the RoIs seeded by the L1 trigger. It is software-based and uses the full detector data to investigate the corresponding RoIs ($\approx$ 2% of full detector data). The data are read from the buffers and the selected events are moved to the event-building system before being transferred to the next level. At L2, the event rate is reduced to 3.5 kHz and the processing time is 40ms.

The last level is the Event Filter which is also software-based. A full offline selection is applied on the L2 constructed event. After successful selection, the events are permanently stored at CERN's computing batch farm. The event rate is reduced to 200 Hz and the event process time at this level is 4 seconds.

During the data transfer, the software and hardware components are configured, controlled and monitored, in order to ensure the optimal data acquisition functionality.

ATLAS uses a special Detector Control System for the safe operation of the detector. An online monitoring is performed on the operational parameters like the high/low voltage systems, gas pressure, temperature, humidity and magnetic field. Also, it serves as front-end interface enabling automatic or manual corrections in case of unexpected behaviours. Additional, it achieves synchronisation between the data-taking and data-transferring operations and links the sub-detectors components with other independent systems, like the LHC accelerator or technical services.

Chapter 3

Physics objects reconstruction

The reconstruction of the physics objects is described in the present chapter. For a general-purpose detector like ATLAS, an efficient object reconstruction and identification is an essential target in order to proceed with physics studies. The objects which are searched might be charged particles tracks, primary and secondary vertices, electrons, photons, muons and hadronic jets.

3.1 Electrons and photons

Reconstruction:

The electrons and photons are characterised by energy deposits in the EM calorimeter. Additionally, photons can be detected from their conversions to electron pairs ($\gamma \rightarrow e^+e^-$) in the material prior to the calorimeter. The charged particles reach and ionise the LAr medium and a signal is extracted proportional to the energy. Therefore, clusters of calorimeter cells are formed with large energy deposits which are used for the electron and photon reconstruction in the region up to $|\eta| < 2.4$.

The energy deposit cells at the four longitudinal parts of the calorimeter are added. A grid is assumed with 200 $\times$ 256 energy towers of size $\Delta\eta \times \Delta\phi$ = 0.025×0.02, similar to the granularity of the calorimeter middle layer. For electrons and converted photons, the clusters are matched with at least one reconstructed track from the Inner Detector. In the case where no track matches the EM cluster, then the cluster is characterised as unconverted photon. A graphical representation of the cluster-track matching is shown in Figure 3.1.

The energy towers seed the standard ATLAS sliding-window algorithm [54] which searches for neighbouring energy deposits with $E_{\mathrm{T}} > 2.5$ GeV in window size of 3×5 energy towers.

After successful match with a track, the electron cluster is rebuilt. The reconstructed area is $\Delta\eta \times \Delta\phi = 3 \times 7$ cells of the second layer for the barrel, and 5×5 ($\Delta\eta \times \Delta\phi$) second layer cells at the end-caps.

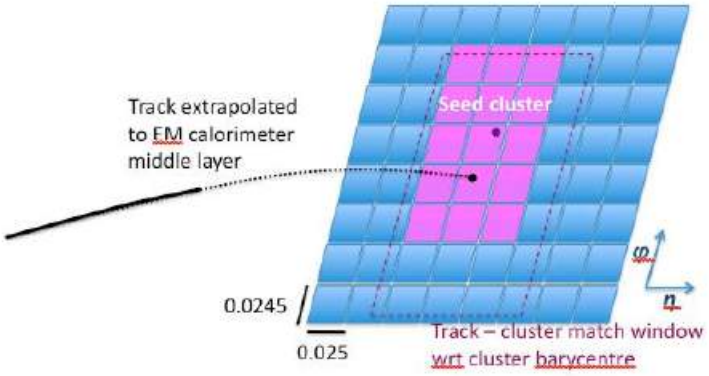

Figure 3.1: Representation of cluster formation. Figure from [55]

The reconstructed cluster area depends on the photon conversion. In the barrel, the cluster size is 3×5 ($\Delta\eta \times \Delta\phi$) for uncoverted photons and 3×7 ($\Delta\eta \times \Delta\phi$) for converted photons. The larger azimuthal angle takes into the account the separation between the conversion products. However, in the end-caps where the inner radius is smaller, both converted and unconverted photons use the cluster size of 5×5 ($\Delta\eta \times \Delta\phi$).

The size of the clusters area in the lateral dimension has been optimised in order to account for the different energy distribution at each layer and also to decrease the effect from pile-up and noise contribution [56]. To determine the cluster energy, additional correction factors are applied. These are computed by calibration after simulation and they are related to: the energy lost in the material upstream the calorimeter, the neighbouring energy cells overlapping with the cluster and the loses beyond the LAr Calorimeter (leakage). Figure 3.2 shows the evolution of a shower in the calorimeter.

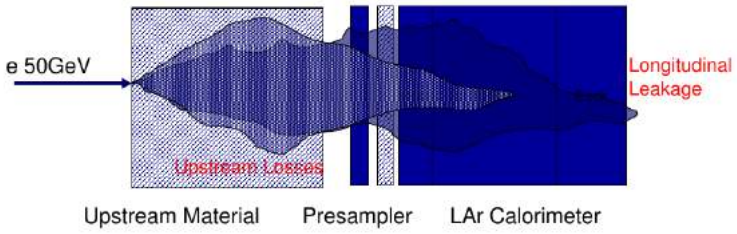

Figure 3.2: Evolution of an electromagnetic shower of an electron with 50 GeV energy in the EM calorimeter. Figure from [55]

Identification:

After successful reconstruction, the candidates have to be identified as real electrons or photons. Once identified, they can be distinguished from jets with large electromagnetic com-

ponents, which fake either an electron or a photon.

The expected shower profile at the EM calorimeter for the particles is provided by simulations. The longitudinal and transverse characteristics of the induced showers are examined for compatibility with the expected ones.

Many parameters are considered for the identification process: the EM shower shapes at the first and second layer of the calorimeter, the leakage into the hadronic calorimeter, the track quality and the impact parameter, the track-cluster matching, the ratio of high-threshold hits at the TRT over the total TRT hits and finally the ratio cluster energy over track momentum.[56]

Electrons: There are two approaches for the electron identification method. Either a selection which applies sequential cuts on discriminant variables or using the probability distrubtions of the variables, known as "likelihood method". Every method contains a set of cuts which apply stricter selections; For the cut-based method, the sets are: "loose,medium,tight,multilepton" and for the likelihood: "loose,medium, very tight" [57].

ATLAS uses the likelihood method as default. At this method, the Probability Distribution Functions (PDF) of the variables for signal and background are combined into a discriminant on which a selection is applied. Based on the uncorrelated PDFs, the probability is calculated for an object to be either signal or background. There are 9×6 sets of PDFs, divided into 9 $|\eta|$ bins and 6 E_{T} bins.

For the physics analyses detailed in the present thesis, the *Loose Likelihood* method has been employed, which uses information from: the hadronic leakage, the ratio of energy in every layer of the calorimeter over the total, the shower width, the hits on the tracker and track-cluster matching information. A full description of the variables is detailed in Appendix A.

Photons: The photon identification method is similar to that of electrons. However, for photons only two sets of cuts exist, the *loose* and the *tight* sets. The *loose* set is the same as electrons whereas the *tight* set focuses mainly on the optimisation of the identication for unconverted and converted photons. [58] The acceptance region for the photon identification is $|\eta| < 2.37$ with the "crack region" of the calorimeter ($1.37 < |\eta| < 1.52$) excluded.

For the non-collinear Final State Radiation photons studies, which are described on Chapter 5, the *tight* selection is used. This selection employs information from the hadronic leakage and the energy deposit ratios in every calorimeter layer. A full description of the photon identification variables is detailed in Appendix A.

3.2 Muons

During the p-p collisions at the LHC muons with a wide energy spectrum are produced. The Muon Spectrometer can provide precise muon momentum measurements and in combination with the Inner Detector and the Calorimeters, accurate muon identification can be performed.

The track reconstruction in the Muon Spectrometer follows a sequence of steps. Initially, a hit signal is extracted from the drifted electron in the MDTs and the charge clustering is

exctracted from the CSCs, RPCs and TGCs. An illustration of the drift-circle in a MDT tube is shown in Figure 3.3.

The next step is the creation of track segments. The track segments are defined as straight lines in the MDT or CSC stations. These are based on reconstructed patterns from combined either MDTs hits or CSCs charge clusters.

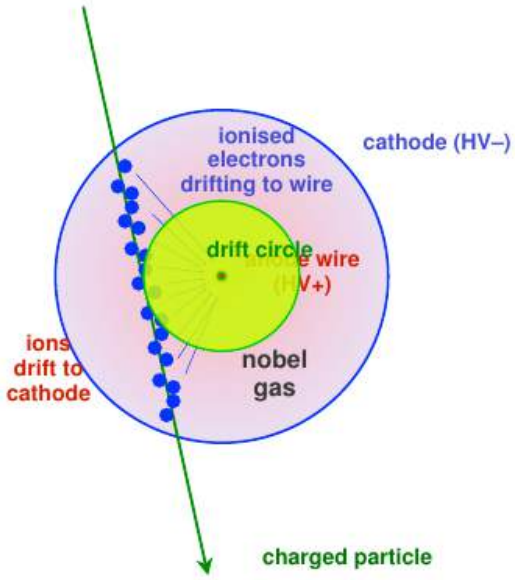

Figure 3.3: Drift circle in the MDT. Figure from [53]

The muon track is created by combining of track segments from the three stations. The track is seeded by the outer and middle station and then is extrapolated to the inner stations, searching for matches with the reconstructed segments there. After successful match, a track candidate is classified. Track fitting follows, which accounts for energy losses through the passive material and the magnetic field inhomogeneities. Lastly, the track is extrapolated back to the interaction point, matching hits at the Inner Detector, with additional momentum corrections due to minimum ionising particle behaviour in the calorimeter.

Figure 3.4 illustrates the track and segment finding in the Muon Spectrometer.

Based on the track reconstruction, the muon identification collections are separated into four categories [59]:

1. **Combined - (CB):** The track reconstruction is performed independently on the Inner Detector and Muon Spectrometer. The combined track is formed after successful combination of the two separate ones. The Combined set has the highest identification purity.

2. **Stand-Alone - (SA):** The muon trajectory is reconstructed only at the Muon Spectrometer at areas which are not covered by the acceptance of the Inner Detector (2.5< $|\eta|$ <2.7).

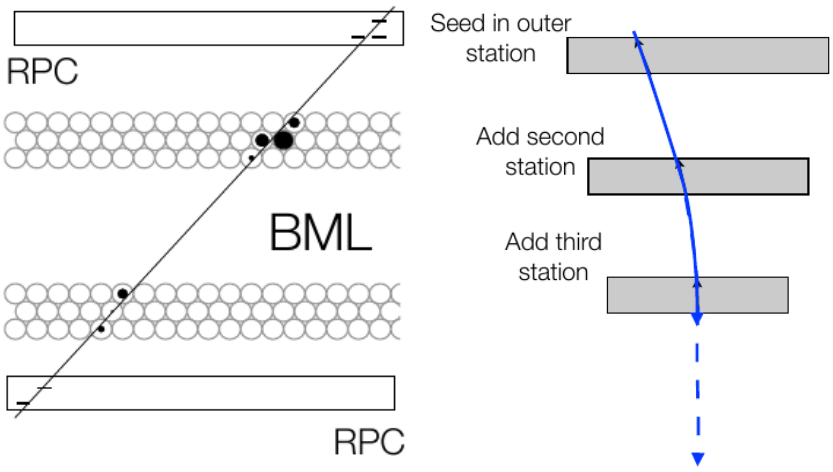

Figure 3.4: (Left) Local and (Right) global segment track search in the MS . The left figure represents a doublet of MDTs at the Barrel Middle Layer (BML) enveloped by a group or RPCs. The right figure represents the evolution of a track reconstruction at the three layers of TGCs. Figures from [53]

The direction and the impact parameter of the muon are defined by extrapolation to the interaction point.

3. **Segment-Tagged - (ST):** A track in the Inner Detector is characterised as muon if it is associated, after extrapolation to the Muon Spectrometer, at minimum with one track segment in the MDT or CSC. This method is applied on muons with low transverse momentum which do not fully cross the MS.

4. **Calorimeter-Tagged - (CaloTag):** If an Inner Detector track can be associated with energy deposit at the calorimeter which matches an expectation from a minimum ionising particle then it is considered as calorimetric tagged muon. The CaloTag collection has the lowest purity and is used for recovery at uninstrumented areas of the Muon Spectrometer ($|\eta| < 0.1$).

The strategies which are employed for the previous muon types classify the muons in two collections [59]:

- **Chain 1 - (STACO)**: A statistical combination of the MS-only and ID track parameters takes place, with the use of covariant matrices of the reconstructed tracks.

- **Chain 2 - (MUID)**: A global re-fit is performed on the muon track using hits from both ID and MS.

For the ATLAS Run-2 a single collection will characterise the muon candidates, **Chain 3 - (MUONS)**. This collection combines the techniques applied from both the old previous methods.

3.3 Jets

Based on the strong force properties and the colour confinement, it is impossible to observe either single quarks or gluons (collectively called, partons). Therefore, in collisions, the "free" partons instantly hadronise, creating a bunch of particles which is called a "jet".

In ATLAS, the energy deposits at the calorimeter cells are the main element which is employed as input for the jet clustering algorithms. For the Vector Boson Fusion part of the Heavy Higgs analysis described on Chapter 7, the jets were reconstructed from topological clusters [54] using the anti-$k_\perp$ [60] algorithm with distance parameter R = 0.4. A graphical representation of the jet production and the energy deposit is shown on Figure 3.5.

The topological clusters (topoclusters) method applies a reconstruction of three-dimensional energy deposits in the calorimeter. The "nearest-neighbours" algorithm is employed which groups neighbouring calorimeter cells above a specific minimum threshold. The condition is: $|E_{\text{cell}}| > N\sigma$, (N = 4 for primary seeds, 2 for secondary seeds), where E_{cell} is the calibrated cell energy and σ is the combined electronics and pile-up noise.

At final level, the jets are calibrated with the application of correction factors, so as the measured energy to correspond to the original energy of the hadrons, given that some energy deposits might not be recorded by the detector.[61]

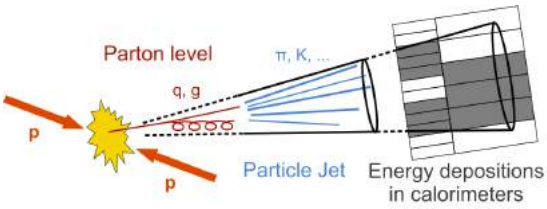

Figure 3.5: Jet production and energy deposit. Figure from [62]

3.4 Missing E_{T}

Based on the collision kinematics on the laboratory frame, the vector sum of the momentum should be zero on the transverse plane. If a particle passes undetected from the detector an imbalance of the energy at the transverse plane will be observed. The imbalance is called: "missing energy" ($E_{\text{T}}^{\text{miss}}$), and is defined as:

$$E_{\text{T}}^{\text{miss}} = -\sum_{i=0}^{N} p_{\text{T}i}$$

where N equals the total number of particles present at the interaction.

The transverse energy is calculated from the calorimeter cluster energy, after calibration with a signal scale based on the expected energy deposit of EM showers.[63].

Additionally, the $E_{\mathrm{T}}^{\mathrm{miss}}$ is important for SUSY searches, where hypothetical Lightest Supersymmetric Particles (LSP) are expected to have an experimental signature associated with high $E_{\mathrm{T}}^{\mathrm{miss}}$ [64]. A non-zero value for the $E_{\mathrm{T}}^{\mathrm{miss}}$ is also related with to the passing of a neutrino. The neutrino transverses the detector without any interaction. Apart from the study of known SM processes, the presence of a neutrino can be associated with Beyond the Standard Model phenomena like the proton decay ($\mathrm{p} \rightarrow K^{+} + \bar{\nu}$).

3.5 ATLAS Datasets

The data analysed in this thesis correspond to the 2012 ATLAS dataset. As mentioned in Chapter 2, LHC operated on 2012 at centre-of-mass energy $\sqrt{s}$=8 TeV. The integrated luminosity suitable for physics was L = 20.3fb^{-1}and the maximum peak instantaneous luminosity was $7.73 \times 10^{33}\mathrm{cm}^{-2}\mathrm{s}^{-1}$.

Figure 3.6 shows the luminosity versus time for the 2012 run, where the luminosities delivered from LHC, recorded by ATLAS and suitable for Physics are overlaid:

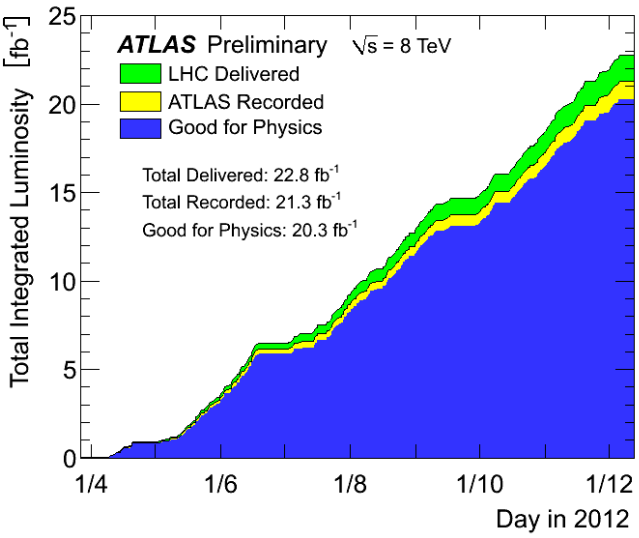

Figure 3.6: Cumulative luminosity versus time delivered (green), recorded by ATLAS (yellow), and certified to be good quality data (blue) during stable beams and for pp collisions at 8 TeV centre-of-mass energy in 2012. Figure from [45]

The collected raw data were subjected to quality control checks in order to ensure that all the accelerator and detector apparatuses were operating in stable mode. Therefore, the data series (luminosity blocks) where any kind of malfunction was recorded have been removed. The ATLAS Data Quality system creates the so-called "Good Runs List", which is the first condition applied on the analysis of the collision data.

3.6 Simulation

The simulation of physics interactions is essential for the detector operation, since it provides information about the expected behaviour of the detector systems and the expected physics outcomes.

The ATLAS simulation process is executed in three steps:

1. Event Generation and decays
2. Simulation of the detector layout and the physics interactions
3. Digitisation of simulated energy deposits to electric signal for direct comparison with read-out system of ATLAS

At generation level the interaction to be examined is kept only after the generated p-p collision. For cases where there is a particular region of interest in the interaction's phase-space, generation cuts are applied. Subsequently, based on the configuration of the Monte-Carlo generator, the particles decay up to the final stable state. The information of the generated events is transferred to the simulated files. A full representation of the ATLAS simulation procedure is shown in Figure 3.7.

Every generated particle is propagated inside the detector. ATLAS has been modelled with the GEANT4 package [65] and configured with particular geometries and material descriptions. The simulated particles interactions and energy depositions create the "hits" collection. The information from this collection is digitised, accessed and stored with the same interface as real data.

The information from the generated events and the detector simulation, comprise the "truth" collection in any MC simulation of ATLAS. The values of the "truth" collection are used for direct comparisons and correction between the observed data and the theoretical expectations.

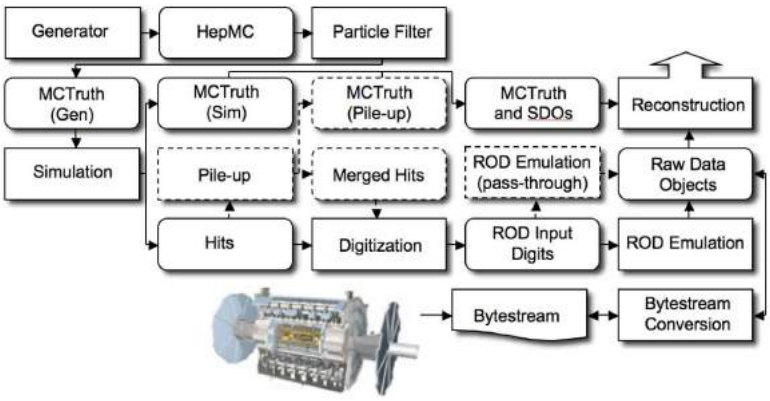

Figure 3.7: The flow of ATLAS simulation software, from event generators (top left) through reconstruction (top right) Figure from [66]

3.7 Experimental uncertainties in reconstruction

The reconstruction of physics objects contains experimental uncertainties. These are associated with: detector defects, reconstruction algorithms, triggering criteria and luminosity. This section presents a list of the main experimental uncertainties for electrons, muons and jets, which are the physics objects involved in the studies of this thesis. The inclusion of the following systematic uncertainties has been recommended by the corresponding Combined Performance groups of ATLAS. For the analyses presented in this thesis, the systematic uncertainties are treated similar to the $H \to ZZ^{(*)} \to 4l$ main analysis [67].

3.7.1 Electrons

- **Electron energy scale.**
  The term refers to all the MC-based calibration of the calorimeter derived from $Z \to e^+e^-$ decays, as well as any MC related uncertainty regarding the material description at the calorimeter.

- **Electron momentum smearing.**
  In MC level, the momentum of the electrons should be smeared by a small factor to incorporate the uncertainty of the measurement on data. The factors are derived from differences on data and MC between the electrons energy which originate from Z boson decays and the mismodelling of the calorimeter material description on the MC.

- **Electron reconstruction and identification.**
  The term refers to differences observed in the reconstruction and identification efficiencies between data and MC. From these differences, scale factors are extracted and applied at the MC. The systematic uncertainties are given by varying the scale factor within their uncertainties.
  Particularly for electron identification, the scale factors are determined from W/Z boson decays and they are dependent on the pseudorapidity, the E_{T} and the electron reconstruction algorithm used.

- **Electron isolation.**
  The uncertainty originates from the difference between data and MC about the description of the isolation shapes of the electrons. The difference produces scale factors which are employed to add extra weights on the MC and they are $|\eta|$ and p_{T} dependent. The total systematic uncertainty is expressed by the variation of the scale factor within their uncertainty.

3.7.2 Muons

- **Muon reconstruction and identification.**
  The term refers to the efficiency of the muon reconstruction algorithm. This is achieved by utilising the "tag and probe" method on J/ψ and Z decays. A fully reconstructed muon (tag) pairs with an inner detector track (probe) to form a di-muon pair.The efficiency is extracted by measuring if the probe can be detected at the Muon Spectrometer. The ratio of efficiencies between data and MC creates the reconstruction efficiency scale factor which is applied in the muon selection. The scale factors are varied within their uncertainties from the nominal value and the differences yield the total systematic uncertainty.

- **Muon resolution.**
  This uncertainty refers to the muon resolution uncertainties from the inner detector and the muon spectrometer. The momentum resolution parameter factor is determined in different η regions of the detector using a template fit to $Z \rightarrow \mu^+\mu^-$ events. The total uncertainty is derived by varying the factors within their uncertainties compared to the nominal value.

- **Muon scale.**
  The terms refers to uncertainties due to scale dependence at momentum measured in the Muon Spectrometer between data and MC. The dependence is due to the behaviour of the muons as Minimum Ionising Particles (MIPs) inside the EM calorimeter. The muon momentum resolution is calibrated from a template fit and the extra factor is added in order to account for differences between data and MC. Similarly, the total uncertainty is obtained from the variations of the factor from the nominal value.

3.7.3 Jets

- **Jets energy scale and resolution.**
  The uncertainties in jet energy and resolution originate mainly from the uncertainty on the correction from the electromagnetic to hadronic scale. The correction has variations which are conditional to the p_{T} and $|\eta|$ of the jet. Additional uncertainties are included, related to the jet modelling, the amount of overlapping collisions, the calibration techniques, the flavour composition and the parton-dependent response of jets.

3.7.4 Trigger and luminosity

- **Trigger requirement**
  The final state of the analysis applies energy cuts on the leptons. Retrospectively, it is ensured that one of these high p_{T} leptons would have triggered the detector systems.

However, an uncertainty check is performed by removing the trigger requirement from the event selection.

- **Luminosity uncertainty**
  Based on the 20.3fb^{-1} integrated luminosity which was recorded by ATLAS for physics processes on the 8 TeV data, the overall uncertainty is 2.8%. The uncertainty acts as normalisation uncertainty in the shape of the observables.

Chapter 4

Muon reconstruction efficiency in the forward region of the ATLAS Muon Spectrometer

4.1 Introduction

The reconstruction efficiency of the ATLAS Muon Spectrometer is the topic of the present chapter.

For this work, conducted by the Muon Combined Performance group of ATLAS, the author contributed by extracting the reconstruction efficiency for the pseudorapidity region 2.5 < $|\eta|$ <2.7 (high-$|\eta|$) comparing simulation with data. The results are used by the ATLAS collaboration to apply correction factors to muons.

The reconstruction efficiency result was published in the 2014 ATLAS Muon Performance paper [59] and was presented on behalf of the ATLAS collaboration at the International Conference of High Energy Physics in 2014 [68]. Additionally, the present work was the service task for my qualification as an ATLAS author.

4.2 Muon reconstruction efficiency

The term efficiency in muon reconstruction refers to the ratio of the detected muons over the total amount of "truth" muons in a fiducial volume. The efficiency ratio between data and MC creates the reconstruction scale factor (SF) which is applied for correction on the MC, in order to account for the reconstruction differences with the data. For muon performance studies, the $Z \rightarrow \mu^+\mu^-$ decays are used since the process has been extensively studied in the past and the theoretical description of the process is well known.

For muons, the reconstruction efficiency scale factors are provided with respect to the p_{T} and $|\eta|$ of the muon. Spatially, the only limitation is the total acceptance of the Muon Spectrometer which is up to $|\eta| = 2.7$. Different methods are applied to region until $|\eta| < 2.5$ ("central region") and to the high-$|\eta|$ region.

4.3 Tag and probe method

The muon reconstruction efficiency depends on the efficiency of the Inner Detector and the Muon Spectrometer separately, and the matching efficiency between them. Measuring the individual efficiencies, it is possible to obtain a picture about the full reconstruction efficiency. The method which is utilised for the efficiency calculation is the so-called "tag and probe" method. In this process, $Z \rightarrow \mu^{+}\mu^{-}$ decays are selected where two oppositely charged muon tracks are required. The tracks should be isolated with di-muon invariant mass near to the Z boson peak.

One of the tracks, should be a well-reconstructed Combined muon, called "tag". Depending on the efficiency of the muon system under study, a particular track is chosen for the other muon, the "probe".

If the Inner Detector efficiency is to be measured, the "probe" should be a standalone muon with hits only on the Muon Spectrometer. Therefore, the Inner Detector efficiency is defined as the fraction of standalone probes which can be associated to an Inner Detector track.

Likewise, if the Muon Spectrometer efficiency is to be measured, the "probe" should be an Inner Detector muon track. The Muon Spectrometer efficiency is defined as the fraction of Inner Detector track probes which can be associated to either Combined or Segment-Tagged muon.

4.4 Reconstruction efficiency in the high pseudorapidity region

The high pseudorapidity region lies at the boundaries of the Muon Spectrometer acceptance where there is no track information from the Inner Detector. The full use of spectrometer's acceptance until $|\eta| = 2.7$ could increase the acceptance of various physics analyses. Therefore, the reconstruction efficiency of muons in this area should be studied. The high-$|\eta|$ region with the corresponding Muon Spectrometer is shown in Figure 4.1

4.4.1 Scale Factor extraction method

The use of the standard tag-and-probe method to calculate the reconstruction efficiency scale factors is not applicable in the high-$|\eta|$ region, due to the absence of track information which

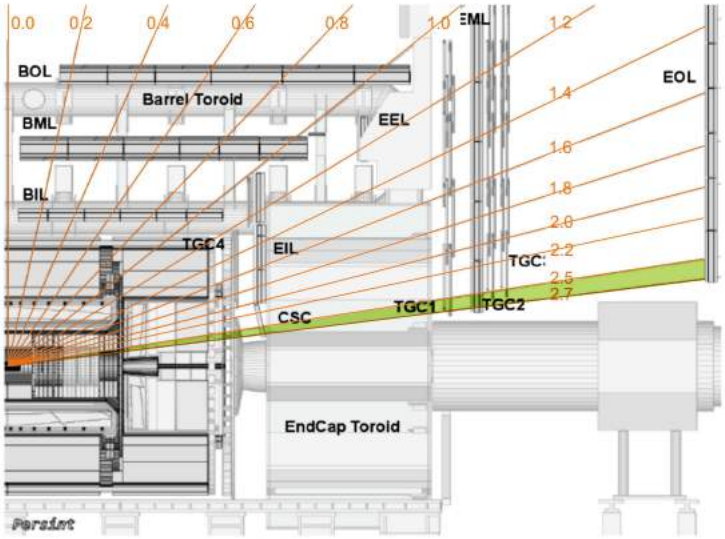

Figure 4.1: Cut-view of the ATLAS Muon Spectrometer with the corresponding pseudorapidity region. Highlighted with green is the high-$|\eta|$ region.

could be assigned to a probe muon. However, the calculation can be achieved by comparing the efficiency calculated in the high-$|\eta|$ region to a well known and modelled area, at the boundaries of the central region. The motivation behind this approach is the assumption that muons behave similarly in close neighbouring regions and thus it is safe to extrapolate the behaviour between them.

The analysis method comprises a "tag and probe"-like method for $Z \rightarrow \mu^+\mu^-$ candidates. The search is performed in two regions of interest, namely the high-$|\eta|$ and the "control" (2.2< $|\eta|$ <2.5) regions. The "tag" muon is always a Combined muon (CB) which satisfies strict quality cuts and exists always below the lower $|\eta|$ threshold of the regions, $|\eta| < 2.5$ and $|\eta| < 2.2$ respectively. The other muon is the "probe" with loose quality cuts, but always lying within the regions of interest.

The scale factor is calculated from a double ratio, shown in Eq.4.1, where the numerator is the ratio of $Z \rightarrow \mu^+\mu^-$ candidates at data over MC, with a probe muon in the high-$|\eta|$ region, and the denominator the same ratio with the only difference that the probe is in the control region.

$$\mathrm{SF} = \frac{\frac{N^{\mathrm{DATA}}}{N^{\mathrm{MC}}}\Big\} 2.5 < |\eta| < 2.7}{\frac{N^{\mathrm{DATA}}}{N^{\mathrm{MC}}}\Big\} 2.2 < |\eta| < 2.5} \tag{4.1}$$

The calculated scale factors are grouped afterwards in 6 bins, depending on the p_{T} of the probe muon. The p_{T} bins are: $[10, 20), [20, 30).[30, 40), [40, 50), [50, 60), [60 < 120]$ GeV . The results are extracted for each of the 3 muon reconstruction algorithms (Chains) as described in

Chapter 3.

4.4.2 "Tag and probe" selection

The selection of the tag and probe pairs took place on a $Z \rightarrow \mu^+\mu^-$ MC sample produced with the POWHEG generator [69] and from the 8 TeV data selected by ATLAS with detector runs suitable for physics analyses (Good Run List). The selection criteria are similar for both data and MC. Initially, single muon high-p_{T} triggers are used, which contain an isolated muon trigger with p_{T} thresholds of 24 GeV or 36 GeV. For the exclusion of non-collision background, the events are required to have at least one primary vertex reconstructed with at least three tracks and a longitudinal impact parameter z_0 less than 200mm. Lastly, since the analysis is based on $Z \rightarrow \mu^+\mu^-$ decays, events with less than two muon objects are rejected. A summary of the event selection requirements is shown on Table 4.1.

Table 4.1: Summary of event selection requirements.

Event selection criteria	
Data quality	Good Run List (Data only)
Trigger	EF_mu24i_tight OR EF_mu36_tight
N^{PV}_{track}	> 3 tracks
$\lvert z_{PV}\rvert$	$< 200mm$
N_muons	> 2 muons

After the event selection, the next step is the formation of the tag and probe pairs. Firstly, the tag muons should belong to the Combined muons (CB) category. Strict quality criteria are applied based on the information from the Inner Detector tracks. The quality criteria for the muon tracks were given as guideline from the Muon Combined Performance group of ATLAS for analyses using muons on 2012 data [59]. The sum of the pixel hits and the crossed dead pixel sensors should be greater than 0. The sum of the semiconductor tracker (SCT) hits and the crossed dead SCT sensors to be greater than 4. Also, the number of empty space (holes) in the pixel detector and the SCT should be less than 3.

Additionally, for tag muons which are in the acceptance of the transition radiation tracker (TRT) (0.1<$|\eta|$ <1.9), more than 5 TRT hits are required and less than 90% of the TRT hits to have been classified as outliers, if there was an unsuccessful extension of the track to the TRT.

Regarding the kinematic properties, the tag muon is required to have p_{T} > 25GeV and to be $|\eta|$ either < 2.5, for the high-$|\eta|$, or <2.2 , for the control region respectively. Also, the z_0 longidutinal impact parameter should be less than 10mm.

To verify the quality of the muon track and to ensure the high p_{T}, the tag candidate should be the same object that triggered the event during the online reconstruction, processed by the either L1 or L2 trigger.

Lastly, a track isolation requirement is applied, asking the ratio of the p_{T} of a cone with opening ΔR =0.2 from the muon track over the muon p_{T}, to be less than 10%, minimising

therefore the presence of nearby objects. In case where more than 1 muons pass the tag requirements, the one with the highest p_T is kept.

Subsequently, the selection of the probe muon takes place. The probe can be classified either as Combined or as Stand Alone (SA). In addition, the probe is searched at either the high-$|\eta|$ ($2.5 < |\eta| < 2.7$) or at the control ($2.2 < |\eta| < 2.5$) region with at least one hit at the Cathode Strip Chamber (CSC) and the Monitored Drift Tube (MDT). A relaxed p_T requirement follows, with $p_T > 10$ GeV.

Finally, calorimeter isolation is required for the probe with transverse energy E_T around a cone of ΔR =0.2 from the muon over the muon p_T to be less than 10%. Similarly to the tag selection, the probe with the highest p_T is selected if more than one muon passes the criteria.

After successful selection of the tag and probe pair, further cuts are applied to the di-muon system. In order to ensure that the two muons come from a Z boson decay, their charge has to be opposite and to have an angular separation in the $\eta - \phi$ plane (ΔR) greater than 0.2. The final requiremenent is for the di-muon mass to be in a range of 10 GeV within the known Z boson mass quoted by the Particle Data Group[17].

All the selection criteria for tag and probe, are summarised on Table 4.2. Kinematic distributions of the selected tag and probe pairs are shown in Figures 4.2, 4.3 and 4.4. However, due to mis-modelling of the simulation for this boundary high-η region at of the Muon Spectrometer, there are some difference in the distributions between data and simulation.

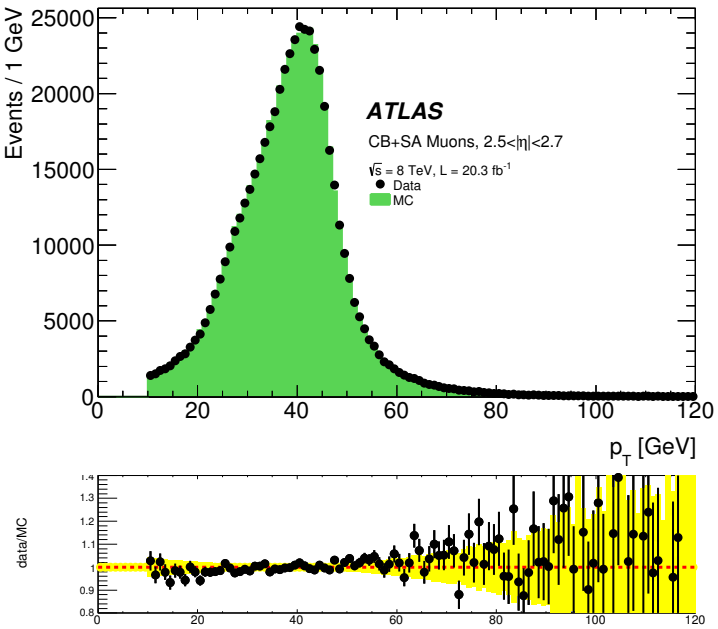

Figure 4.2: Distribution of the p_T for the probe muons which pass the selection criteria and exist in the high-$|\eta|$ region. In the bottom ratio plot, reasonable agreement between data and MC is observed,considering the mis-modelling of the MC for high-η, with the yellow band indicating the statistical uncertainty.

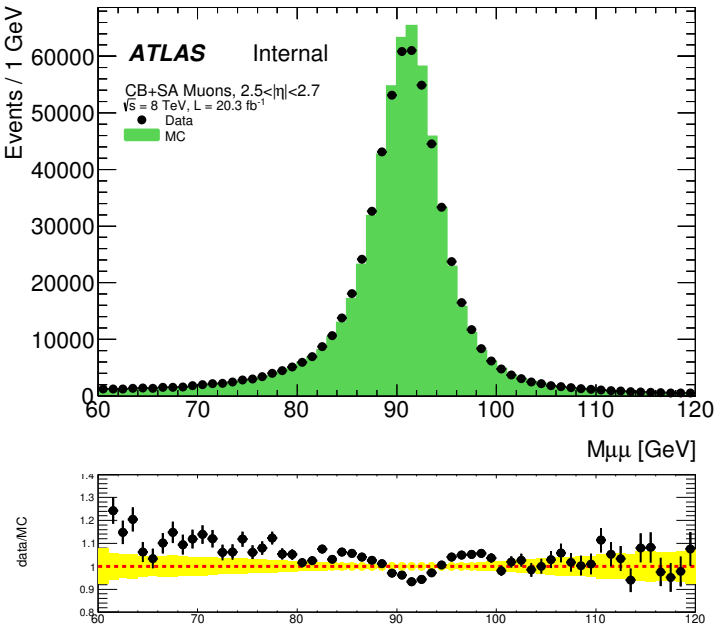

Figure 4.3: Distribution of the invariant mass of the di-muon pair with the probe muon in the high-$|\eta|$ region and the tag muon in $|\eta| < 2.5$. In the bottom ratio plot, reasonable agreement between data and MC is observed, considering the mis-modelling of the MC for high-η, with the yellow band indicating the statistical uncertainty.

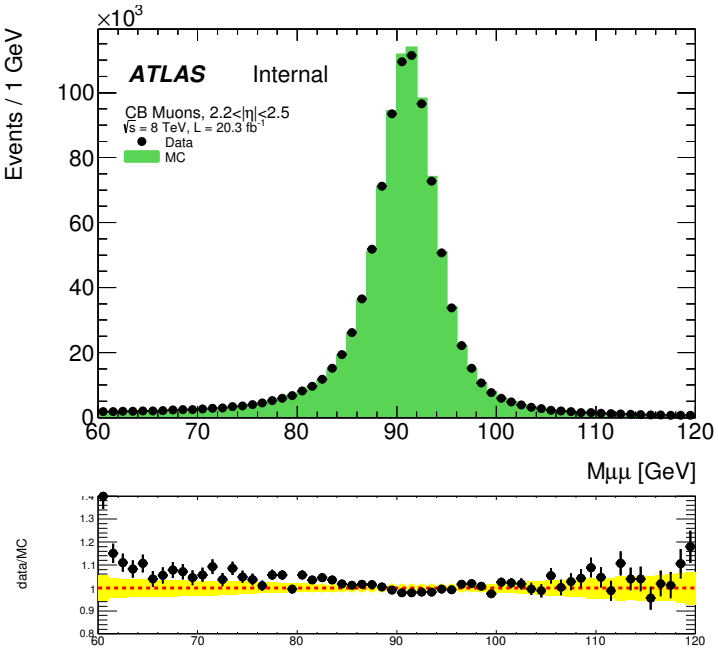

Figure 4.4: Distribution of the invariant mass of the di-muon pair with the probe muon in the control region and the tag muon in $|\eta| < 2.2$. In the bottom ratio plot, reasonable agreement between data and MC is observed, considering the mis-modelling of the MC for high-η, with the yellow band indicating the statistical uncertainty.

Table 4.2: Tag and probe muon selection criteria. Note that η^a corresponds to the η requirement of the numerator of equation 4.1 while η^b corresponds to the denominator as described in the text.

Tag Selection cuts	
Category	Combined
Quality	N_pixel hits + N_crossed dead pixel sensors > 0 N_SCT hits + N_crossed dead SCT sensors> 4 N_pixel holes + N_SCT holes < 3. (if $0.1 < \|\eta\| < 1.9$): $N_{TRT} > 5$ and $N_{TRT\_outliers} < 0.9 \times N_{TRT}$.
p_T	> 25 GeV
$\|\eta^a\|$	< 2.5
$\|\eta^b\|$	< 2.2
z_0	< 10 mm
Trigger matched muon	
Track isolation	$p_T{}^{cone20}/p_T < 0.1$
Probe Selection cuts	
Category	Combined / Stand Alone
$\|\eta^a\|$	2.5 – 2.7
$\|\eta^b\|$	2.2 – 2.5
p_T	> 10 GeV
Calorimeter isolation	$E_T^{cone20}/p_T < 0.1$
ΔR(Tag,Probe)	> 0.2
Muons with opposite charge Di-muon mass	$\|M_Z^{PDG} - M_{\mu\mu}\| < 10GeV$

4.4.3 Systematic uncertainties

There are various sources of systematic uncertainties which affect the analysis. A comprehensive description is given below:

- **Kinematic and isolation properties:**

  The properties of the tag and probe pairs with their relative variations are the systematic uncertainties with the highest effect on the result. These are addressed by varying the p_T of the tag muon from 25 GeV to 27 GeV , and the track isolation requirement from 10% to 12%. The p_T variation had a less then 0.4% effect whereas the track isolation contributed to a level of less than 0.1%. Furthermore, the calorimeter isolation is removed in order to study the sensitivity effect in high $|\eta|$ regions. Overall, the removal of calorimeter isolation had a less than 0.7% effect.

- **Di-muon mass:**

In order to account for resolution effects, the di-muon mass is allowed to lie in a window of 12 GeV from the Z mass. The impact of widening the di-muon mass range by 2 GeV was less than 0.2%.

- **Theory:**

The baseline Parton Distribution Function (PDF) for the $Z \to \mu^+\mu^-$ MC POWHEG sample was the MSTW2008NLO [46]. Two studies were performed regarding the PDF. Firstly, the effect of the 40 different subsets which comprise the PDF, compared to the central PDF value, was studied at truth-level. For each subset, a new $Z \to \mu^+\mu^-$ MC sample was recreated and the kinematic cuts were applied to the muons. The ratio of number of born-level muons in the central region to the number of muons in the control region was extracted and compared with the nominal values. The overall uncertainty is calculated as the average of the difference from the subsets with respect to the nominal. The effect was found to contribute to the scale factors at a level of less than 0.5%.

The second PDF-related uncertainty was the comparison with other PDF sets. For this study, the PDF CT10[70] was used and the effect was studied by re-weighting the MSTW PDF to match the values of CT10 at a new $Z \to \mu^+\mu^-$ POWHEG MC sample. The re-weighting of the PDF introduced an overall uncertainty of 0.2%.

- **Background:**

The only source of background process for this study originates mainly from QCD heavy flavour $b\bar{b}$ decays to muons. The background contribution was studied and was found negligible (~0.05%), affecting only the first bin of the scale factor. The reason for this small effect is due to the $p_{\mathrm{T}} > 10$ GeV requirement for probe muons, where background processes from heavy quarks are unlikely to contribute.

The full list of the systematic uncertainties, splitted for each muon reconstruction algorithm, is shown on the Tables 4.3, 4.4 and 4.5.

Table 4.3: Fractional difference between the variation of each source of systematic uncertainty and the nominal SF values for Chain 1. Wherever one value exists for a systematic source it is implied that is the same for all bins.

	$\lvert SF_{Nominal} - SF_{syst}\rvert / SF_{Nominal}$					
Bin (GeV)	Tag pt	Pair Mass	Tag Iso	Probe Calo Iso	PDF subset	PDF rw
10-20	0.4	0.0	0.0	0.7		
20-30	0.0	0.2	0.0	0.0		
30-40	0.0	0.0	0.0	0.1		
40-50	0.0	0.0	0.0	0.0	< 0.5	0.2
50-60	0.2	0.2	0.1	0.0		
> 60	0.4	0.1	0.0	0.2		

In order to obtain the total systematic uncertainty in the scale factors, the contribution from each aforementioned source, apart from the background contribution, is squared and

Table 4.4: Fractional difference between the variation of each source of systematic uncertainty and the nominal SF values for Chain 2. Wherever one value exists for a systematic source it is implied that is the same for all bins.

	$\|SF_{Nominal} - SF_{syst}\|/SF_{Nominal}$					
Bin (GeV)	Tag pt	Pair Mass	Tag Iso	Probe Calo Iso	PDF subset	PDF rw
10-20	0.7	0.5	0.1	0.9		
20-30	0.3	0.1	0.0	0.6		
30-40	0.0	0.0	0.0	0.1		
40-50	0.0	0.1	0.0	0.1	< 0.5	0.3
50-60	0.1	0.0	0.1	0.4		
> 60	0.5	0.1	0.1	0.4		

Table 4.5: Fractional difference between the variation of each source of systematic uncertainty and the nominal SF values for Chain 3. Wherever one value exists for a systematic source it is implied that is the same for all bins.

	$\|SF_{Nominal} - SF_{syst}\|/SF_{Nominal}$					
Bin (GeV)	Tag pt	Pair Mass	Tag Iso	Probe Calo Iso	PDF subset	PDF rw
10-20	1.0	0.2	0.1	1.0		
20-30	0.2	0.0	0.0	0.0		
30-40	0.0	0.1	0.0	0.0		
40-50	0.0	0.1	0.0	0.0	< 0.5	0.3
50-60	0.0	0.1	0.0	0.1		
> 60	0.4	0.0	0.0	0.2		

added altogether, obtaining as final result the square root of the sum (quadrature method). All the sources of systematic uncertainties are considered to be uncorrelated to each other. Since the final result is based on counting and not on any shape of a variable, then the systematic uncertainties are independent, each having a separate contribution without being affected by other uncertainties.

4.4.4 Scale Factor Results

With the application of Eq.4.1 and the inclusion of the systematic and statistical uncertainties, the reconstruction efficiency scale factors are extracted, grouped in p_{T} bins, for each of the 3 muon reconstruction chains. The results are shown in Tables 4.6 and 4.7 and illustrated in Figures 4.5 and 4.6.

4.4.5 Reconstruction Efficiency

The final component of the study is to extract the data reconstruction efficiency for the muons in the high-$|\eta|$ region. The MC efficiency is corrected using the reconstruction scale factors in order to obtain the efficiency on data. The efficiency results are presented only for the Chain-1 reconstruction algorithm, known as "STACO".

Table 4.6: Reconstruction efficiency SF of high-η muons reconstructed with the Chain 1 and Chain 2 algorithm.

Chain 1 - STACO				Chain 2 - MUID			
Bin (GeV)	Scale Factor	Stat.	Syst	Bin (GeV)	Scale Factor	Stat.	Syst
10-20	0.971	0.011	0.010	10-20	0.959	0.015	0.011
20-30	0.979	0.006	0.006	20-30	0.982	0.006	0.008
30-40	0.985	0.004	0.006	30-40	0.989	0.006	0.006
40-50	0.989	0.004	0.005	40-50	0.983	0.006	0.006
50-60	1.003	0.009	0.007	50-120	0.995	0.008	0.007
>60	0.998	0.014	0.007	> 60	0.958	0.015	0.008

Table 4.7: Reconstruction efficiency SF of high-η muons reconstructed with the Chain 3(MUON) algorithm.

Chain 3 - MUON			
Bin (GeV)	Scale Factor	Stat.	Syst
10-20	0.965	0.010	0.015
20-30	0.989	0.006	0.006
30-40	0.991	0.004	0.006
40-50	0.989	0.004	0.006
50-60	1.010	0.009	0.007
> 60	0.964	0.014	0.007

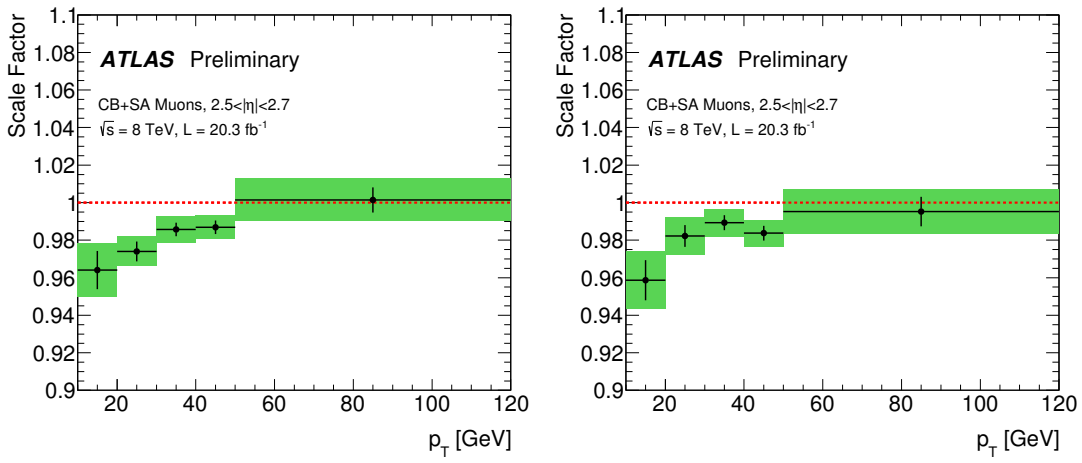

(a) Chain 1 - STACO

(b) Chain 2 - MUID

Figure 4.5: Reconstruction efficiency scale factors for the (a) Chain 1 and (b) Chain 2 reconstruction algorithms.

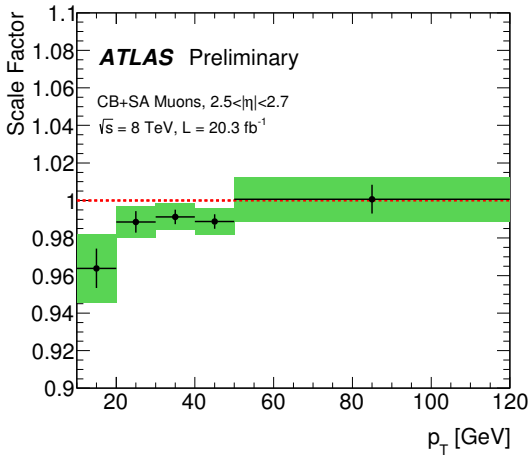

(a) Chain 3 - MUON

Figure 4.6: Reconstruction efficiency scale factors for the Chain 3 reconstruction algorithm.

The efficiency result is based on the equation:

$$\text{Data\_eff} = \text{SF} \times \text{MC\_eff} \tag{4.2}$$

where MC_eff:

$$\text{MC\_eff} = \frac{\text{True muons, passed fid. cuts and reco matched}}{\text{True muon tracks, passed fid. cuts}} \tag{4.3}$$

4.4.5.1 MC efficiency

In detector performance studies, the efficiency corresponds to the ratio of the MC truth muons which pass some fiducial cuts and are matched with a reconstructed object, over all the MC truth muons that pass the same fiducial cuts.

The calculation of the MC efficiency is performed in a $Z \rightarrow \mu^+\mu^-$ POWHEG sample. The analysis looks for truth muons with $p_T > 10$ GeV and pseudorapidity $2.5 < |\eta| < 2.7$ which have an angular separation (dR) less than 0.2 with the reconstructed muon of the event. The efficiency is grouped based on the p_T of the probe muon, similar to the scale factors. However, to minimise the statistical uncertainty of the scale factors, the last two p_T bins $(50-60)\&(60<)$ GeV are merged into a single one.

The calculated MC efficiency is presented on Table. 4.8

After multiplication with the scale factors from Table 4.6, the data reconstruction efficiency following results are obtained, shown on Table 4.9.

Table 4.8: MC efficiencies for the high-η muons, grouped on p_T bins

p_T Bin GeV	MC efficiency
10-20	0.9531 ± 0.0008
20-30	0.9795 ± 0.0004
10-40	0.9794 ± 0.0003
40-50	0.9795 ± 0.0003
> 50	0.9722 ± 0.0005

Table 4.9: Data reconstruction efficiencies for the high-η muons, grouped on p_T bins

Bin GeV	Data Reconstruction efficiency
10-20	0.926 ± 0.010
20-30	0.959 ± 0.005
10-40	0.965 ± 0.004
40-50	0.967 ± 0.004
> 50	0.979 ± 0.011

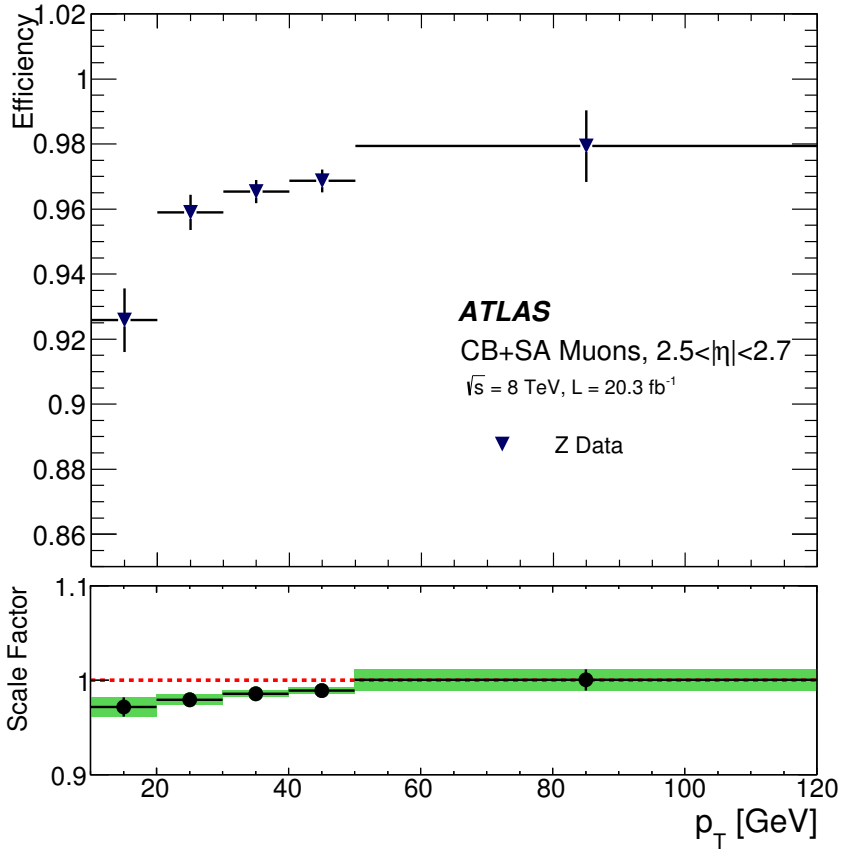

Figure 4.7: Data reconstruction efficiency for high-$|\eta|$ muons, reconstructed with the Chain 1 algorithm. Figure from [59]

4.5 Conclusion

The results presented in this study show the high levels of reconstruction efficiency of the ATLAS Muon Spectrometer. The method used a conservative approach which was to assume similar behaviour in neighbouring areas of the spectrometer, namely the control region ($2.2 < \eta < 2.5$) and the high-eta region ($2.5 < \eta < 2.7$). Using the "tag-and-probe" method which ensures the presence of one well-reconstructed central muon, the behaviour of the other muon in between the aforementioned areas, was used as level of comparison and extrapolation from the control to the high-eta region.

At the boundary region of high pseudorapidity ($\eta < 2.7$) where the spectrometer instrumention can be found, the reconstruction efficiency is more than 92% low p_{T} muons reaching up to more than 97% for higher p_{T}. The excellent performance in these extreme areas of the ATLAS Muon Spectrometer can be observed, offering the to physics analyses who use muons, to expand their phase-space using high-eta muons, where the calculated scale-factors have been applied for corrections.

Chapter 5

Reconstruction of non-collinear QED Final State Radiation in $Z \to \ell\ell$ events

In this chapter, the reconstruction of non-collinear QED Final State Radiation (FSR) in $Z \to \ell\ell$ ($\ell = e, \mu$) events is detailed. The FSR reconstruction and identification method, with the improvements in the Z boson invariant mass reconstruction are presented. The impact of the method in $H \to ZZ^{(*)} \to 4l$ channel is demonstrated, where a better accuracy on the Higgs boson mass measurement is achieved.

The author made FSR performance studies in $Z \to \mu^+\mu^-$ and $Z \to e^+e^-$ events, and studied the effect of the FSR correction at the $H \to ZZ^{(*)} \to 4l$ mass measurement on the ATLAS Run-I dataset [67].

5.1 Introduction

The QED Final State Radiation is the phenomenon where a photon (γ) is emitted from a lepton (e, μ) which had originated from a Z or W boson. The consequence of this emission, when the photon carries a large fraction of the boson momentum, is that there will be a shift in the lepton-pair invariant mass [71]. In this particular chapter, only decays from Z boson are considered.

A good accuracy of the Z boson mass resolution is essential, given the importance of the Z boson in electroweak studies. Furthermore, every search for particles decaying to leptons should take this effect into account in order to improve their measurements. One of the applications,considered in the thesis, of the FSR inclusion is for the measurement of the $H \to ZZ^{(*)} \to 4l$ final state, and the measurement of the Higgs mass in this channel. Consid-

ering the presence of FSR, the tails at the distribution of the Higgs invariant mass are reduced improving the mass resolution.

5.2 Reconstruction and Identification

Leptons could emit FSR photons at any angle. However, the relative angle between the lepton and the photon is smaller than the opening angle of the dilepton system. If the photon is emitted in larger angles, it can not determine the charge of the individual lepton. Only the total zero charge of the system would be perceivable, implying no emission[1] [72]. The energy of the emitted photon varies. From a small amount of energy to a significant level of the lepton energy, reaching the regime of GeV.

In ATLAS, the FSR photons interact with the LAr Electromagnetic Calorimeter, creating an energy cluster and having their energy reconstructed with the standard ATLAS algorithms.

The relative angle between the lepton track and the energy cluster created by the FSR is the discriminant in order to classify the FSR. If the angular separation in the $\eta - \phi$ plane between the lepton track and the photon cluster is less than 0.15, the FSR is classified as **collinear**. If the angular separation is greater than 0.15, the FSR is classified as **non-collinear**, hereafter **far**. The majority of the FSR signal is mostly collinear and more than 10% of the photon energy is absorbed in the first layer of the calorimeter as shown in Figure 5.1.

The background contribution in the FSR reconstruction originates from many sources. One potential source could be the muon energy loss in the LAr Calorimeter ("μ" background). Also, QCD jets faking electrons and the decays of neutral mesons to photons, like $\pi^0 \to \gamma\gamma$ are background sources. An additional background component could be a process like $Z \to \tau^+\tau^-$ and $W \to \mu^\pm\nu$ where the decay products could fake FSR photons.

As muons transverse the calorimeter, they behave as minimum ionising particles and thus it is possible to have deposition of energy in the same cluster with the FSR photon energy cluster.

5.2.1 Selection

This chapter focuses mainly on the far FSR reconstruction and selection. However, the search for a far FSR photon is related to the presence of a collinear photon. Therefore, both selection mechanisms will be briefly described.

Collinear FSR: The search for collinear FSR is performed only in di-muon pairs. In case of di-electron pairs, the collinear FSR will be in the same energy cluster as the electron and they will be reconstructed together. The selection is divided into two groups based on the transverse energy deposited at the calorimeter (E_T) and targets to minimise the background contribution.

[1] Details on the emission mechanism can be found on Ellis, R. K., W. J. Stirling, and B. R. Webber. QCD and Collider Physics. 1st ed. Cambridge: Cambridge University Press, 1996. pp. 180-181

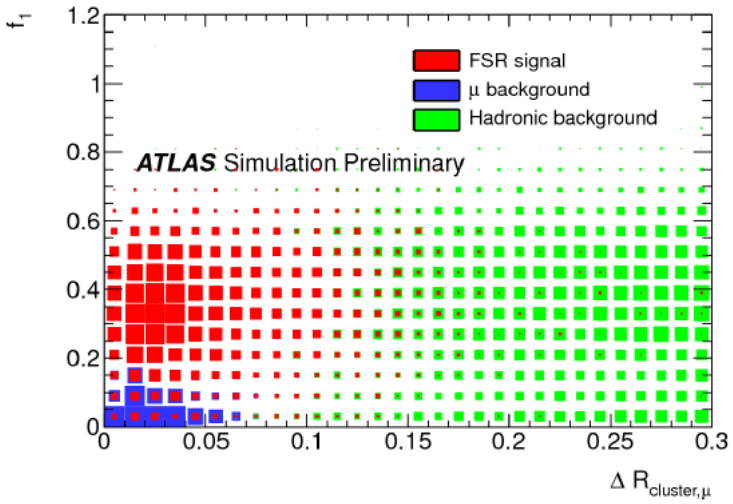

Figure 5.1: Correlation plots of discriminants f1, which is the ratio of the photon energy absorbed in the first layer of the calorimeter over total, and ΔR (cluster, μ) with E_T (EM cluster) > 1.3 GeV. Figure from [73]

For energy clusters with $E_{\mathrm{T}} \gtrsim 3.5$ GeV the standard ATLAS photon and electron cluster reconstruction is used. In this category, the angular separation between the muon track and the FSR photon should be less than 0.15 ($\Delta R(\mu, \gamma) < 0.15$). Also, the FSR photon is required to have deposited more than 10% of its total energy in the first layer of the calorimeter as the photon interacts with the medium and the electromagnetic shower starts, in order to discriminate against minimum ionising muons where the muon energy from the Landau distribution tail is still significant, up to 3 GeV.

For energy clusters with $E_{\mathrm{T}} < 3.5$ GeV the reconstruction utilises topological seeded clusters, similar for jets reconstruction as described in Chapter 3. The angular separation between the muon track and the FSR photon is required to be < 0.08 and the FSR photon should have deposited more than 20% of the total energy in the first layer. An additional correction, in order to account for the muon ionisation where the muon deposits energy in the same cluster with the FSR takes place. It requires for a subtraction of 400 MeV from the energy cluster if the separation between the muon and the FSR photon is less than 0.05. This substraction accounts for the average muon energy deposition in the calorimeter [67].

Regarding the position of the FSR photons in the calorimeter, the crack region of (1.37<$|\eta|$ <1.52) is excluded together with the forward region ($|\eta|$ >2.5). If more than one candidates are found, only the one with the highest energy cluster is kept.

Far FSR: The search for far FSR photons takes place in both di-muon and di-electron pairs. Given the large separation between the lepton and the photon ($\Delta R > 0.15$), it is likely that other sources could fake a far FSR photon. Thus, strict quality and energy selection criterias are applied for the selection of the far FSR. Initially, the photon candidate is required to pass

the *tight* photon identification criteria. In addition, the photon is required to have transverse cluster energy E_T greater than 10 GeV. An extra isolation cut is applied, by requiring the sum of the transverse energy of a cone with $\Delta R < 0.4$ around the photon cluster to be less than 4 GeV . .

A summary of the FSR selection is presented in Table 5.1.

Table 5.1: Summary of FSR selection

	Collinear		Far
Leptons	μ		μ,e
Photon E_T (GeV)	> 3.5	< 3.5	> 10
ΔR(l,γ)	< 0.15	< 0.08	> 0.15
		$< 0.05 \to (E_T - 0.4)$	
Pseudorapidity	$\neq(1.37 < \lvert\eta\rvert < 1.52)$ $(\lvert\eta\rvert < 2.5)$		

5.3 Effect in $Z \to \ell\ell$ events

In order to study the effect of FSR in the $Z \to \ell\ell$ events, an analysis was performed on data and on MC samples where the behaviour of the FSR inclusion was studied.

5.3.1 Data and MC samples

The FSR study on the $Z \to \ell\ell$ channel included all the 2012 ATLAS data which were available for physics analysis. The MC samples which were used ($Z \to \mu^+\mu^-$ and $Z \to e^+e^-$) were generated with the ALPGEN[74] MC generator using the CTEQ6L1 PDF set[75] and α_S at Leading Order (LO), with the inclusion of up to five extra partons included as hard scatters to account for background effects, like additional hadronic background. The MC samples were interfaced with PYTHIA[76] using the Perugia2011C tune [77] for hadronisation and showering effects. The MC generator PHOTOS[78] was used for the inclusion of QED radiative corrections. In order to fully simulate the average interaction per bunch crossing, the MC samples are combined together and weighting is applied to each of them. Finally, the ATLAS detector material and geometry has been modelled with GEANT4[65].

5.3.2 Event selection

The selection looks for two oppositely charged same flavour leptons (e,μ) which originate from a Z boson decay. The event selection is similar to the $H \to ZZ^{(*)} \to 4l$ analysis when a dilepton pair is formed [67], with tighter lepton criteria. It is the baseline Z boson selection before looking for FSR photons.

The initial requirement is that the events were triggered from a single muon or electron high p_T triggers. For the muons trigger, the trigger selection comprises an isolated muon

which passes the tight criteria with $p_{\mathrm{T}} > 24$ GeV , or a non-isolated tight muon with $p_{\mathrm{T}} >36$ GeV. The tight muon criteria, imply that the muon belongs to the Combined collection (or StandAlone if it is in $\eta > 2.5$) and a successful re-fit has been performed by combining all the track segments in the components of the Muon Spectrometer. For the electrons trigger, an isolated electron which passes the medium criteria, of the variables related to the shower shapes in the calorimeter with E_{T} >24 GeV or a looser trigger cut for high E_{T} electrons with E_{T} >60 GeV.

For the di-electron pair, the electrons are required to have E_{T} >10 GeV and to be in $|\eta| <$ 2.47. The angular separation for the two electrons should be $\Delta R > 0.1$. Also, the ratio of the normalised p_{T} sum around a cone of $\Delta R < 0.2$, surrounding the electron track over the total p_{T} of the electron should be less than 15%. Similarly, the ratio of the normalised sum of calorimetric energy deposition E_{T} around a cone of $\Delta R < 0.2$ from the electron cluster over the cluster energy should be less than 20%. To exclude cosmic-rays background, the transverse impact parameter significance for each lepton should be $d_0/\sigma_{d_0} < 6.5$.

For the di-muon pair, the muons are required to belong in the Combined reconstruction category, with $p_{\mathrm{T}} > 20$ GeV and $|\eta| < 2.5$. The angular separation of the two muons should be $\Delta R > 0.1$. The impact parameter significance for each lepton is required to be $d_0/\sigma_{d_0} < 3.5$. Similarly to the electrons, the ratio of the normalised sum of the p_{T} around the muon track in a cone of $\Delta R < 0.2$ over the total p_{T} should be less than 15% whereas for the cluster energy E_{T} the ratio should be less than 30%.

Focusing now on the non-collinear FSR, after the selection of the events an additional search takes place looking for those FSR photons in the events. The non-collinear photons which pass the respective criteria (Table 5.1) will be considered for the FSR correction. The correction is applied only if the di-lepton pair has invariant mass $m_{\ell\ell} < 81$GeV . The far FSR inclusion remains under the condition that the new invariant mass ($m_{\ell\ell\gamma}$) is below 100 GeV ($m_{\ell\ell\gamma} < 100$ GeV).

The selection of $m_{\ell\ell} < 81$GeV was chosen because it is the region with the highest signal-to-background ratio. Figure 5.2 depicts the invariant mass, before the correction, of the events which have a selected FSR photon. The background contains events with a fake FSR originating from QCD/hadronic jets, which are the most dominant in the high E_{T} region. As it is shown in the figure, the events with a true FSR photon are corrected, increasing the amount of events in the Z mass window.

For collinear FSR, the photon is added to di-muon pair if $66 < m_{\mu\mu} < 89$ GeV , $m_{\mu\mu\gamma}$ <100 GeV. For di-electron pairs, no FSR correction is performed for collinear photons, due to the fact that it is very difficult to clear separate the EM cluster formed in the calorimeter from the FSR photon to the one from electron, in such small separation angle. The effect of the collinear FSR correction in the $Z \rightarrow \mu^+\mu^-$ events is shown in Figure 5.3. The ratio of the $Z \rightarrow \mu^+\mu^-$ events which were corrected for collinear FSR is approximately 4% [59].

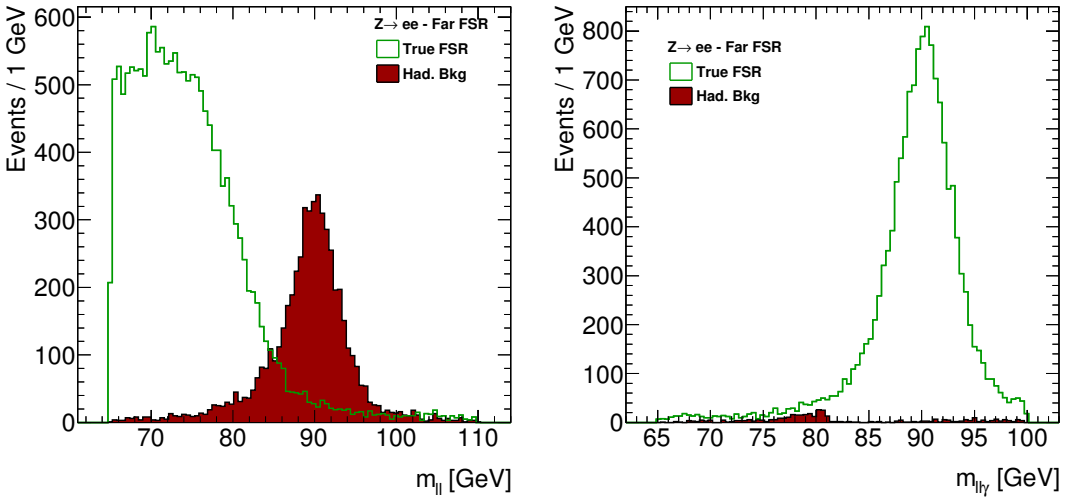

(a) $m_{\ell\ell}$ **(b)** $m_{\ell\ell\gamma}$

Figure 5.2: Distribution of the invariant mass of the events with an FSR photon of either true or fake origin, before ($m_{\ell\ell}$) and after ($m_{\ell\ell\gamma}$) the correction.

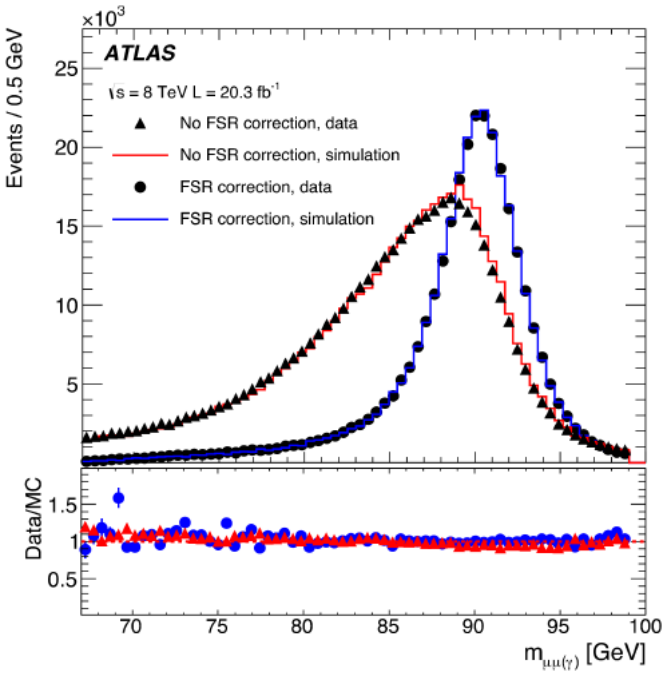

Figure 5.3: Invariant mass distribution of $Z \to \mu^+\mu^-$ events with identified FSR in data before (triangles) and after (circles) FSR correction, for collinear FSR. The MC prediction is shown before correction (red histogram) and after correction (blue histogram). Figure from [59].

5.3.3 Far FSR effect on $Z \to \ell\ell$

Two ratios define the quality of the FSR correction. The **efficiency**, which is defined as the ratio of the reconstructed far FSR photons which are matched with a true MC far FSR photon, over the amount of MC far FSRs which passes the fiducial selection.

The other ratio is called **purity** and expresses the ratio of the reconstructed far FSR photons which are matched with a true one, over all the reconstructed far FSRs.

$$\text{efficiency} = \frac{\text{Reco far FSR - truth matched}}{\text{MC Far FSRs in selection}} \tag{5.1}$$

$$\text{purity} = \frac{\text{Reco far FSR - truth matched}}{\text{All reco far FSR}} \tag{5.2}$$

For the $Z \to \mu^+\mu^-$ events, it is found that 1% of events are corrected for far FSR, with an efficiency of the selection of 60±3% and purity of ≥95%. Likewise, the fraction of corrected events for the $Z \to e^+e^-$ case is slightly lower (≈ 0.5%). The efficiency in this case is 30±5% and the purity ≥95%.

The corrected mass compared with the uncorrected one for selected events containing a far FSR photon which pass the selection, is shown in Figure 5.4 for $Z \to \mu^+\mu^-$ and on Figure 5.5 for $Z \to e^+e^-$. Figures 5.6, and 5.7, depict the separation of the lepton with the far FSR and the E_{T} of the far FSR for $Z \to \mu^+\mu^-$ and $Z \to e^+e^-$ cases respectively.

A comparison between the reconstructed and the true invariant mass for the events corrected with far FSR is shown in Figure 5.8. The difference in the masses is significantly improved since the reconstructed Z boson mass after the correction is very close to the MC truth one.

The inclusion of the FSR photons shifts the gaussian mean and improves the resolution when applied on data. A shift of the invariant mass distribution by +40±3 MeV in the $Z \to \mu^+\mu^-$ (collinear and far FSR) channel, and an improved resolution by a factor of 3±1% is observed. Likewise, for the $Z \to e^+e^-$ channel, the inclusion of the far FSR introduces a shift of +1±4 MeV and an improvement in resolution of 0.03±0.24%. Figure 5.9 illustrates this effect.

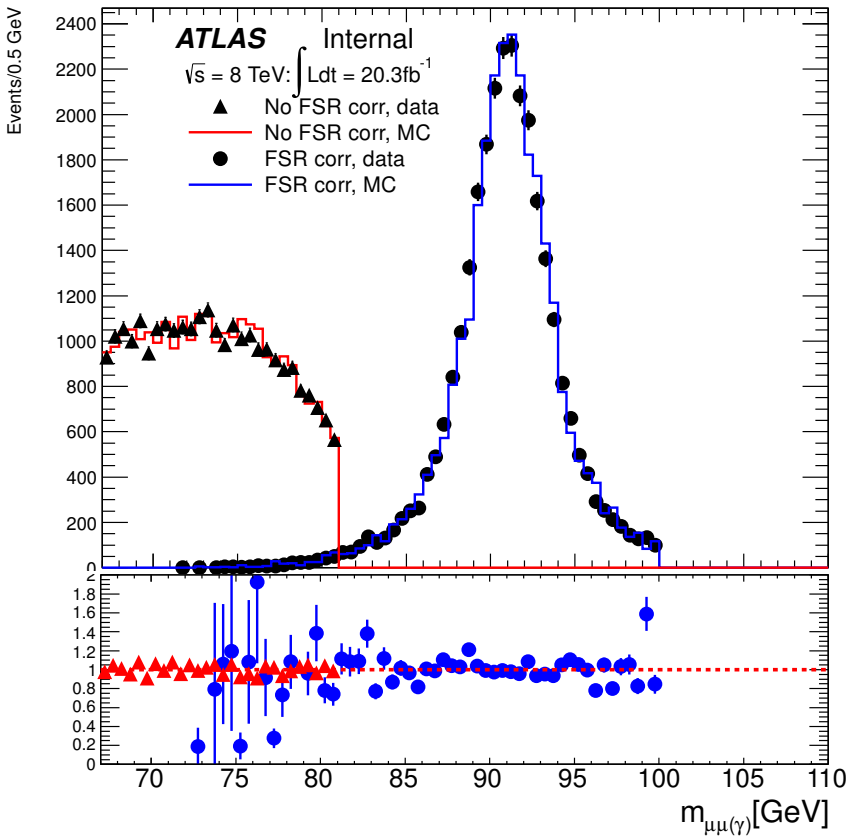

Figure 5.4: Invariant mass distribution of $Z \to \mu^+\mu^-$ events with a selected far FSR , before (MC: red line, Data: triangles) and after (MC: blue line, Data: circles) the correction. A similar effect is observed in both MC and data with successful recovery of the Z candidates.

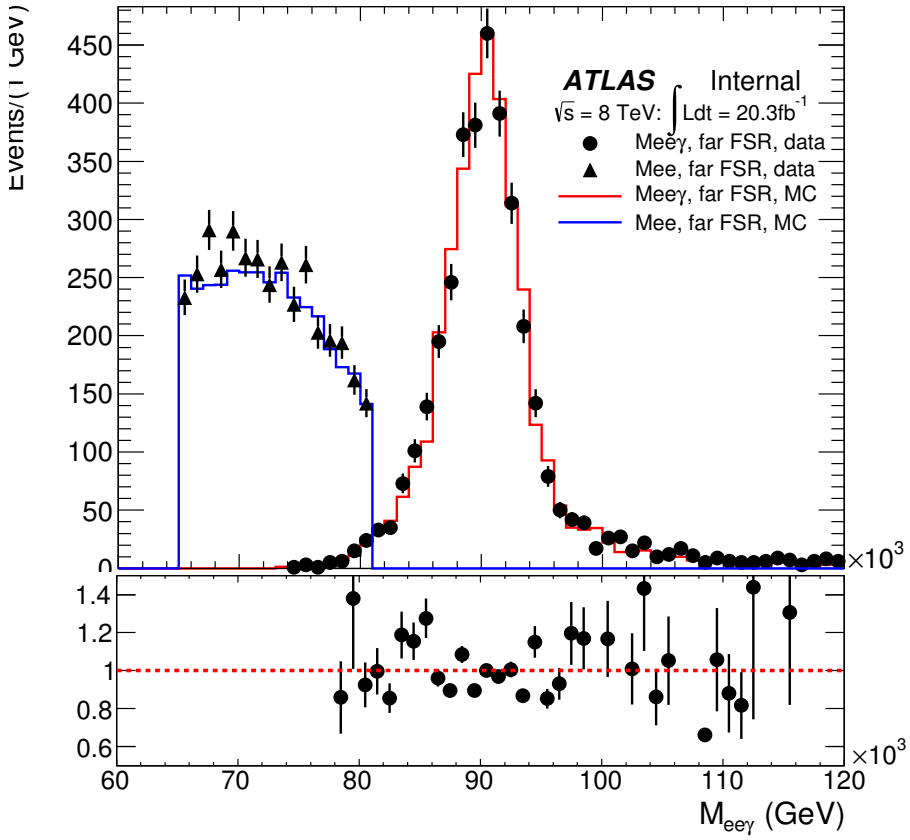

Figure 5.5: Invariant mass distribution of $Z \to e^+e^-$ events with a selected far FSR , before (MC: blue line, Data: triangles) and after (MC: red line, Data: circles) the correction. A similar effect is observed in both MC and data with successful recovery of the Z candidates.

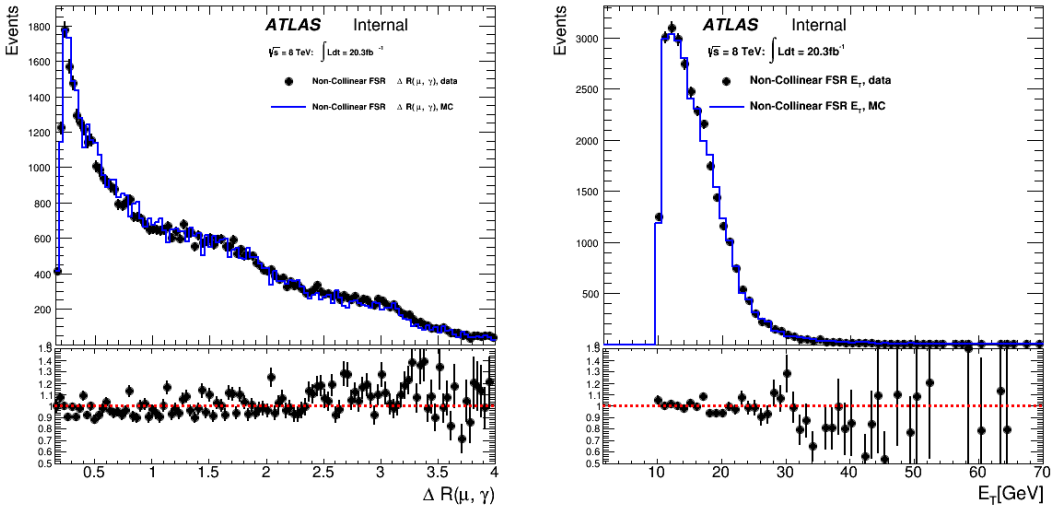

(a) $Z \to \mu^+\mu^-$, $\Delta R(\mu, \gamma)$ **(b)** $Z \to \mu^+\mu^-$, $E_{\mathrm{T}}\gamma)$

Figure 5.6: Distribution of (a) $\Delta R(\mu, \gamma)$ and (b) the E_{T} for the $Z \to \mu^+\mu^-$ far FSR search. Excellent agreement is observed between data and MC.

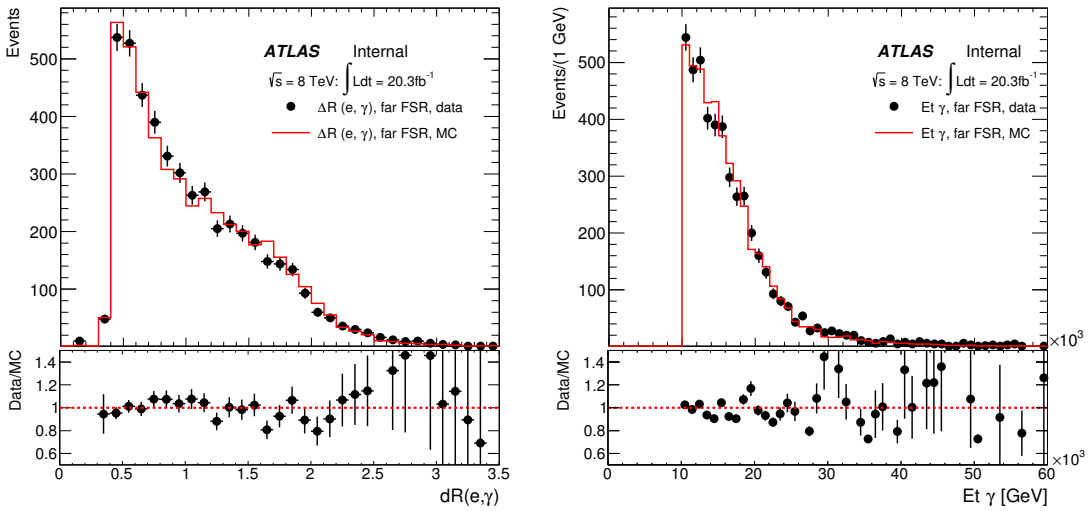

(a) $Z \to e^+e^-$, $\Delta R(e, \gamma)$ **(b)** $Z \to e^+e^-$, $E_{\mathrm{T}}\gamma)$

Figure 5.7: Distribution of (a) $\Delta R(e, \gamma)$ and (b) the E_{T} for the $Z \to e^+e^-$ far FSR search. Excellent agreement is observed between data and MC.

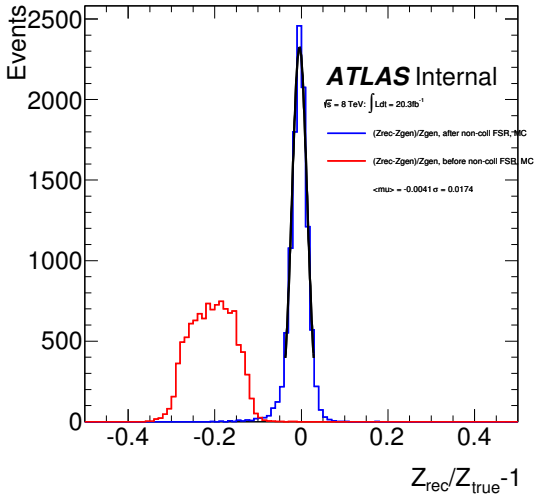

(a) $Z \to \mu^+\mu^-$

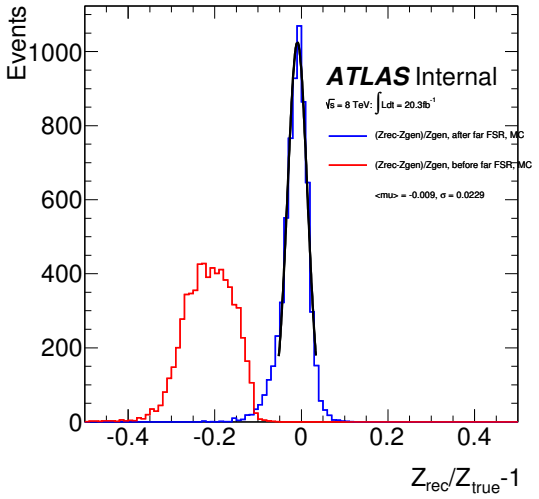

(b) $Z \to e^+e^-$

Figure 5.8: Invariant mass comparison, $(Z_{\text{rec}}/Z_{\text{true}}) - 1$, before (red) and after (blue) the far FSR correction in events with an FSR selected photon for (a) $Z \to \mu^+\mu^-$ and (b) $Z \to e^+e^-$ channel. Z_{rec} is the invariant mass of the reconstructed Z boson after the inclusion of the far FSR and Z_{true} is the Z boson invariant mass, corresponding to the MC truth information of the event.

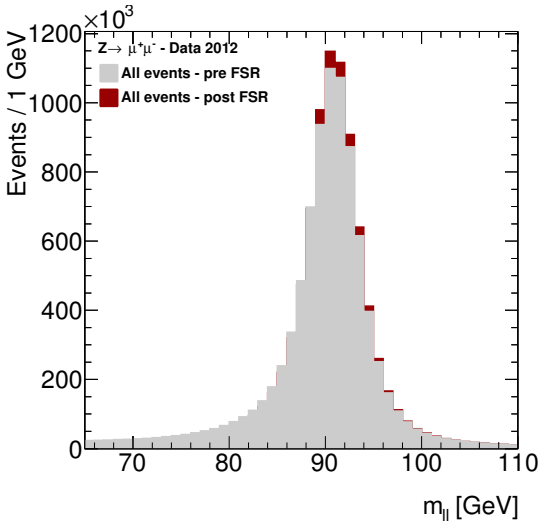

(a) $Z \to \mu^+\mu^-$

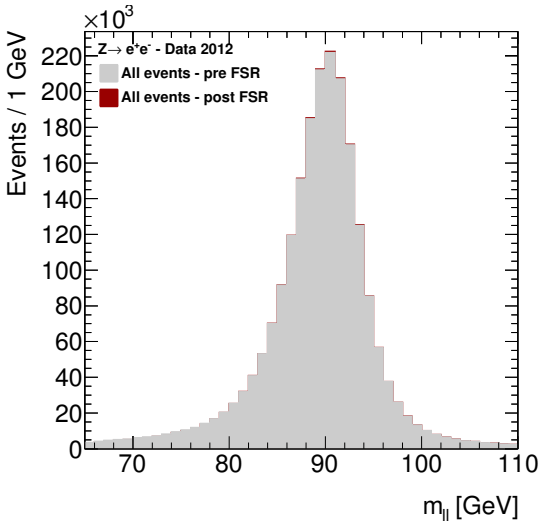

(b) $Z \to e^+e^-$

Figure 5.9: Distribution of the invariant mass for all the events, before and after the far FSR recovery for the for (a) $Z \to \mu^+\mu^-$ and (b) $Z \to e^+e^-$ channel.

5.4 Final State Radiation in the $H \to ZZ^{(*)} \to 4l$ mass measurement

The $H \to ZZ^{(*)} \to 4l$ mass measurement was the first analysis which included the Final State Radiation recovery. With the Higgs boson discovery, the mass of the particle is known ($m_H \approx$ 125 GeV). Due to the FSR radiation, many $H \to ZZ^{(*)} \to 4l$ events are reconstructed with four leptons invariant mass shifted to lower values. Therefore, the FSR recovery tries to increase the number of events in the signal region which have correct invariant mass.

The collinear FSR recovery was the first which was added in the analysis on December 2013, improving the mass measurement by a few MeV [79]. For the 8 TeV data analysis[67], the $H \to ZZ^{(*)} \to 4l$ channel included the far FSR recovery too.

5.4.1 Summary of $H \to ZZ^{(*)} \to 4l$ mass measurement analysis

The $H \to ZZ^{(*)} \to 4l$ analysis is looking for four isolated and well reconstructed leptons (electrons, muons) which can form two Z boson candidates. In the following sections, the selection criteria of the analysis will be described as they were used by the $H \to ZZ^{(*)} \to 4l$ analysis group [67] and are summarised on Table 5.2.

Firstly, a trigger requirement is applied to the events. For the 8 TeV data, the single muon and electron trigger have low p_{T} thresholds of 20 GeV and 25 GeV respectively. Di-leptons trigger requirements are also applied. For the di-electron trigger the low p_{T} threshold is 12 GeV. For the di-muons case, there is a single threshold of 13 GeV but also an asymmetric threshold of either 8 or 18 GeV.

The **electron** candidates should have well-reconstructed tracks from the Inner Detector. They should pass the "loose" likelihood [80] ATLAS identification criteria. They should have E_{T} >7 GeV and be in $|\eta|$ <2.47. The transverse impact parameter significance requirement is $d_0/\sigma_{d_0} < 6.5$.

The **muon** candidate should belong to any of the reconstruction categories. The analysis allows at most one StandAlone or Calo-Tag muon per event. The candidate should also have hits in the Inner Detector or to have been recorded in all Muon Spectrometer stations in case of StandAlone. The muons should have p_{T} >6 GeVand be $|\eta|$ <2.7, with an impact parameter significance cut of $d_0/\sigma_{d_0} < 3.5$.

To ensure that the leptons originate from the primary vertex, the lepton tracks must have distances $|z_0| < 10$ mm from the primary vertex (the one with the largest sum of p_{T}^2) along the proton beam pipe. Additionally, the muons are required to have transverse impact parameter ("$|d_0| < 1$ mm"), to reduce any cosmic background.

5.4.2 Event selection

After the selection of the objects, two same-flavour, opposite-sign lepton pairs (a quadruplet) are required. The events are classified into four channels, according to the leptons which comprise the quadruplet and the flavour of the leading di-lepton pair. The channels are: 4e,4μ,2e2μ,2μ2e.

Initially, one lepton of the quadruplet should have $p_{\mathrm{T}} > 20$ GeV, the next one $p_{\mathrm{T}} > 15$ GeV and the last one $p_{\mathrm{T}} > 10$ GeV respectively. The di-lepton pair with mass closest to the known Z mass is called the "leading pair" and the second closer is called as the "sub-leading" one.

The leading di-lepton pair is required to have mass $50 < m_{12} < 106$ GeV . The sub-leading pair, is required to have maximum mass to 115 GeV with varied minimum threshold; If the four leptons invariant mass is lower than 140 GeV then, the minimum requirement is $m_{34} > 12$ GeV, with a linear interpolation up to 50 GeV if $m_{4l} = 190$ GeV, remaining there for any other higher m_{4l} invariant mass. An extra J/ψ mass veto is applied, removing the quadruplet if any combination $m_{\ell\ell} < 5$ GeV . Also, it is ensured that the leptons are isolated with the $\Delta R(\ell, \ell') > 0.10(0.20)$ for all same (different) flavour leptons in the quadruplet.

Further isolation criteria include the normalised sum of the transverse momenta of tracks, $\sum p_{\mathrm{T}}$, inside a cone of $\Delta\mathrm{R} < 0.2$ around the lepton, without the lepton track, divided by the lepton p_{T}. For muons, the tracks have at least four hits in the pixel and silicon strip detectors ("silicon hits") and $p_{\mathrm{T}} > 1$ GeV. For electrons, the tracks are required to have at least nine silicon hits, one hit in the innermost pixel layer (the b-layer) and $p_{\mathrm{T}} > 0.4$ GeV. Each lepton is required to have a normalised track isolation smaller than 0.15.

The normalised calorimetric isolation discriminant for muons is defined as the sum of the calorimeter cells, $\sum E_{\mathrm{T}}$, inside an isolation cone of 0.20 around the muon divided by the muon p_{T}. In the case of electrons, the normalised calorimetric isolation is computed as the sum of the topological cluster energy E_{T} inside a cone of 0.2 around the electron cluster, divided by the electron p_{T}.

Muons are required to have a normalised calorimetric isolation of less than 0.30, while for electrons the corresponding value is 0.20. For both the track- and calorimeter-based isolation, any contributions arising from other leptons of the quadruplet are subtracted. For the track isolation the contribution from any other lepton in the quadruplet within $\Delta\mathrm{R} < 0.2$ is subtracted. For the calorimetric isolation the contribution of any electron in the quadruplet within $\Delta\mathrm{R} < 0.18$ is subtracted.

The FSR recovery is followed by a kinematic fit which constraints the invariant mass of the leading pair to the Z boson taking into account the lineshape and the experimental uncertainties.

At the final level, if more than one channel has a quadruplet which passes the selection, the channel with the highest Higgs expected yield is kept following the order: $4\mu, 2e2\mu, 2\mu2e, 4e$.

Table 5.2: Summary of the event selection requirements. The two lepton pairs are denoted as m_{12} and m_{34}.

Event selection	
	Good runs list
Trigger	Single electron: e24vhi_medium1 OR e60_medium1 Di-electron: 2e12Tvh_loose1 Single muon: mu24i_tight OR mu36_tight Di-muon: 2mu13 OR mu18_tight_mu8_EFFS El-muon: e12Tvh_medium1_mu8 OR e24vhi_loose1_mu8
Object selection	
Electrons	Loose LH quality electrons with $E_{\mathrm{T}} > 7$ GeV and $\lvert\eta\rvert < 2.47$
Muons	Combined or segment-tagged muons with $p_{\mathrm{T}} > 6$ GeV and $\lvert\eta\rvert < 2.7$ Maximum one calo-tagged or standalone muon Calo-tagged muons with $p_{\mathrm{T}} > 15$ GeV and $\lvert\eta\rvert < 0.1$ Standalone muons with $p_{\mathrm{T}} > 6$ GeV ,$2.5 < \lvert\eta\rvert < 2.7$ and $\Delta R > 0.2$ from closest segment-tagged
Quadruplet Selection	
Kinematic Selection	- Ask for at least one quadruplet of leptons consisting of 2 pairs of same-flavour opposite-charge - p_{T} cuts for the 3 first leptons in the quadruplet: 20, 15 and 10 GeV - Leading di-lepton: the one closer to the Z PDG mass - Sub-leading di-lepton: the second closer to the Z PDG mass . - Leading Z mass requirement 50 GeV $< m_{12} <$ 106 GeV - Sub-leading Z mass requirement $m_{\mathrm{threshold}}$ GeV $< m_{12} <$ 106 GeV $m_{\mathrm{threshold}}$ = 12 GeV if $m_{4\ell}$ <140 GeV $m_{\mathrm{threshold}}$ linearly up to 50 GeV in $m_{4\ell} \in$ [140 GeV, 190 GeV] $m_{\mathrm{threshold}}$ = 50 GeV if $m_{4\ell}$ >190 GeV - Remove quadruplet if alternative same-flavour opposite-charge di-lepton gives $m_{\ell\ell} < 5$ GeV - $\Delta R(\ell, \ell') > 0.10$ for same flavour leptons in the quadruplet. - $\Delta R(\ell, \ell') > 0.20$ for different flavour leptons in the quadruplet.
Quadruplet cuts	
Isolation	- Lepton track isolation ($\Delta R = 0.20$): $\Sigma p_{\mathrm{T}}/p_{\mathrm{T}} < 0.15$ - Electron calorimeter isolation ($\Delta R = 0.20$) : $\Sigma E_T/E_T < 0.20$ - Muon calorimeter isolation ($\Delta R = 0.20$) : $\Sigma E_T/E_T < 0.30$ - Stand-Alone muons calorimeter isolation ($\Delta R = 0.20$) : $\Sigma E_T/E_T < 0.15$
Impact Parameter Significance	- For electrons : $d_0/\sigma_{d_0} < 6.5$ - For muons : $d_0/\sigma_{d_0} < 3.5$

5.4.3 FSR recovery in $H \to ZZ^{(*)} \to 4l$

The FSR recovery in the $H \to ZZ^{(*)} \to 4l$ analysis employs a special tool, which performs the search for an identified photon or EM clusters complying with the criteria required for FSR photons around a lepton. A single photon candidate is returned giving priority to collinear photons. If more than one candidate is found the one with the highest E_{T} is selected. Every lepton in the quadruplet is searched for FSR photon and a maximum of one FSR photon candidate is allowed to be added to one of the two Z boson candidates. After successful search of a photon candidate, the photon is temporarily added to the Z candidate. If the new invariant mass ($m_{ll\gamma}$) is below a specific threshold, then the correction is considered successful and the invariant mass of the Z candidate includes now the FSR photon.

The steps of the FSR correction method are detailed below:

1. Priority is given to collinear photons associated to the leading Z candidate and are searched through $Z \to \mu^+\mu^-$ decays.

   - **If a collinear FSR is found from the FSR tool for the leading Z (m_{12}) ,in the 4μ or the $2\mu 2e$ case, then this one is used:**

     The FSR correction is applied if:

     $66 < m_{\mu\mu} < 89$ GeV and

     $m_{\mu\mu\gamma} < 100$ GeV

2. If the collinear search has failed either at the tool level (did not pass the photon cuts) or at the analysis level (did not pass the m_{12} cuts) then a far FSR is searched in all four leptons:

   - The far FSR found with highest E_{T} is required to have an angular separation $\Delta R(l, \gamma) > 0.15$ from all the leptons

     If the invariant mass of the four leptons is m_{4l} <190 GeV:

     The correction is applied to the leading Z (m_{12}) boson, of any channel, which satisfies:

     $m_{ll} < 81$ GeV and

     $m_{ll\gamma} < 100$ GeV

     If the invariant mass of the four leptons is m_{4l} >190 GeV:

     The correction is applied to any Z candidate with:

     $m_{ll} < 81$ GeV and

     $m_{ll\gamma} < 100$ GeV

     If both Z1 or Z2 satisfy the cut $m_{ll} < 81$GeV, the FSR correction is applied to the pair whose corrected mass is below 100 GeV and the closest to Z pole

Based on MC studies using a Higgs signal sample with $m_H = 125$ GeV, for collinear FSR 4% of the total $H \to ZZ^{(*)} \to 4l$ events of the channels where the collinear correction can be applied (4μ and 2μ2e) are expected to be corrected. For far FSR the fraction drops to 1%. The effect of the correction at the four lepton invariant mass for events containing FSR is shown on Figure 5.10.

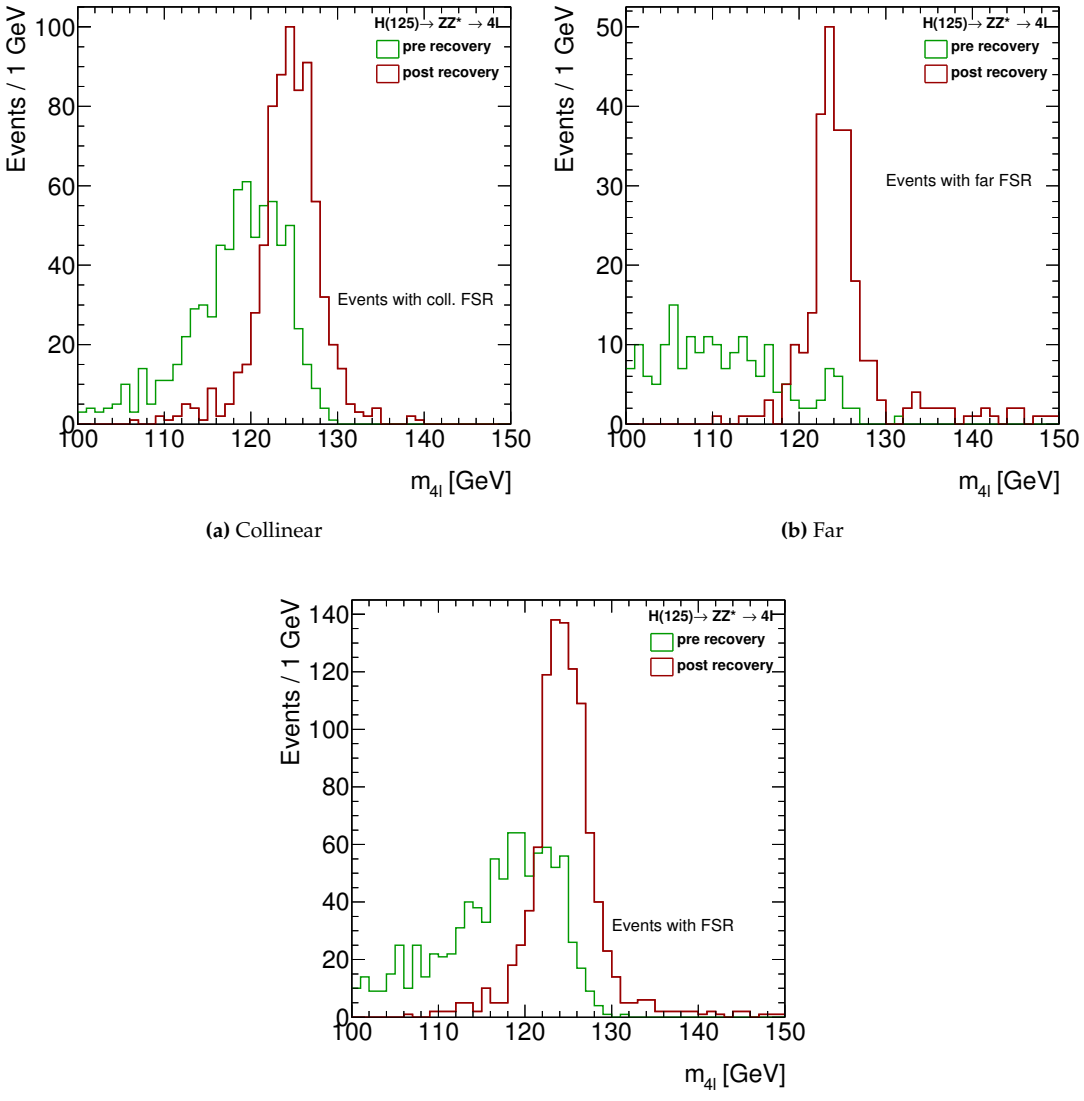

(a) Collinear

(b) Far

(c) All

Figure 5.10: MC invariant mass distribution m_{4l} of simulated Higgs 125 GeV decaying to four leptons, for events with an identified FSR photon, before (green) and after (red) the FSR correction in case of (a) Collinear FSR, (b) Far FSR, (c) all events.

The correction is very efficient regarding the transition of the corrected events. For the events with an identified far FSR, 75% of them have pre-corrected reconstructed mass outside the signal region and are brought to the signal region after the correction.

From the events with an identified collinear FSR, 48% of the corrected ones are brought inside the signal region after the correction.

The Figure 5.11 shows the transition of the corrected events ,whose mass is outside the signal region, to the signal region (120-130 GeV).

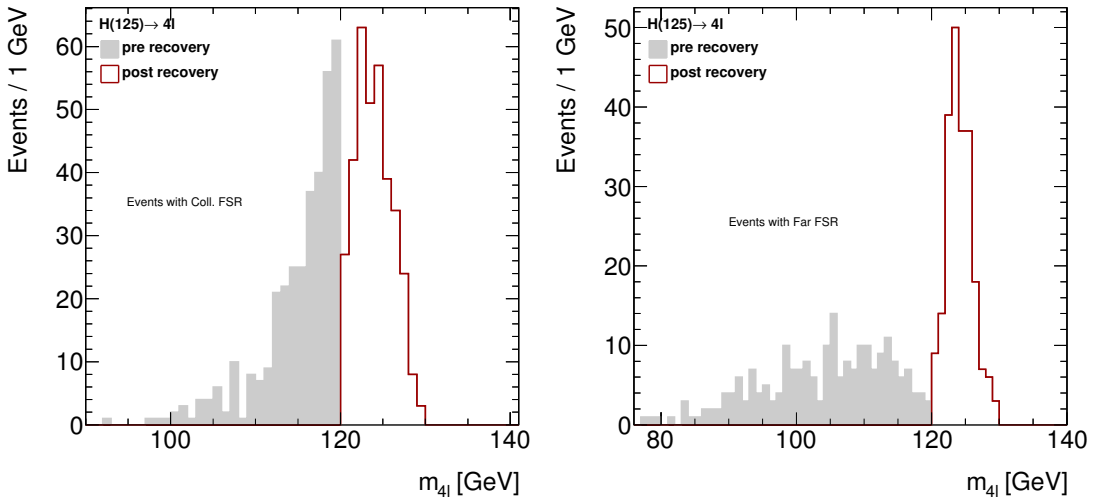

(a) Collinear **(b)** Far

Figure 5.11: MC invariant mass distribution m_{4l} of simulated Higgs 125 GeV decaying to four leptons, for events with an identified FSR photon, who enter the signal region after the correction for (a) Collinear FSR and (b) Far FSR.

From the total number of $H \to ZZ^{(*)} \to 4l$ events, the ratio of events which after the correction enter the signal region of 120-130 GeV is 0.7% for far FSR and 3.5% of for collinear FSR respectively. For both collinear and far FSR, there is a negligible fraction of events (0.17%) which are transferred outside the signal region after the correction.

For the effect at the irreducible ZZ background, the correction is applied also to the background candidates which pass the ZZ selection, as described before. The result shows that 1.6% and 1.1% of the total events in the full invariant mass spectrum are expected to be corrected for collinear and far FSR respectively. From the events corrected, only 0.06% of the events corrected with collinear FSR photons, have final invariant mass in the signal region. For the far FSR photons, this ratio is lowered to 0.01%.

The comparison of the ratio of events which enter the signal region after the FSR correction between signal and background, in the background sample, shows a clear difference in the probability of events to enter the Higgs signal region after the FSR correction.

Table 5.3: Comparison of ratio of events which are transferred, after FSR correction, to and from the signal region (SR), between a Higgs signal with $m_H = 125$ GeV and ZZ background. For background the information about the events which could enter the signal region is needed only.

	Higgs signal			ZZ background	
FSR type	Total	Enter SR	Leave SR	Total	Enter SR
Collinear	4%	3.5%	0.16%	1.6%	0.06%
Far	1%	0.7%	0.17%	1.1%	0.01%

5.4.4 Results on 2012 data

The analysis performed on the 2012 dataset yielded 428 Higgs candidates[67]. The categorisation of the events was 137 in the 4μ channel, 88 at the 2μ2e, 79 at the 4e and 124 at the 2e2μ. Overall, 7 events were corrected for collinear FSR and 2 for far FSR, verifying the expected ratios for the channels were the correction can be performed. For the signal region (120-130 GeV), only 3 events were found which are brought to the signal region after the correction. Table 5.4 details the events in the signal region with FSR photon.

Table 5.4: List of the events in the signal region with FSR photon. The invariant masses are in GeV

Channel	FSR Type	m4l	m4l+FSR	m4l final
2μ2e	Far	95.771	126.453	126.765
2μ2e	Coll	109.911	123.955	126.754
4μ	Far	113.425	123.527	123.736

After the full analysis, the Higgs boson mass was measured through the $H \to ZZ^{(*)} \to 4l$ channel, with the combined dataset of 7 and 8 TeV, $m_H = 124.51 \pm 0.52(\text{stat}) \pm 0.06(\text{syst})$ GeV.[67]. The best-fit value is shown in Figure 5.12.

For comparison, the first Higgs mass measurement in $H \to ZZ^{(*)} \to 4l$ channel, after the discovery, without the FSR correction was calculated: $m_H = 123.5 \pm 0.9(\text{stat}) \pm 0.3(\text{syst})$ GeV. [81]. The following one measurement included only the collinear FSR correction and the fitted mass was found: $m_H = 124.3^{+0.6}_{-0.5}(\text{stat})^{+0.5}_{-0.3}(\text{syst})$ GeV [82].

5.5 Conclusion

The FSR photon recovery has been realised thanks to the performance of the ATLAS EM calorimeter where the photons can be identified and recovered at low energy levels of around 1.5 GeV. The study of the $Z \to \ell\ell$ decay can be benefitted from the FSR correction for both collinear and far FSR, by reconstructing properly the Z candidates and improving the resolution of the mass to smaller values.

Using the previous elements in the $H \to ZZ^{(*)} \to 4l$ analysis, there is a twofold benefit from the inclusion of the FSR correction. Firstly, the tails of the distribution are reduced and the lineshape is improved. As a result of this, the fitted Higgs mass resolution in the signal region

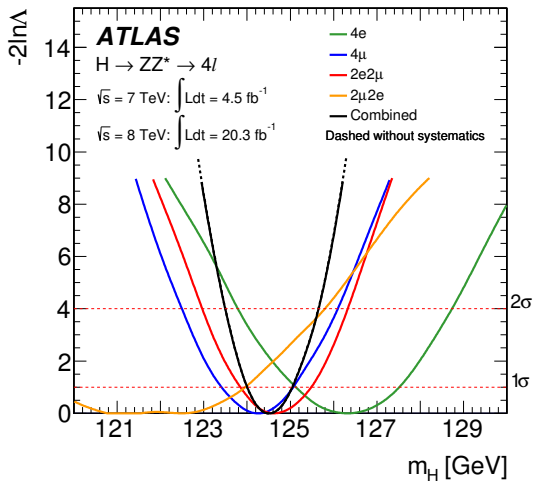

Figure 5.12: The profile likelihood as a function of mH for the combination of all $H \to ZZ^{(*)} \to 4l$ channels and for the individual channels for the combined 7 TeV and 8 TeV data samples. The combined result is shown both with (solid line) and without (dashed line) systematic uncertainties.[67]

can be improved by having a narrow peak. In addition, counting in the known Higgs signal window, extra signal events are brought inside, without contamination from background, increasing the amount of the well recontructed Higgs candidates.

Chapter 6

Measurement of the Double Drell-Yan process

This chapter presents the measurement of the cross-section of Double Drell-Yan process using the 8 TeV dataset, with studies regarding the properties of Double Parton Interaction (DPI). The author conducted the analysis as part of ATLAS internal studies regarding the contribution of DPI in $H \to ZZ^{(*)} \to 4l$ analysis.

6.1 Introduction

A Double Parton Interaction is the occurrence of two hard parton scatterings within the same hadron-hadron collisions. The study of DPI allows further investigation on the proton structure and the correlations between interacting partons. The DPI is a QCD described process and past studies involved the study of jets originating from either quark of gluon hadronisation.

The measurement of the exclusive fiducial cross-section $\sigma_{\text{DPI}\to Z+Z\to 4l}$ takes place for the first time using ATLAS data. With the increase of the energy levels, a better knowledge of background processes is required. Since the four-leptons (4l) final state is important for many searches, like Higgs decaying to four leptons, or the SM ZZ to four leptons system, the contribution from other background sources should be estimated. At these new energy levels, the contribution from DPI DDY is unknown and thus it should be estimated. Additionally, the knowledge of the DDY DPI production cross-section is essential for the understanding of the proton structure, through the double parton interactions, providing a better understanding of the distribution of the partons inside the proton.

As it has been mentioned in Chapter 1, one of the possible DPI processes is the Double Drell-Yan annihilation (DDY)[35], where two Drell-Yan $q\bar{q} \to Z/\gamma* \to \ell\ell$ come from two independent $q\bar{q}$ hard scatterings with the leptonic final state containing electron pairs or muons pairs.

This study focuses on two on-shell Z bosons produced through DDY annihilation, which decay to four leptons. The consideration of a fully leptonic final state has the advantage of accurate lepton reconstruction with low systematic uncertainties compared to jets. Therefore, the DDY offers a clean probe of a Leading Order quark-antiquark process. Also, the theoretical considerations regarding the lepton production are well-understood compared to jet production. In the present measurement, the cross-section takes place in a phase-space which corresponds closely to the experimental acceptance and is corrected for experimental inefficiences of the ATLAS detector.

6.2 Theoretical considerations

The theoretical formulation of the nature of DPI is still unknown. Therefore, there is an absence of a theoretical model which could describe the DPI DDY production mechanism. In a simple approximation, the DDY cross-section is the product of two single Drell-Yan interactions. The translation of the two single interactions to a double is performed with a factor which is phenomenologically related to the distribution of the partons at the interaction plane [29]. Therefore, the cross-section of the double interaction is related to the product of two single interactions which would result a significantly lower cross-section compared to the single one.

The transverse plane of the interaction can be described with the "effective cross-section factor" σ_{eff} . The σ_{eff} is defined in parton level and is associated with the effective area of the interaction, the momentum of the hard scatters and other correlations between the two interacting partons.

For the interpretation of the cross-section into the DPI context, the simple factorisation model [83, 29] is assumed. According to this model, the probability of the multiparton interactions has Poissonian distribution. A three-dimensional parton density is introduced which describes the average number of partons with a given momentum fration and transverse coordinate. Therefore, the dependence of previous parton density to transverse and longitudinal degrees of freedom can be factorised to the usual parton distribution function and a function which represents the distribution of the partons at the transverse space. Due to the large uncertainty in the cross-section measurement, a lower limit in the DDY cross-section is extracted which is translated into an upper limit for σ_{eff} .

As shown in 1.47, the Double Drell-Yan cross-section can be written as:

$$\sigma_{\text{DPI}} = \frac{m}{2} \times \frac{\sigma_{\text{SPI1}} \times \sigma_{\text{SPI2}}}{\sigma_{\text{eff}}} \tag{6.1}$$

where the symmetry factor "m" equals 1 for indistinguishable processes and 2 for distinguishable processes; σ_{SPI} is the cross-section of the single parton interaction processes.

6.3 Monte Carlo modelling

6.3.1 Signal modelling

The DPI DDY $Z+Z \rightarrow 4l$ is modelled by introducing a second $Z \rightarrow \ell\ell$ hard process on the same event. The second hard scattering ($Z \rightarrow \ell\ell$) it is assumed to originate from the Double Drell-Yan process. However, given the absence of any standard theoretical description of DPI DDY it should be noted that the simulated DDY is used only for the event topology, the shape of the observables and the analysis selection efficiency, without any prior assumptions about the σ_{eff} or the factorisation of double PDFs. The simulated signal is generated in PYTHIA 8 MC generator [76]. A full description of the way that PYTHIA 8 handles multiparton interactions is available at [84].

After the generation, the sample is interfaced to PHOTOS for quantum electrodynamics (QED) radiative corrections in the final state. The generated Z boson signal events are decaying and hadronized with Pythia using the AU2 underlying-event tune for the fine-structe constant (α_s) [85] adjusted to experimental ATLAS data. The LO CTEQ6L1 [75] parton distribution function (PDF) for the single parton interactions is used.

6.3.2 Background modelling

The only background source for the DPI study is the Standard Model ZZ continuum, through the $q\bar{q}$ →ZZ and gg →ZZ processes.

The $q\bar{q}$ →ZZ background is modelled using POWHEG which is NLO in QCD [69], using a re-normalisation and factorisation scale of m_{ZZ} and the CT10 NLO PDF set[70]. The PYTHIA 8 generator [76] is used for hadronization and showering.

The gg→ZZ background is modelled to LO accuracy using the gg2VV MC generator[86], interfaced to PYTHIA 8 for hadronization and showering. The CT10 NNLO PDF set is used, since the LO gg→ZZ process is part of the NNLO calculation for pp→ ZZ.

6.4 Analysis overview

The analysis is similar to the Higgs to four leptons analysis which is detailed in Chapter 5.The main difference from the Higgs analysis is the additional DPI-related selection at the end. The mass range of the Z boson candidates lies for both between $50 < M_Z < 106$ GeV; the four lepton mass should be $m_{4\ell}$ >170 GeV, since the analysis has on-shell Z candidates; the azimuthal angle between the Z candidates should be $\Delta\phi < 2.1$. An overview of the DPI-related selection is shown at the Table 6.1.

Table 6.1: Summary of the DPI related cuts in the four lepton analysis. The two lepton pairs are denoted as m_{12} and m_{34}.

	DPI cuts
On-shell Z bosons	- Di-lepton mass requirement 50 GeV $< m_{12/34} <$ 106 GeV
Z pairs angle	- $\Delta\phi(m_{12}, m_{34}) < 2.1$
Invariant mass of 4ℓ	- $m_{4\ell} > 170$ GeV

6.4.1 DPI selection

Initially, the region of interest for the analysis is the high mass regime ($m_{4l} > 170$ GeV) of the ZZ final state. The analysis follows the same selection as the Heavy Higgs with $ZZ \to 4l$ final state [87] and thus the contribution of the background is expected to be similar. The reducible background like Z+jets or $t\bar{t}$ is negligible, at a level of less than 0.1 expected events. The only background source present in the high mass regime is the Standard Model ZZ continuum with a rate of expected events of more than 250 events [87].

The difference of the azimuthal angle ($\Delta\phi$) of the two Z bosons, depicted in Figure 6.1, is used as a discriminant between the background and the signal (DPI) events. In the ϕ-space, the Z pairs from the irreducible background, $q\bar{q} \to ZZ^{(*)}$and $gg \to ZZ^{(*)}$, are back-to-back in order to perserve the momentum of the di-boson system on the rest frame. On the contrary, the Z boson pairs from DPI DDY have uniform distribution.

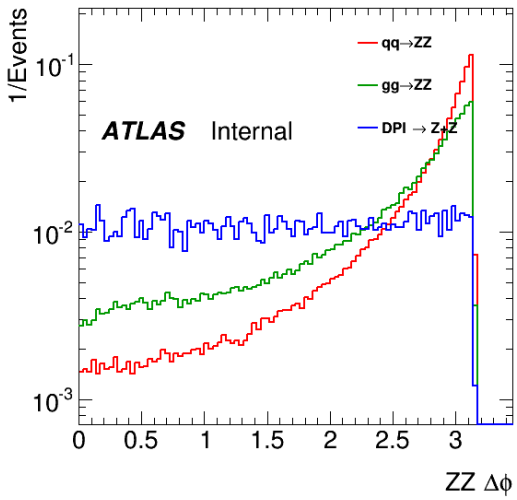

Figure 6.1: Distribution of the azimuthal angle $\Delta\phi$ for the signal and background events which are in the signal region

The choice of the $\Delta\phi < 2.1$ was found to provide the maximum signal to background rate.

For both background components, after the selection of the Z candidates, the reduction is a factor of ≈ 6.5 for $q\bar{q} \to ZZ^{(*)}$and ≈ 2.5 for $gg \to ZZ^{(*)}$.

The distributions of the kinematics for the events that pass the selection criteria are shown at Figure 6.2 ,6.3 and 6.4.

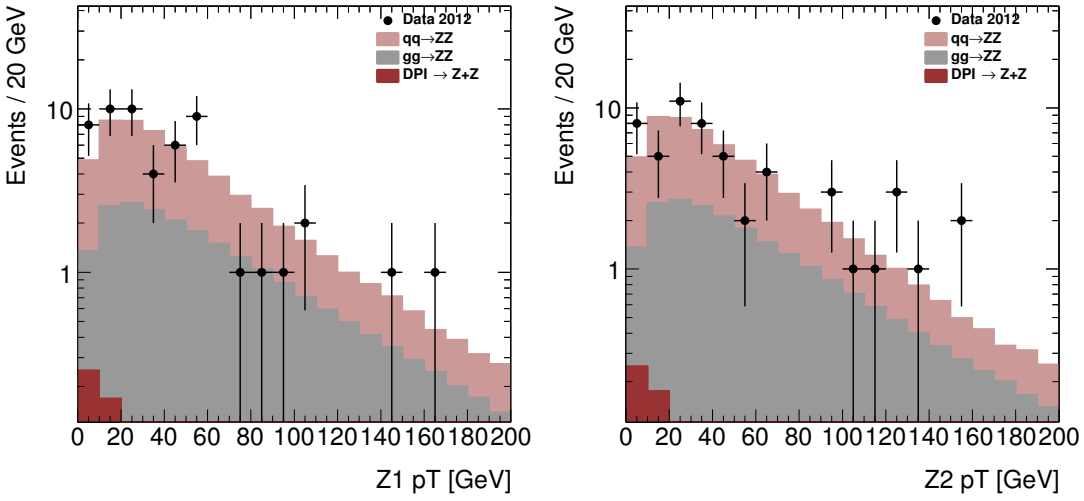

(a) Z1 p_{T}

(b) Z2 p_{T}

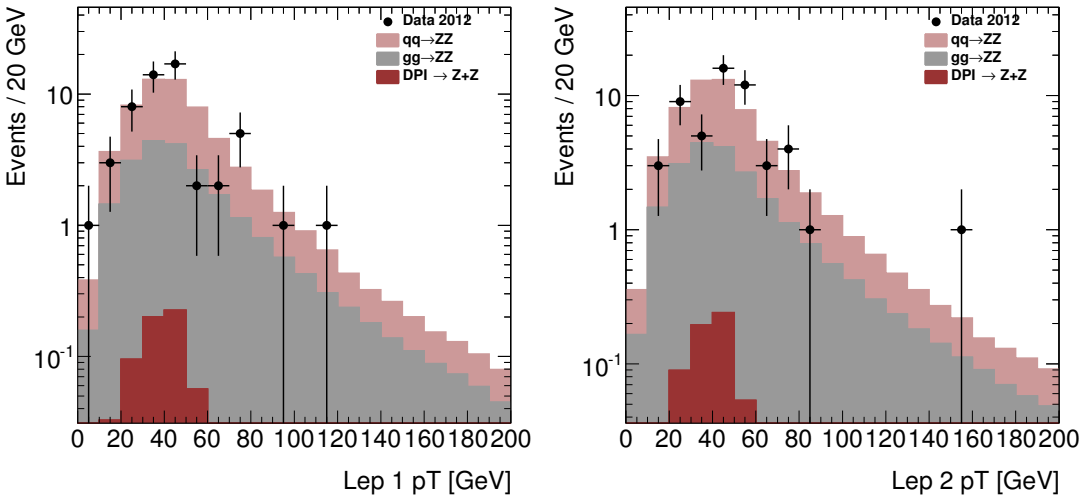

(c) Lepton 1 p_{T}

(d) Lepton 2 p_{T}

Figure 6.2: Distributions for the events passing the analysis cuts. (a) Leading dilepton pair (Z1) p_{T}, (b) Subleading dilepton pair (Z2) p_{T}, (c) p_{T} of the quadruplet lepton with highest p_{T}, (d) p_{T} of the quadruplet lepton with the second highest p_{T}. For the DPI sample σ_{eff} = 15mb is assumed. Reasonable agreement between data and MC is observed.

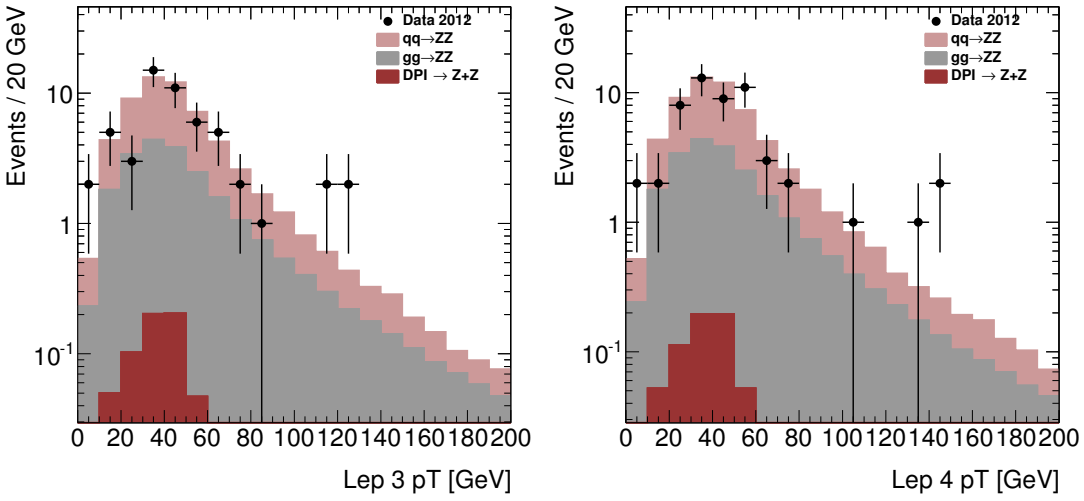

(a) Lepton 3 p_T

(b) Lepton 4 p_T

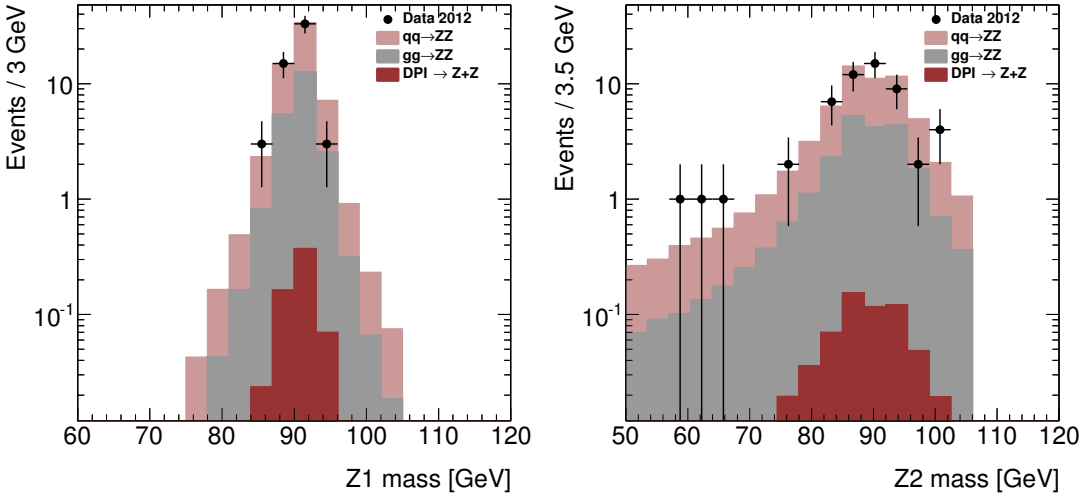

(c) Z1 mass

(d) Z2 mass

Figure 6.3: Distributions for the events passing the analysis cuts. (a) p_T of the quadruplet lepton with the third highest p_T, (b) p_T of the quadruplet lepton with smallest p_T, (c) Z1 mass, (d) Z2 mass. For the DPI sample σ_{eff} = 15mb is assumed. Reasonable agreement between data and MC is observed.

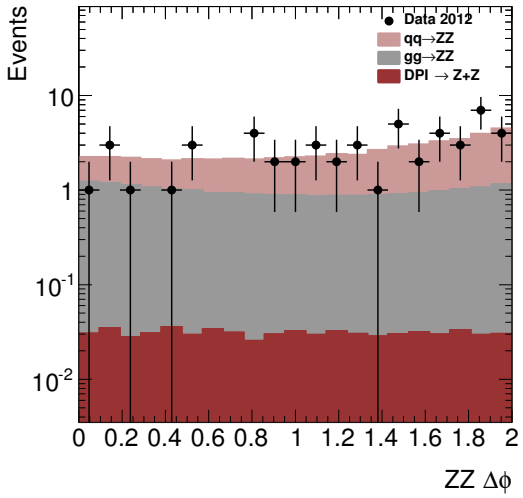

(a) ZZ $\Delta\phi$

Figure 6.4: Distribution of the observable $\Delta\phi$ for the signal and background events which pass the selection cuts. For the DPI sample σ_{eff} = 15mb is assumed. Reasonable agreement between data and MC is observed.

6.4.2 DPI observable

A Double Parton Interaction search with four leptons as final state needs an observable with very good discrimination power to drive the fit, due to the large background contamination from the ZZ continuum. An observable related to the particular event topology of the DPI in the transverse plane could be used as discriminant.

Based on the ATLAS W+2jets [31] analysis, the vectorial sum of the p_{T} for the 2 leptons originating from the Z boson is chosen. The vectorial sum is normalized to the scalar sum of the p_{T}. The mathematical expression of the observable is represented with the variable Δ.

$$\Delta = \frac{|\mathbf{p}_{\text{T}}^{\text{lep1}} + \mathbf{p}_{\text{T}}^{\text{lep2}}|}{|\mathbf{p}_{\text{T}}^{\text{lep1}}| + |\mathbf{p}_{\text{T}}^{\text{lep2}}|} \tag{6.2}$$

At the transverse plane, the Z boson is produced at rest. At a double interaction, each of the Z bosons will have zero p_{T} and subsequently the two leptons which will be produced after the decay will be back-to-back. On the other side, at the qq→ZZ and gg→ZZ background processes, the system of the two Z bosons will have a total zero p_{T}, whereas the produced leptons will not necessarily be back-to-back. Hence, considering only the leptons from the Z decays, the observable "$\boldsymbol{\Delta}$" will favour values closer to zero for Z produced through the Double Drell-Yan mechanism. A graphical represenation of the event topology, comparing SM ZZ and DPI Z+Z at the transverse plane, is shown in Figure 6.5.

Since the analysis involves the study of two Z bosons, the product of the observable Δ is used. A comparison of the observable distribution between the two Z from Double Drell-Yan

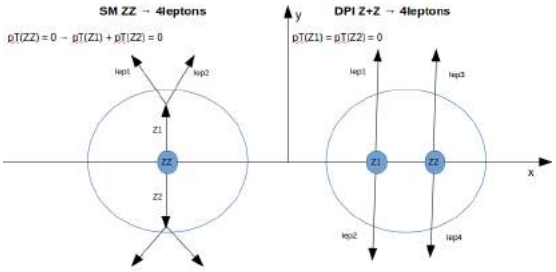

Figure 6.5: Event topology at the transverse plane, comparing the transverse energy p_T between the SM ZZ→4 leptons and DPI Z+Z→4 leptons.

and the background (single parton interaction), exhibits a stronger favour for values around zero, whereas the background has a broader shape. A represenation of the observable distribution for signal and background samples is shown in Figure 6.6.

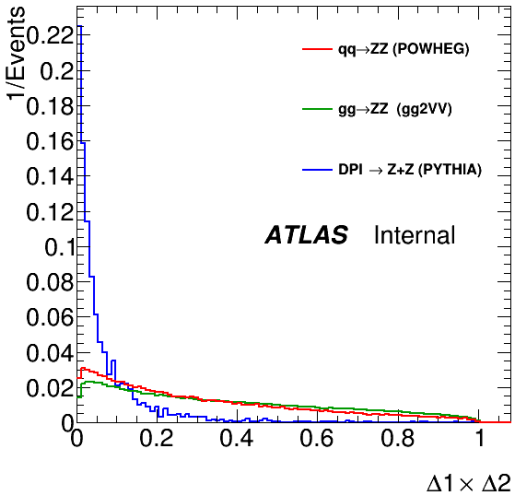

Figure 6.6: Shape of the observable $\Delta 1 \times \Delta 2$ for the signal and background events in the signal region, with the analysis channels combined. For the DPI sample σ_{eff} = 15 mb was assumed.

6.5 DPI cross section

6.5.1 DPI cross section definition

The present analysis measures the Double Drell-Yan cross-section, $\sigma_{\text{DPI}\to Z+Z\to 4l}$, where ($l = e, \mu$), in a fiducial region defined by the presence of two on-shell Z bosons, decaying to leptons with $p_T > 3$ GeV and $|\eta| < 5$. The measurement is bound to this fiducial phase-space due to

limitations on the generated signal sample.

The analysis is performed simultaneously in three channels (4e, 4μ, 2e2μ). The breakdown of the cross-sections and the relation with the σ_{eff} for each channel is presented below:

$$\begin{aligned}
\sigma_{\text{DPI}\to\text{Z+Z}\to 4e} &= \frac{1}{2}\frac{\sigma_{Z\to e^+e^-}\times\sigma_{Z\to e^+e^-}}{\sigma_{\text{eff}}} \\
\sigma_{\text{DPI}\to\text{Z+Z}\to 4\mu} &= \frac{1}{2}\frac{\sigma_{Z\to \mu^+\mu^-}\times\sigma_{Z\to \mu^+\mu^-}}{\sigma_{\text{eff}}} \\
\sigma_{\text{DPI}\to\text{Z+Z}\to 2e2\mu} &= \frac{\sigma_{Z\to e^+e^-}\times\sigma_{Z\to \mu^+\mu^-}}{\sigma_{\text{eff}}} \quad (2\text{ cases})
\end{aligned} \tag{6.3}$$

At the 2e2μ channel, $\sigma \times BR$ equals:

$$\sigma_{\text{DPI}\to\text{Z+Z}\to 2e2\mu} = 2\times\sigma_{\text{DPI}\to\text{Z+Z}\to 4e} = 2\times\sigma_{\text{DPI}\to\text{Z+Z}\to 4\mu} \tag{6.4}$$

Therefore the cross-section for the 2eμ channel can be associated with the exclusive cross-section as:

$$\begin{aligned}
\sigma_{\text{DPI}\to\text{Z+Z}\to 2e2\mu} &= 2\times\frac{1}{2}\times\frac{\sigma_{Z\to e^+e^-}\times\sigma_{Z\to e^+e^-}}{\sigma_{\text{eff}}} \\
&= 2\times\frac{1}{2}\times\frac{\sigma_{Z\to \mu^+\mu^-}\times\sigma_{Z\to \mu^+\mu^-}}{\sigma_{\text{eff}}} \\
&= 2\times\frac{1}{2}\times\frac{\sigma_{Z\to \mu^+\mu^-/e^+e^-}\times\sigma_{Z\to e^+e^-/\mu^+\mu^-}}{\sigma_{\text{eff}}}
\end{aligned} \tag{6.5}$$

The notation for the exclusive cross-section is:

$$\sigma_{\text{DPI}\to\text{Z+Z}\to 4l} = \frac{1}{2}\times\frac{\sigma_{Z\to\ell\ell}\times\sigma_{Z\to\ell\ell}}{\sigma_{\text{eff}}} \tag{6.6}$$

to denote the exclusive decay to each four leptons subchannel ($4e, 4\mu, 2e2\mu/2\mu2e$) where the analysis and simultaneous fit are performed.

The cross-section $\sigma_{Z\to\ell\ell}$ for the $Z\to\ell\ell$ process was calculated $\sigma_{\text{Z}} = 1.088 \pm 0.040$ fb where the branching ratio $\text{BR}_{Z\to\ell\ell} = 0.0336$ is included, with the MCFM 7.0 MC generator at $\sqrt{s} = 8$ TeV. It corresponds to the fiducial region where the Z bosons have a mass range of 50-106 GeV and the 2 leptons from the decay have $p_{\text{T}} > 3$ GeV and $|\eta| < 5$.

From the Eq.6.6 an expression for σ_{eff} can be extracted:

$$\begin{aligned}\sigma_{\text{eff}} &= \frac{1}{2} \times \frac{(\sigma_{Z\to\ell\ell}) \times (\sigma_{Z\to\ell\ell})}{\sigma_{\text{DPI}\to Z+Z\to 4\ell}} \\ &= \frac{1}{2} \times \frac{1.19 \times 10^{-12}}{\sigma_{\text{DPI}\to Z+Z\to 4l}\ (\text{fb}) \times 10^{-12}}\ \text{mb}\end{aligned} \tag{6.7}$$

6.5.2 Analysis acceptance

The analysis volume is the part of the phase-space which is close to the detector acceptance and it is applied on the MC signal. The selection criteria are selected to be similar to the experimental ones and are detailed on Table 6.2.

Table 6.2: Summary of the analysis acceptance selection requirements.

Lepton selection	
Electrons	$p_{\text{T}} > 7$ GeV $\lvert\eta\rvert < 2.47$
Muons	$p_{\text{T}} > 6$ GeV $\lvert\eta\rvert < 2.7$
Lepton pairing	
Primary pair	The di-lepton with mass closest to Z PDG mass.
Secondary pair	The next pair closest to Z PDG mass.
Quadruplet selection	
Lepton kinematics	$\text{Lep}_1\, p_{\text{T}}$ >20 GeV $\text{Lep}_2\, p_{\text{T}}$ >15 GeV $\text{Lep}_3\, p_{\text{T}}$ >10 GeV $\Delta R(l, l) > 0.1$ (0.2 for different flavour leptons)
DPI related cuts	
Mass requirement	$50 < m_Z < 106$ GeV
Azimuthal angle	$\Delta\Phi(Z1, Z2) < 2.1$
4-lepton mass window	$m_{4l} > 170$ GeV

The measured cross-section in the analysis volume should be extrapolated to the fiducial volume, which as it has been defined previously, consists of two on-shell Z bosons decaying to leptons with $p_{\text{T}} > 3$ GeV and $|\eta| < 5$. The extrapolation factor is referred as analysis acceptance $\mathbf{A_{Z+Z}}$.

$$A_{\text{Z+Z}} = \frac{N^{\text{MC}\to\text{Analysis Vol.}}_{\text{Gen. Z+Z}}}{N^{\text{MC}\to\text{Fiducial Vol.}}_{\text{Gen. Z+Z}}} \tag{6.8}$$

The extrapolation factor is defined as the ratio of the truth events which pass the analysis volume selection over the truth events in the fiducial volume. The calculation is obtained from

the "DPI signal" POWHEG + PYTHIA 8 MC sample. The acceptance is different for each of the three channels. The separate acceptances are summarized at Table 6.3.

Table 6.3: Summary of the analysis acceptance in truth level for each of the analysis channels with the total error included.

	4e	4μ	2e2μ
A_{Z+Z}	0.182 ± 0.006	0.238 ± 0.007	0.214 ± 0.006

The requirements for the on-shell Z candidates at the high mass regime with $\Delta\phi < 2.1$ are the main reason for the low acceptance numbers. The selection satisfies only a small fraction of the examined phase-space. Additionally, the different selection criteria between electrons and muons is the reason for the different numbers between the channels.

6.5.3 Analysis efficiency

The detector corrections and experimental inefficiencies are expressed by the analysis efficiency factor $\mathbf{C_{Z+Z}}$. The correction factor C_{Z+Z} is defined as the ratio of the MC events which pass the reconstruction level analysis over the MC generated events which pass the analysis volume selection.

The error of the C_{Z+Z} factor contains also all the previously described experimental systematic uncertainties, which are uncorrelated and included into the cross-section extraction. The values of the analysis efficiency for each channel are listed on Table 6.4.

$$C_{\mathrm{Z+Z}} = \frac{N^{\mathrm{MC\rightarrow Cuts}}_{\mathrm{Reco.\ Z+Z}} \times wt}{N^{\mathrm{MC\rightarrow Analysis\ Vol.}}_{\mathrm{Gen.\ Z+Z}}} \tag{6.9}$$

The fully reconstructed events are corrected with scale factors noted with "wt". These scale factors express: comparisons of lepton reconstruction efficiency between MC and data, tuning of lepton momentum scale and resolution in order to match the data.

Table 6.4: Summary of the fiducial acceptance in truth level for each of the analysis channels with the total error included.

	4e	4μ	2e2μ
C_{Z+Z}	0.514 ± 0.035	0.766 ± 0.035	0.678 ± 0.028

6.5.4 Expected yield

The number of signal events in the DPI-related region is given by:

$$N^{i}_{\text{events}} = L \times \sigma_{\text{DPI}\to Z+Z\to 4l} \times A_{Z+Z} \times C_{Z+Z} \tag{6.10}$$

The background expectation is derived after applying the full analysis chain at the reconstructed background samples and normalising the surviving events to 20.3 fb^{-1}. The expected and observed number of events for signal and background are listed on Table 6.5.

Channel	$q\bar{q} \to$ ZZ	gg$\to$ ZZ	DPI$\to$ Z+Z	Total Expected	Observed
4e	7.17 ± 0.57	4.17 ± 1.25	0.08 ± 0.01	12.59 ± 1.37	9
4μ	12.30 ± 0.98	6.61 ± 1.98	0.15 ± 0.01	19.06 ± 2.21	18
2e2μ	18.53 ± 1.48	10.51 ± 3.15	0.24 ± 0.01	29.28 ± 3.48	27

Table 6.5: Summary of the expected and observed number of events for signal and background. The theoretical uncertainty is included only in the background. For the DPI signal expectation, the σ_{eff} 15mb is assumed and only the statistical error is expressed.

Based on the distribution of the observable $\Delta 1 \times \Delta 2$, the majority of the DPI events are expected to populate the window 0 - 0.1. Table 6.6 presents the expected and observed events for the signal window. The number of background events at the sideband region ($\Delta 1 \times \Delta 2 > 0.1$) are listed on the Table 6.7.

Channel	$q\bar{q} \to$ ZZ	gg$\to$ ZZ	DPI$\to$ Z+Z	Observed
4e	2.29 ± 0.18	0.81 ± 0.24	0.06 ± 0.01	6
4μ	4.09 ± 0.33	1.33 ± 0.40	0.12 ± 0.01	5
2e2μ	6.26 ± 0.50	2.11 ± 0.63	0.16 ± 0.01	12

Table 6.6: Summary of the expected and observed number of events for signal ,assuming σ_{eff} 15mb, and background at the signal window $\Delta 1 \times \Delta 2$ <0.1. The theory uncertainty is included in the expected yield. For the DPI signal expectation, the σ_{eff} 15mb is assumed and only the statistical error is expressed.

Channel	$q\bar{q} \to$ ZZ	gg$\to$ ZZ	DPI$\to$ Z+Z	Observed
4e	4.88 ± 0.39	3.36 ± 1.01	0.02 ± 0.01	4
4μ	8.21 ± 0.66	5.28 ± 1.59	0.03 ± 0.01	12
2e2μ	12.57± 1.01	8.40 ± 2.52	0.08 ± 0.01	15

Table 6.7: Summary of the background and observed events at the sideband region $\Delta 1 \times \Delta 2$ >0.1. The theory uncertainty is included in the expected yield.

6.6 Systematic uncertainties

6.6.1 Theoretical uncertainties

The dominant systematic uncertainties in the analysis are the relative uncertainties originating from the background normalization. For the $q\bar{q}$ →ZZ process, the uncertainty is considered 8%. Similarly, for the gg→ ZZ the uncertainty is 30%. The values have been obtained from the LHC Higgs-Cross section working group.[88]

6.6.2 Experimental uncertainties

The contribution level of the experimental uncertainties is extracted by comparing the nominal expected MC events with the expected events, after varying the analysis with regard of a particular uncertainty. A summary of the experimental systematic uncertainties considered in the analysis is presented on Table 6.8. All of the values are found to be below 5%.

Table 6.8: Summary of experimental systematic uncertainties for signal yield per category which are considered for the cross-section measurement.

Nuisance parameter	4e	4μ	2e2μ
Electron reconstruction, identification and resolution efficiencies			
e energy scale	0.61 %	0	0.51 %
e momentum smearing	0.18%	0	0.09%
e resolution	1.07%	0	0.41%
e reco_id_eff	3.96%	0	2.02%
e isolation	0.33%	0	0.13%
Muon reconstruction, smearing and resolution efficiencies			
μ reconstruction	0	1.60%	0.81%
μ momentum smearing	0	0.42%	0.80%
μ energy scale	0	0.43%	0.36%

Summarizing all the systematic uncertainties, the largest at the electrons channel is the reconstruction and identification efficiency with a contribution of around 4% in the 4e channel and 2% at the 2e2μ channel. At the muons channel, the largest contribution originates from the reconstruction at the 4μ channel with 1.6% and the momentum smearing.

6.7 Statistical method

Having chosen the observable $\mathbf{\Lambda}$, the extraction of its shape for signal and background takes place. In both signal and background cases, the $\Delta 1 \times \Delta 2$ distribution is divided into 20 bins ranging from 0 to 1.

For the signal modelling, the shape is obtained with the application of the KEYS [89] algorithm. In every bin, the KEYS algorithm will generate a one-dimensional gaussian kernel. The width of the kernel is adaptively calculated from the local density of events, being narrow for areas with high density of events and broad for lower densities. This results in the removal of statistical fluctuations which might exist in the original shape. Lastly, the gaussian kernels are merged together with the application of a 3rd order interpolation, creating the smoothed PDF.

For the background, statistical fluctuations are not considered, due to the large statistics. The smoothed PDF is obtained straight from the MC and the 3rd order interpolation between the bins. The shapes for signal and background are shown in Figure 6.7.

The signal and the background shapes with the expected yields and the systematic uncertainties are combined to create the total model of the analysis. All the systematic uncertainties enter the final fit as constrained nuisance parameters. The number of the background events is constrained to the corresponding uncertainties and the number of Double Parton Interaction events is allowed to float.

An unbinned simultaneous fit is performed at the distribution of the observable for each of the 3 channels so that at the end a single value for the cross-section can be extracted by maximizing the combined profile likelihood. The full likelihood function with the nuisance parameters will automatically take into account all the systematic uncertainties, and propagate them to the final uncertainty of the parameters. The fit result is used then for an estimation of the $\sigma_{\mathbf{DPI\to Z+Z\to 4\ell}}$ and $\sigma_{\mathbf{eff}}$ values.

6.7.1 Validation test on MC

A closure test is performed in order to validate the fit model. The method involves fit on pseudo-data obtained by the signal and background MC events, normalized to the expected values with all the nuisance parameters at their best-fit value. This dataset is using asymptotic approximations equivalent to an infinite number of toy MC pseudoexperiments ("Asimov" dataset)[90]. Since the expected MC simulation yields were used to produce the model the fit should return the assumed values. Any deviation from these values would show biases on the model.

For the generation of the model, the $Z \to \ell\ell$ cross-section value of 1.088 ± 0.037 fb and σ_{eff} = 15 mb were used. The expected central value for $\sigma_{\text{DPI}\to Z+Z\to 4l}$ is 0.004 fb. Assuming the expected signal yield for σ_{eff} = 15 mb and fitting on the generated pseudodata, the fitted value for the cross-section is $\sigma_{\text{DPI}\to Z+Z\to 4l}$ = 0.040 ± 0.430 fb. The expected upper limit on cross-section is calculated $\sigma_{\text{DPI}\to Z+Z\to 4\ell} < 0.99$ fb which is translated to a lower limit on $\sigma_{\text{eff}} > 0.60$ mb.

The results show that the model is consistent overall and no biases exist in the fitting model.

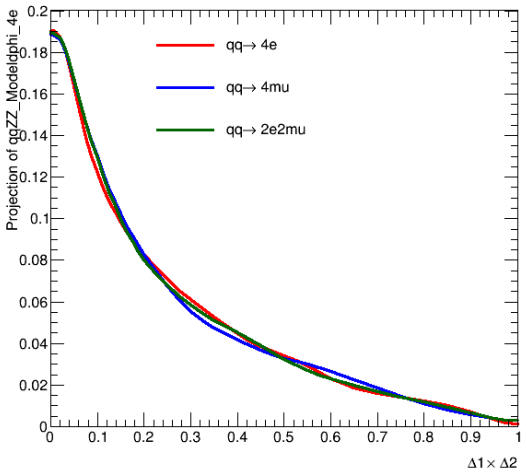

(a) $q\bar{q}$ →ZZ

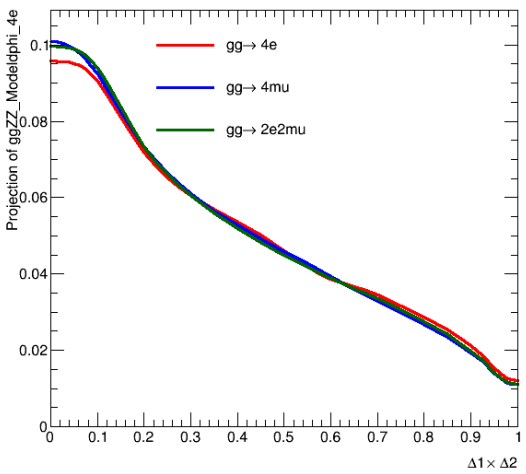

(b) gg→ZZ

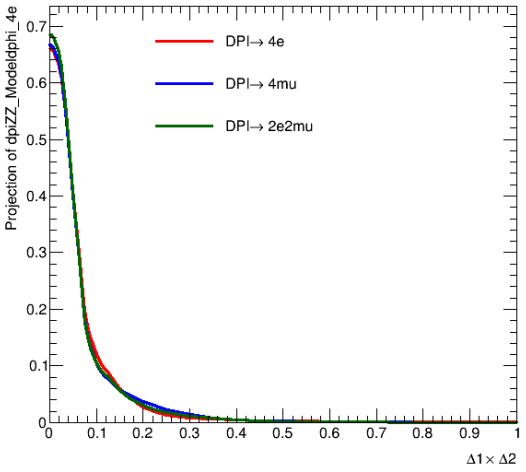

(c) DPI Z+Z

Figure 6.7: Distribution of the observable Δ for the signal and background events in the signal region for each analysis channel.

6.7.2 Nuisance parameter pulls

The effect of the systematic uncertainties has been studied with the calculation of the pull parameter, $\hat{\theta} - \theta_0/\Delta\theta_0$, where $\hat{\theta}$ is the best-fit value for the nuisance parameter, θ_0 is the starting value and $\Delta\theta_0$ is the uncertainty of the parameter. The pulls distribution is shown on Figure 6.8.

The background systematic uncertainties have been pulled down, compared to the expectation after the fit result with the $gg \rightarrow ZZ^{(*)}$having the largest negative pulls. The observed negative pulls are accounting for the observed event deficit in the background sidebands. Since there are no data to cover the sideband region, the fitted DPI cross-section would increase in order to balance, having though large relative uncertainties.

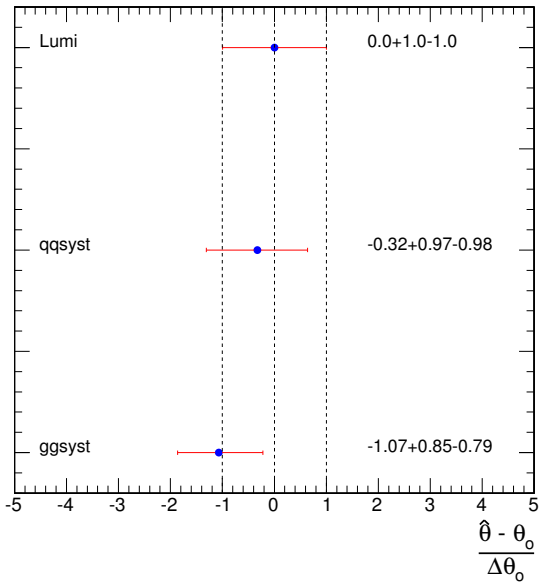

Figure 6.8: Nuisance parameter pulls for the background nuisance parameters and luminosity.

6.8 Results

The final step in the analysis is to perform the fit with the constructed model on the ATLAS data at the surviving events which pass all the analysis selection. A simultaneous fit is applied to all the 3 channels in order to extract a value for the fiducial $\sigma_{\mathrm{DPI}\to Z+Z\to 4l}$.

The best fit value for the exclusive cross-section is $\mathbf{0.74^{+0.51}_{-0.44}(stat.)^{+0.21}_{-0.14}(syst.)\ \ fb}$, leading to an upper limit for $\boldsymbol{\sigma_{\mathrm{DPI}\to Z+Z\to 4l} < 1.54\ \mathrm{fb}}$. The measured cross-section and limit, correspond to the fiducial volume defined by two Z bosons in the mass window (50 - 106 GeV) decaying to leptons with p_{T} >3 GeV and $|\eta| < 5$. The cross-section measurements for each indiviual channel and the exclusive are presented in Table 6.9.

The observable Δ for each analysis channel is shown in Figure 6.12. The result for the simultaneous fit and the individual fits on the channels are depicted in Figures 6.9 and 6.10. The comparison between the observed and the expected upper limit is shown on Figure 6.11.

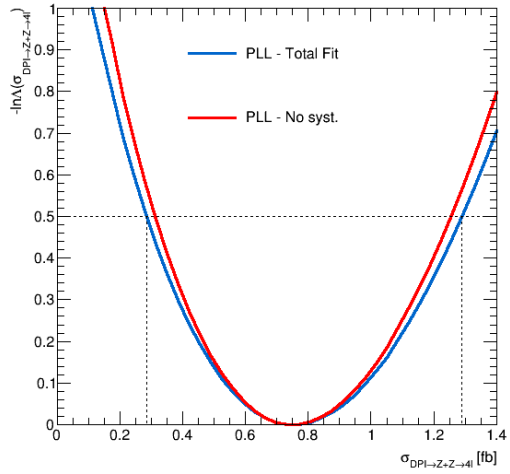

Figure 6.9: Distribution of the profile likelihood for the simultaneous fit (blue line) and the fit without systematics(red), with the 1σ (dashed line at 0.5) uncertainty range.

The $\sigma_{\mathrm{DPI}\to Z+Z\to 4l}$ limit can be translated into a lower limit for σ_{eff} , via the Equation 6.7, and was calculated $\boldsymbol{\sigma_{\mathrm{eff}} > 0.38\ \mathrm{mb}}$. The calculation of the limits was performed using the Modified Frequentist CLs method [91] at 95% confidence level, using the $\tilde{q}_{\mu}$ test statistic in the asymptotic approximation [90], which assumes a non-negative parameter of interest, which in this case is the exclusive cross-section.

The fitted cross-section is order of ten times higher than the expected one as extracted from the pseudodata fitting. In the fit result, the most dominant uncertainty is related to very limited statistics in data. The systematic uncertainty is of the order of $\approx$ 20% which is expected, due to the large uncertainty coming from the background normalization.

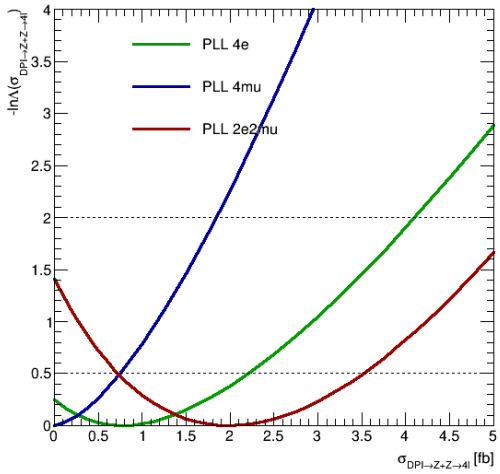

Figure 6.10: Distribution of the profile likelihoods for all the individual channels that are included in the fit with the 1σ (dashed line at 0.5) and 2σ (dashed line at 2) uncertainty range.

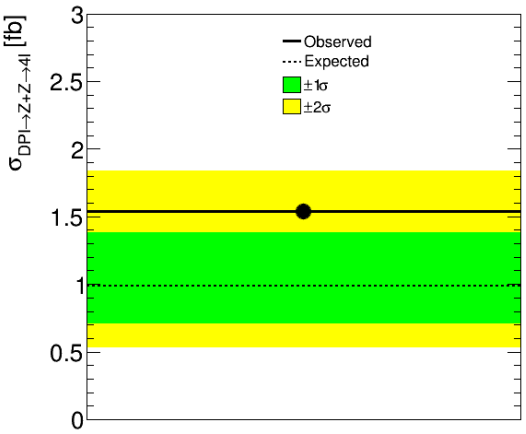

Figure 6.11: Upper limit on $\sigma_{\mathrm{DPI}\to\mathrm{Z+Z}\to 4\ell}$. The observed 95% CL (black) and the expected (dashed) limits are shown.

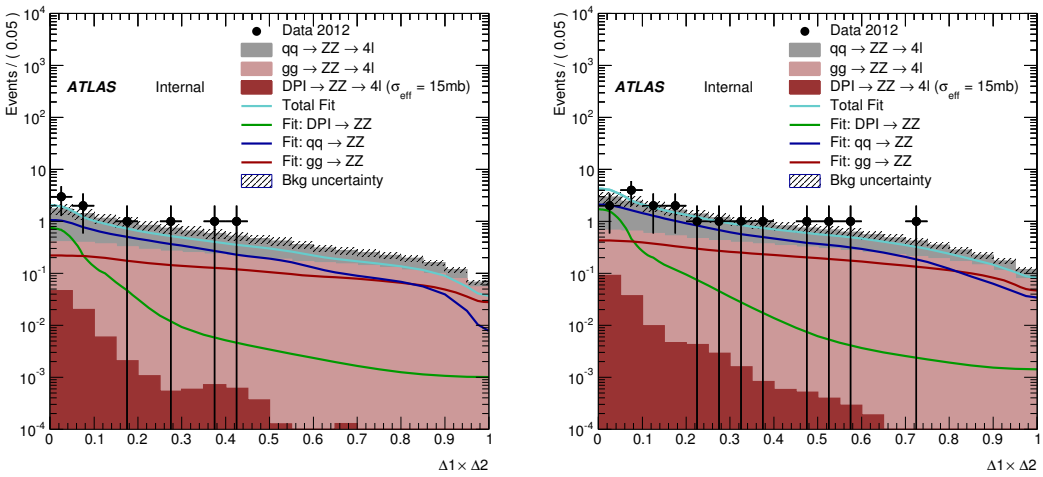

(a) 4e

(b) 4mu

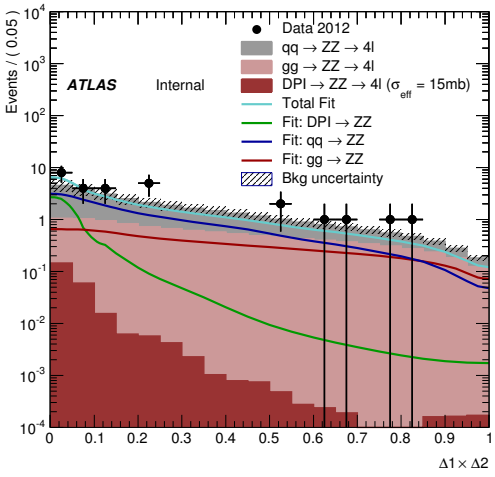

(c) 2e2mu

Figure 6.12: Distribution of the observable $\Delta 1 \times \Delta 2$ for the analysis channels. No significant excesses are observed on data.

Table 6.9: Fiducial cross-section measurements results for every analysis channel and the exclusive cross-section.

Cross-section measurements				
$\sigma_{\mathrm{DPI}\to Z+Z\to 4e}$	=	0.77	$^{+1.42}_{-0.00}$ (stat)	$^{+0.24}_{-0.17}$ (syst) fb
$\sigma_{\mathrm{DPI}\to Z+Z\to 4\mu}$	=	0.00	$^{+0.83}_{-0.00}$ (stat)	$^{+0.00}_{-0.00}$ (syst) fb
$\sigma_{\mathrm{DPI}\to Z+Z\to 2e2\mu}$	=	1.99	$^{+1.48}_{-1.22}$ (stat)	$^{+0.40}_{-0.33}$ (syst) fb
$\sigma_{\mathrm{DPI}\to Z+Z\to 4l}$	=	0.74	$^{+0.50}_{-0.44}$ (stat)	$^{+0.21}_{-0.14}$ (syst) fb

6.9 High luminosity study - Future prospects

The analysis prospects on $\sqrt{s}$ = 14 TeV for various luminosities are presented in this section. At higher luminosities, the signal to background ratio increases, since the scale for the signal expectation is higher than the background.

Based on the presented analysis method, both the number of expected events for signal and background are scaled up to 14 TeV. For the background processes ($q\bar{q}$ →ZZ and gg→ZZ), the cross-sections from 8 to 14 TeV increase by a factor of 2.1 [88, 92]. For the single $Z \to \ell\ell$ process, the projection of the cross-sections at 14 TeV was performed with the MCFM 7.0.1 MC generator and was found to increase by a factor of ≈ 1.81. A list of projected number of events for 300 and 1000 fb^{-1}is detailed on Table 6.10. Under the assumption of σ_{eff} = 15mb, the expected $\sigma_{\mathrm{DPI}\to Z+Z\to 4l}$, σ_{eff} and the corresponding upper and lower limits are shown in Figure 6.13.

Table 6.10: Projected number of events for signal and background at 14 TeV assuming σ_{eff} 15mb for indicative luminosities. The theoretical uncertainties are included.

Luminosity	Channel	$q\bar{q} \to$ ZZ	gg→ ZZ	DPI→ ZZ
300fb^{-1}	4e	222.52 ± 17.80	129.41 ± 38.82	3.61 ± 0.29
	4μ	381.72 ± 30.54	205.14 ± 61.54	7.04 ± 0.43
	2e2μ	584.38 ± 46.75	326.17 ± 97.85	11.20 ± 0.65
3000fb^{-1}	4e	2225.17 ± 178.01	1294.14 ± 388.24	36.10 ± 2.95
	4μ	3817.24 ± 305.38	2051.38 ± 615.41	70.35 ± 4.40
	2e2μ	5843.79 ± 467.50	3261.72 ± 978.52	111.98 ± 6.58

The fit results on the 14 TeV pseudodata show that the large uncertainties hinder a clear experimental observation for the Double Drell-Yan process at the LHC upgrade phases. How-

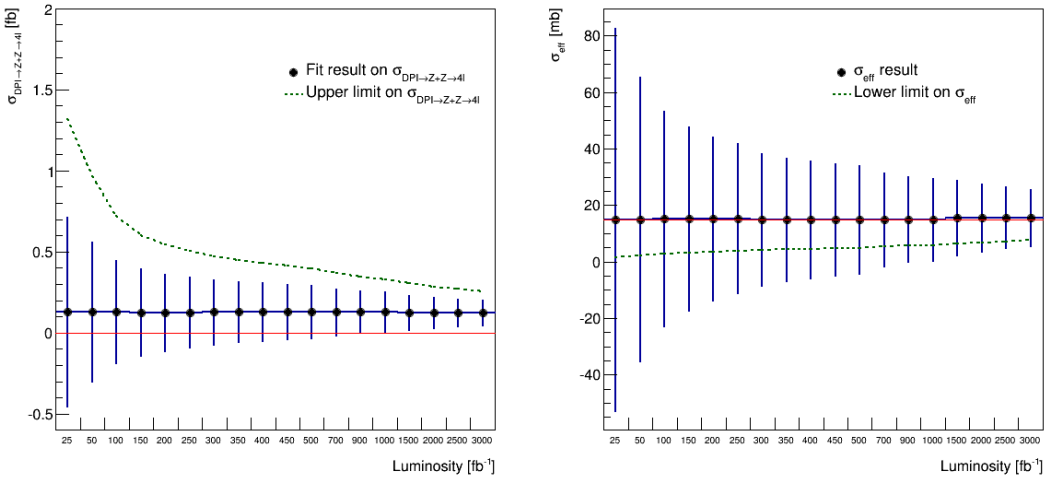

(a) $\sigma_{\text{DPI}\to Z+Z\to 4l}$ **(b)** σ_{eff}

Figure 6.13: Fit results and limits on $\sigma_{\text{DPI}\to Z+Z\to 4\ell}$ and σ_{eff} for various luminosities at 14 TeV. The red line in the DPI limit plot shows the value of 0 and at the σ_{eff} plot shows the value of 15.

ever, this conclusion is drawn upon on the assumption that the same σ_{eff} value contributes in the DDY, meaning that the factor σ_{eff} can express any Double Parton Interaction with a single value.

6.9.1 Study at universality of σ_{eff}

The universality of σ_{eff} has been challenged in the past, considering its validity in the Double Drell-Yan process. Phenomenological studies [37, 93] suggest that the transverse plane which describes the quark-antiquark initiated processes, like Double Drell-Yan, might have different properties compared to gluon-gluon initiated properties. The assumptions are based on two factors: a) the distribution of the partons in the interaction transverse plane, where the gluons are assumed to have broader distribution than quarks and b) the correlation with the momentum fraction of the scatters, meaning what part of the proton momentum is carried by the scatter.

The nature of σ_{eff} for this process ($q\bar{q}$) and its universality in general, is an open topic for QCD [37]. A Double Drell-Yan cross-section measurement with the presented analysis method in higher energies and luminosities would have an increased signal-over-background ratio and it would be able to examine the nature of σ_{eff} . In order to perform this test, the analysis is repeated with varied signal DPI yield, assuming other values of σ_{eff} (1 - 15mb). The significance as a function of luminosity for the various σ_{eff} assumptions is shown on Figure 6.14.

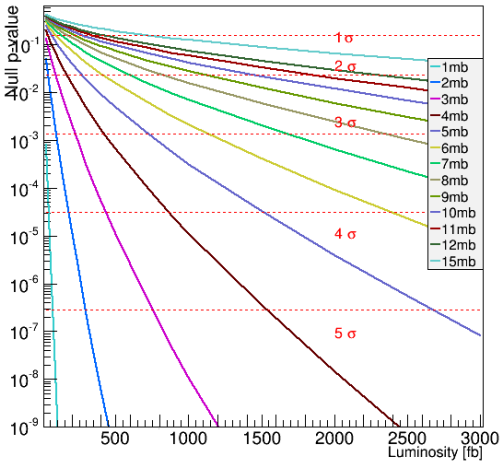

Figure 6.14: Local p-values of the background-only hypothesis testing for various luminosities. The significance of an observation of the Double-Drell Yann process increases with lower σ_{eff} values.

The distribution of the p-values indicates that if the σ_{eff} is indeed universal with the value of σ_{eff} = 15mb, then the significance of a future measurement would not be sufficient to provide strong evidence about DDY ($< 2\sigma$). However, assuming other lower values for σ_{eff} , then the significance of a future observation increases. If the σ_{eff} for DDY is at the level of 5 mb, a clear experimental measurement with significance of $> 3\sigma$ would be doable at the Run 4 of LHC (500fb^{-1}).

The designed HL-LHC will be able to reach the luminosity regimes for a clear experimental evidence if the σ_{eff} is below 10 mb. To illustrate this, Figure 6.15 shows the significance as a function of various σ_{eff} values for the luminosity value of 3000 fb^{-1}and is compared with 300fb^{-1}which are planned to be achieved in the near future by LHC.

The benefit from an experimentally clear observation of the DDY process would be the verification of the universality of σ_{eff} = 15 mb. An extra test is performed which seeks the luminosity regime where the universal value of 15mb could be excluded if, for DDY, σ_{eff} has a different value. For this calculation, a lower limit on the exclusive cross-section is obtained and translated to an upper limit on σ_{eff} , using the factorisation formula 6.1.

If the upper limit on σ_{eff} is found to be below 15 mb, then the value σ_{eff} = 15 mb could be excluded for the DDY process. Such a result would be an indication that σ_{eff} could have a different value for the DDY process. The results of this test are shown in Figure 6.16 and present the relation of the exclusion versus luminosity for various σ_{eff} assumptions. For the current LHC programme, up to 300fb^{-1}, the universality of the value σ_{eff} = 15 mb can be excluded for the DDY, if σ_{eff} has a real value below 4 mb.

The study of the DDY DPI $q\bar{q} \to ZZ \to \ell\ell\ell\ell$ process can exhibit alternative behaviour of

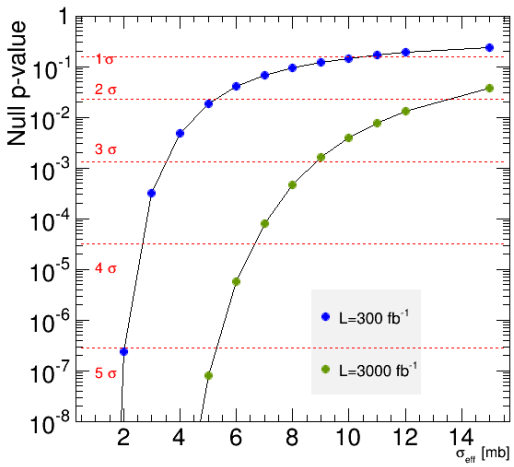

Figure 6.15: Significance of observation as a function of various σ_{eff} values for 300 and 3000 fb^{-1}. The significance of an observation of the Double-Drell Yann process increases with lower σ_{eff} values.

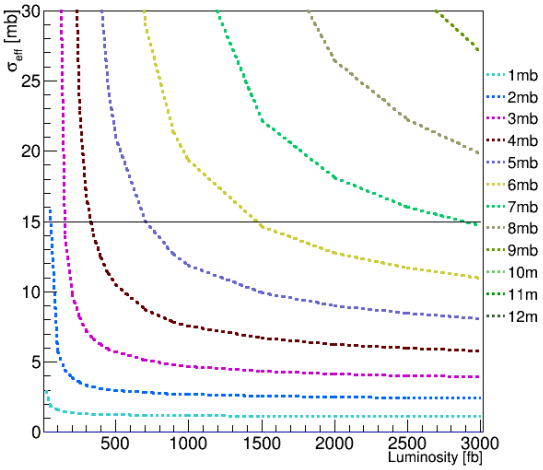

Figure 6.16: Upper limit on σ_{eff} for various σ_{eff} assumptions vs high luminosities range. An exclusion of the value σ_{eff} =15mb could be achieved if the upper limit on the assumed value of σ_{eff} is below 15mb (black line) for a given luminosity.

the hard scatters. It probes an initial state (quark-antiquark) which is different compared to other channels. A DDY DPI study can investigate the validity of the double Parton Distribution Functions expressions and assumptions about the factorisation of the longitudinal and transverse momentum components associated with the single Drell-Yan cross-sections. Lastly, the DDY cross-section measurement is important to understand background for other physics studies, like $H \to ZZ^{(*)} \to 4l$ or SUSY searches in the future of LHC.

6.10 Application in the low mass $H \to ZZ^{(*)} \to 4l$ analysis

The Double Drell-Yan process is a background for the $H \to ZZ^{(*)} \to 4l$ analysis. In order to have a better understanding of all the background sources in the signal region (120 - 130 GeV), the DPI contribtution should be calculated. The upper limit on the exclusive DDY cross-section could be used in order estimate the DPI contribution.

The measured $\sigma_{\mathrm{DPI}\to\mathrm{Z+Z}\to 4\ell}$ is related to two on-shell Z bosons decaying to leptons (electrons or muons with $p_{\mathrm{T}} > 3$ GeV at the region $|\eta| < 5$. The upper limit on the exclusive cross-section is 1.54 fb . Including an overall acceptance and efficiency factor of $A \times C \approx 0.15$, one obtains for 20.3 fb^{-1}an upper limit in DPI events of $N_{DPI\to Z+Z\to 4l} < 4.6$ in the DPI selection region ($m_{4l} > 170$ GeV, $50 < m_Z < 106$ GeV, $\Delta_\phi(ZZ) < 2.1$).

Appyling the $H \rightarrow ZZ^{(*)} \rightarrow 4l$ selection on the DPI MC sample, the ratio of the events which pass the DPI selection on top of the Higgs selection over those which pass only the Higgs selection is $\approx 0.40\%$. Extrapolating the previous limit to the Higgs analysis, one obtains $N_{DPI \rightarrow Z+Z \rightarrow 4l} < 11.48$ events for the full mass region.

From the DPI MC events that pass the Higgs analysis only a $\approx 0.08\%$ of the events lies in the signal mass window (120 - 130 GeV). Extrapolated to the signal region, the expected upper limit of DPI events in the low mass Higgs analysis is $N_{DPI \rightarrow Z+Z \rightarrow 4l} < 0.95$ events.

Chapter 7

Heavy Higgs boson search in the $H \to ZZ^{(*)} \to 4l$ decay channel

This chapter presents the search for an additional, heavy Higgs boson in the $H \to ZZ^{(*)} \to 4l$ channel. The events are categorised based on their production mode (gluon fusion, ggF-like and vector-boson fusion, VBF-like). The event rates are compared with the Monte Carlo background expectations for discrepancies and observation of data excesses. Due to the lack of evidence for new heavy Higgs states, 95% CL limits are set on the production cross-section times branching ratio.

The published analysis by ATLAS [87], performs a combined search on the H→ ZZ decay channels ($4\ell, 2\ell 2\nu, 2\ell 2q, 2\nu 2q$). The author was member of the $H \to ZZ^{(*)} \to 4l$ analysis team, responsible for the statistical interpretation and extraction of the cross-section limits, presented in Section 7.7.2.

7.1 Introduction

The search for an additional SM-like Higgs boson is important for physics extensions Beyond the Standard Model. As it has been described in Chapter 1 many SM extensions models, like the two-higgs-double model (2HDM [22]) predict the presence of an additional Higgs boson in parallel with the low mass SM one. The high mass regime, above 180 GeV, can be used to investigate the presence of an additional heavy Higgs. The signal to background ratio for the additional heavy Higgs is unknown and thus the properties of the SM Higgs boson using the $H \to ZZ^{(*)} \to 4l$ channel are used to in order to estimate an expectation.

In the present analysis, the search is performed for the mass range 140-1000 GeV, at the $H \to ZZ^{(*)} \to 4l$ ($l = e, \mu$) decay channel, excluding in this way any contribution from the on-shell $m_h = 125$ GeV. Assuming a SM-like additional heavy Higgs, the other ZZ channels ($2\ell 2\nu, 2\ell 2q$) are more sensitive in higher masses due to larger branching fractions, 1.35% and

4.7% respectively, compared to 0.452% [17] of the 4l channel. However, the four leptons channel has the clearest lepton reconstruction with small uncertainties.

7.2 Analysis synopsis

The analysis is based on an event selection where a sequence of requirements is applied, resulting in four well-reconstructed leptons (electrons or muons). Based on the production mechanisms of the low mass SM Higgs, the events which pass all the requirements are classified afterwards into four categories, following further selection.

The categorisation allows a search in a model independent way. Additionally, limits can be set on the production cross-section independently for the gluon-initiated process (ggF) and the quark initiated processes (VBF,VH). Since the Standard Model does not predict the existence of a heavy Higgs boson, there is no relative ratio for the cross sections of the various productions modes.

The variable with the highest discrimination power, similar to the low mass Higgs search, is the invariant mass of the four leptons system, which benefits from the performance of the ATLAS detector components (inner tracker, calorimeters and muon spectrometer).

An unbinned likelihood fit is performed in the invariant mass distribution. The parameter of interest for the fit is the quantity called signal strength, denoted as μ. It shows the ratio of the observed cross-section over a reference, which in this case is chosen to be the Standard Model cross-section. Finally, an upper limit on the μ is obtained, translated afterwards to cross-section times branching ratio upper limit.

7.2.1 Event and Object selection

The analysis follows the same selection as the low mass $H \rightarrow ZZ^{(*)} \rightarrow 4l$ analysis, which is described in Chapter 5. Additionally, there is a selection on the jets, since they are used for the classification of the events based on the assumed production mechanism. The jet reconstruction algorithm used is the anti-$k_{\perp}$ [60] with the choice of distance parameter R = 0.4. An extra requirement is applied, which removes jets coming from pile-up, and asks a minimum of 50% of the tracks associated to the jet, to originate from the primary vertex. Jets are required to have $p_{\mathrm{T}} > 25$ GeV for $|\eta| < 2.5$ and $p_{\mathrm{T}} > 30$ GeV for $2.5 < |\eta| < 4.5$. Furthermore, in order to ensure the quality, the standard "looser" ATLAS jets selection [61] is applied which takes into account spikes and noise in the calorimeters, rejecting thus fake jets.

7.2.2 Event categorisation

Following the formation of the four leptons candidate which passes the Higgs selection cuts, the event is classified into a production mechanism category. For the postulated additional heavy Higgs-like boson in a model independent search, there is no assumption about the

relative coupling strengths of the production mechanism. The categorisation would allow a handling of the relative strength of the production mechanisms. Similar to the low mass SM Higgs, the categories are "ggF-like", "VBF-like", "VH-like".

If the event initially satisfies the VBF criteria it is assigned to the VBF category, otherwise it is tested for either hadronic or leptonic VH criteria and assigned to the VH category. The remaining events are assigned to the ggF category. Figure 7.1 shows schematically the categorisation procedure:

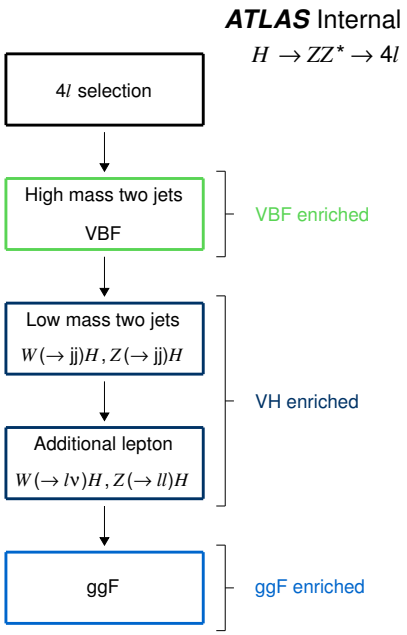

Figure 7.1: Schematic view of the event categorisation with the different selection for each category.

The breakdown of the categorisation is described below:

VBF selection

The VBF-like events are required to have at least two jets, accompanying the Higgs boson. The jets should pass the preselection criteria and the invariant mass of the di-jet system should be $m_{jj} > 130$ GeV. The selection has 55% efficiency which is constant among the full mass range. However, there is $\approx 10 - 30\%$ contamination from ggF events. In higher masses, as the ggF spectrum gets harder, there is an increase in the jet multiplicity and p_{T} of the jets and thus the event might mis-characterised as VBF.

VH selection

The VH-like events are those where a vector boson (W or Z) is produced alongside the Higgs Boson. The mechanism is known as "Higgs strahlung". The subcategorization of the event is based on the decay products of the vector boson which could be either hadronic or leptonic.

The hadronic-VH events are characterised by the presence of two jets whose invariant mass peaks either at the $m_W = 80.4$ GeV or $m_Z = 91.19$ GeV. The category is highly contaminated with ggF events though. In order to face the high rate of ggF events, the selection is using a Boost Decision Tree [94] to separate between Signal and Background-like events. A BDT score of 1 is assigned to signal-like events whereas for the background-like events the score is -1. The variables upon which the BDT was trained were: the invariant mass of the di-jet system, the pseudorapidity of the jet with the highest transverse momentum, the pseudorapidity separation of the two jets and the transverse momentum of the di-jet. Based on the tree outcome, the events are required to have a VH BDT score of -0.393. For example, applying this requirement for a Higgs boson at 300 GeV, the signal efficiency is 72% and the background rejection is 68%.

ggF selection

The gluon-gluon fusion is the most dominant production mechanism for a Standard Model Higgs boson, with a ratio of almost 8:1 to the VBF category. Looking for an additional heavy Higgs, it is assumed that ggF remains the main production mechanism. Having excluded thus all the other categories, all the remaining events in the selections, are categorised as ggF.

7.2.3 Background processes

The four lepton final state could originate from various background processes. Based on the similarity of the final state, there is the irreducible background (ZZ process) and the reducible background (any other process).

Irreducible background

The main source of the irreducible background in the $H \to ZZ^{(*)} \to 4l$ is in any mass range,

the Standard Model ZZ^* continuum production, where each of the Z bosons decay to leptons. Theory predicts that the process with the highest contribution is the $q\bar{q} \rightarrow ZZ^{(*)}$, whilst the $gg \rightarrow ZZ^{(*)}$process contributes around 10% [92]. Due to the different kinematics and theoretical systematic uncertainties, both processes are modelled separately on MC.

Reducible background

The reducible background comprises processes where the reconstructed lepton-pair furthest from the Z mass containing fake leptons from jets, or leptons from heavy-flavour quark semi-leptonic decays. Usually, such processes are Z+jets and $t\bar{t}$ decays. The reducible background is calculated using data-driven methods and it concerns mostly the sub-leading pair. Thus, two main categories of the reducible background exist: $\ell\ell\mu\mu$ and $\ell\ell$ee. Given the fact that a well-reconstructed lepton is less likely to be misidentified as jet, the contribution of the reducible background spans mainly the region below the ZZ threshold ($\approx$ 190 GeV) where one of the Z bosons is outside the mass peak.

7.3 Signal and background modelling

7.3.1 Background

In order to estimate the effect of the background in the analysis, all the background processes should be modelled through Monte Carlo simulation, with the application of all the necessary theory corrections.

7.3.1.1 Irreducible Background

$q\bar{q} \rightarrow ZZ^{(*)}$

The $q\bar{q} \rightarrow ZZ^{(*)}$background is modelled with the MC generator POWHEG, at Next-to-Leading Order in QCD. The factorisation (μ_F)and re-normalisation (μ_R) scale are fixed at $\mu_R = \mu_F = m_{zz}$, to account for non-pertubative PDF and UV divergences. The PDF CT10 NLO was used to for the description of the parton distributions in the colliding protons. For hadronization and showering, the MC generator PYTHIA 8 is used. Next-to-Next-to-Leading Order (NNLO) effects are included with the application of a factor ("k-factor") which is differential in the m_{zz} [95], increasing the cross-section in the high mass region by 4% compared to NLO. Also, the sample is re-weighted for NLO electroweak effects based on the kinematics of the di-boson system, following the recommendations of [96].

The $q\bar{q} \rightarrow ZZ^{(*)}$+ 2jets process, which is the electroweak background to VBF, is modelled with the MadGraph5 + Pythia 6 [97, 76] with scale $\mu_R = \mu_F = m_w$ and the PDF CTEQ611.Finally, all the detector effects, are modelled with the GEANT 4 toolkit.

$gg \to ZZ^{(*)}$

The $gg \to ZZ^{(*)}$background is modelled to Leading-Order accuracy using the MC generator MCFM, interfaced to PYTHIA 8 for hadronisation and showering. Since the LO $gg \to ZZ^{(*)}$process is part of the NNLO calculation for $pp \to ZZ^{*}$, the CT10 NNLO PDF is used. The discovered light Higgs boson at 125 GeV will affect the m_{4l} spectrum either at the low mass range through off-shell contributions, or through the interference of the processes $gg \to h \to ZZ^{*}$ and the SM $gg \to ZZ^{(*)}$. The MCFM generator accounts for the interference of the two processes. For NLO and NNLO QCD corrections, the k-factors applied on the $gg \to h \to ZZ^{*}$ process [98] are considered to have the same effect on $gg \to ZZ^{(*)}$. The GEANT 4 toolkit is used for the detector effects.

Considering the contribution of jets in this process, the LO MCFM simulation may not be accurate since hard emissions can be only generated in the parton shower. This leads to a non-accurate description of the acceptances. However, the SHERPA MC generator is capable of simulating the process with up to 1 jet included in the matrix element. With this approach, a LO accuracy is given at least to 1 jet and the acceptances of the jet-including categories are described better. Also, the same NNLO correction is applied to the SHERPA samples. Due to the low statistics of the SHERPA samples, the MCFM samples are used as nominal, scaling the ratio of events in each category, so as to match the ratios predicted by SHERPA.

7.3.1.2 Invariant mass shape for the background

For the shape description of the irreducible background, the $m_{4\ell}$ distribution is split into three parts. The low, medium and high part of $m_{4\ell}$. The statistical fluctuations are removed with use of the KEYS algorithm. In every part of the distribution, the gaussian kernel function uses a different width. The histogram produced in order to derive the smoothed shape has variable binning. The width of these bins is determined by width used on the KEYS kernel. This results into a finer binning in the area with higher statistics and broader binning in the lower statistics. Finally, a 3rd order interpolation is performed between the bins, to obtain the smoothed shape of the PDF describing $m_{4\ell}$.

An example of the aforementioned smoothing method is shown in Figure 7.2:

7.3.1.3 Reducible Background

As it has been mentioned on Chapter 5, the reducible background affects mainly the subleading Z which is the farthest from the Z pole. The background method is the same with the one used for the low Higgs mass measurement[67].

$\ell\ell\mu\mu$ background

In order to calculate the contribution of this background component, which is mainly fake jets from heavy-flavour semi-leptonic decays, a dedicated control region is created in the data.

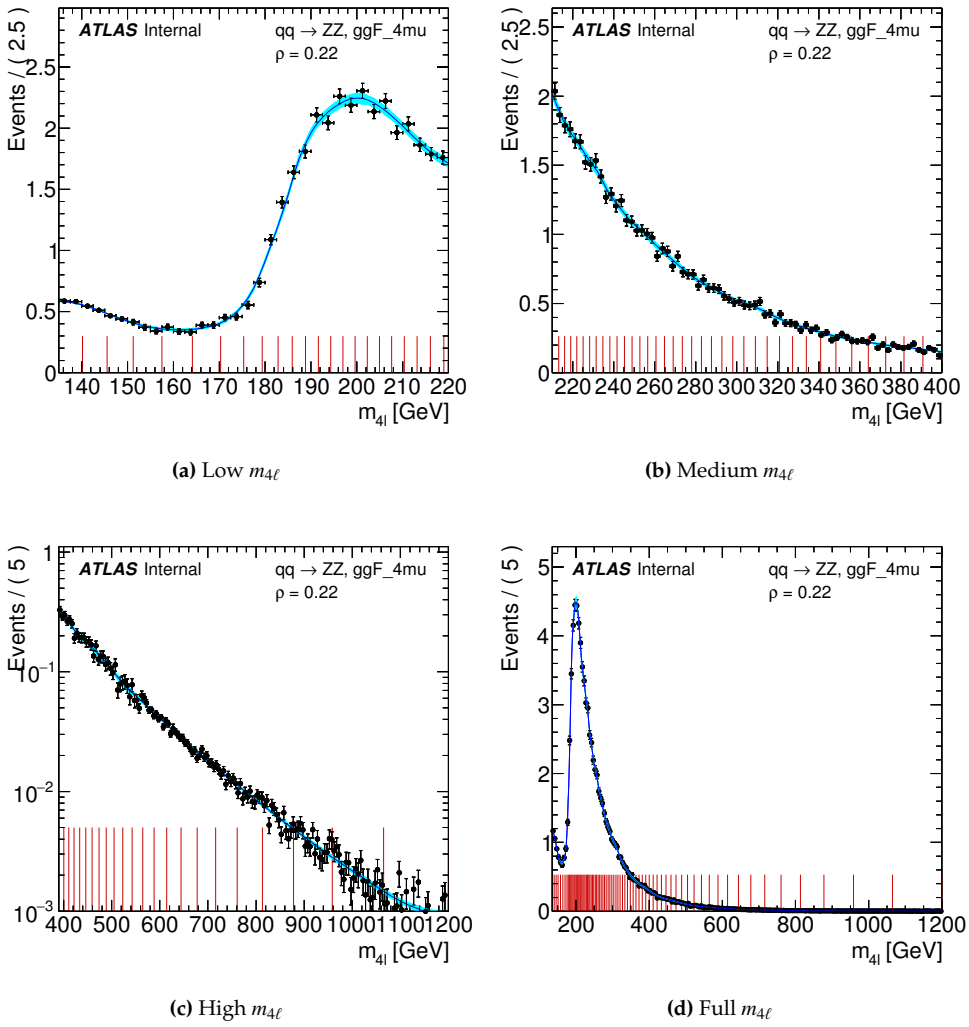

(a) Low $m_{4\ell}$

(b) Medium $m_{4\ell}$

(c) High $m_{4\ell}$

(d) Full $m_{4\ell}$

Figure 7.2: Smoothed PDF for the $q\bar{q} \rightarrow ZZ^{(*)}$ background in the ggF 4μ-like category, zoomed to different $m_{4\ell}$ regions. The blue band indicates the MC statistical uncertainty. The red lines show the new variable binning.

Given the proximity to jet behaviour on the events of these MC samples, all the cuts are applied, apart from the isolation and impact parameter cut. Inside this control region, four further control regions are defined and are fitted simultaneously, in order to extract the contribution of each sub-region to the main one. The number of events is calculated by the ratios from MC of the number of events in each sub-region to the number of events in the total region.

The sub-regions are:

1. One muon in the sub-leading pair with inverted impact parameter, enhancing the contribution from heavy flavour.

2. One muon in the sub-leading pair with inverted isolation cut, so as to increase the contribution from π or K decays.

3. Same-sign pair, where all the contributions are included.

4. A leading e-μ pair, with any sign sub-leading muon pair, so as to study the rest background components apart from Z+jets.

The fit results in the sub-regions are extrapolated to the main control region by multiplying them with the probability of each background component to pass the isolation and impact parameter cuts. The transfer factors contain systematic uncertainties which are low ($\approx$ 6%) for highly populated samples like $Zb\bar{b}$ and very high ($\approx$ 60%) for those with low statistics like Z+jets from light quarks. Also, the transfer efficiencies are validated with data using extra muons in $Z \to \ell\ell$ candidates. The comparison of the efficiencies between data and MC in the control region introduces an extra systematic uncertainty of 1.6%

$\ell\ell$ee background

The $\ell\ell$ee background mostly comprises fake electrons which are jets through either light-flavour hadrons, photon conversion and non-isolated electron from heavy-flavour hadronic decays.

The data driven method in this case, introduces a new control region, which requires the three leptons, with the highest transverse momentum, from which the third is an electron, to pass all the object requirements. The remaining fourth electron has a very relaxed electron identification requirement apart from a mininmum of seven silicon hits with at least one in the pixel detector. Also, the fourth electron should be of the same sign as the other one of the sub-leading Z candidates, in order to minimise the ZZ contribution.

The fit in this case is performed on the number of hits in the first pixel layer of the Inner Detector, and on the hit ratio of high to low-threshold on the Transition Radiation Tracker. The low threshold of 300 eV is used for registering the passage of minimum ionising particles, whereas the high threshold of 6 keV flags the absorption of transition radiation. The choice of these variables is based on the fact that most photons have no hits on the first pixel layer and the TRT threshold is able to distinguish between hadrons misidentified as electrons and the electrons from heavy flavour or photon conversions.

The yield given by the fit result is extrapolated to the signal region using efficiencies obtained from additional electrons in $Z \to \ell\ell$ decays which have loose selection. The uncertainties on these transfer factors are negligible since the samples contain large statistics.

Lastly, the fraction of events in every category is defined by simulation and is validated on data. These fractions are applied to the total background estimation and the number of events for each category is calculated, including the uncertainty due to data/MC comparison of the efficiencies.

PDF shape for $m_{4\ell}$

The shape of the $m_{4\ell}$ distribution is needed for the normalisation in the search regions. For the $\ell\ell\mu\mu$ background, the shape is obtained from simulation and the uncertainties are expressed by varying the requirements for track isolation and the impact parameter. For the $\ell\ell$ee background, the distribution of the control region is used after re-weighting in order to adapt to the kinematics of the signal region. The uncertainty is taken from the $m_{4\ell}$ distribution of other control regions, where the first two leptons should pass the full selection and the other two have the relaxed criteria. Figure 7.3 shows the smoothed $m_{4\ell}$ shapes for the two reducible background cases.

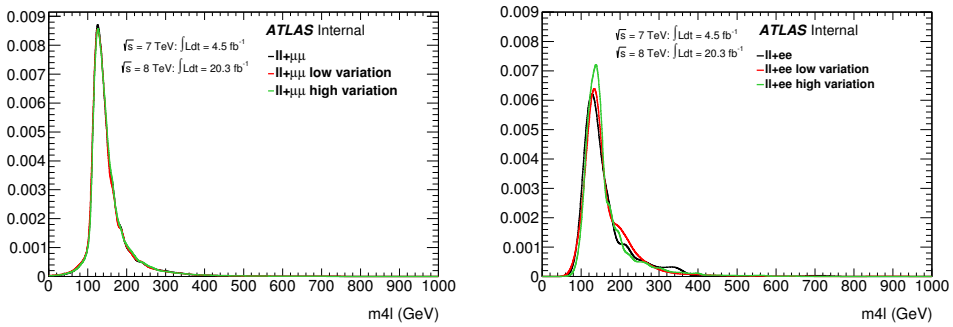

(a) $\ell\ell + \mu\mu$ **(b)** $\ell\ell + ee$

Figure 7.3: (a) The $m_{4\ell}$ distribution for the $\ell\ell + \mu\mu$ reducible background overlaid with two systematic variations (b) The expected $m_{4\ell}$ distribution of the reducible $\ell\ell + ee$ background, overlaid with systematic variations obtained by using different control regions.

The total background expectation before the fit for both irreducible and reducible is listed on Table 7.1

Process	ggF	VBF	VH
$q\bar{q} \rightarrow ZZ^{(*)}$	275.1 ± 18.9	14.64 ± 1.9	7.38 ± 1.04
$gg \rightarrow ZZ^{(*)}$	48.34 ± 40.7	4.9 ± 5.4	1.57 ± 1.7
$\ell\ell + \mu\mu$	4.60 ± 0.96	0.6 ± 0.6	0.15 ± 0.09
$\ell\ell$ + ee	2.87 ± 0.79	0.36 ± 0.42	0.19 ± 0.15

Table 7.1: The pre-fit expected background events in the mass range 135<$m_{4\ell}$<1200 GeV

7.4 Signal

The search is performed across a wide mass range in the $m_{4\ell}$. Therefore, a separate MC sample is needed for each m_H where the new signal might exist. The POWHEG MC generator is used for the modelling of the $H \rightarrow ZZ^{(*)} \rightarrow 4l$ signal , for the ggF and VBF production mech-

anisms, with matrix element up to NLO for all the mechanisms. Especially for the transverse momentum of the simulated Higgs boson, QCD corrections for NLO and NNLL are applied. The samples are interfaced to PYTHIA 8 for showering and hadronisation and to PHOTOS for QED radiative corrections which appear in the final state. In the case of the "Higgs strahlung" production, the signal is simulated with PYTHIA. All the detector effects are modelled with the GEANT 4 toolkit.

Up to m_H = 300 GeV the simulated additional heavy Higgs boson is modelled with the predicted SM width. For higher masses, the Narrow Width Approximation [23] is used which assumes a fixed width of 4.07 MeV for the Higgs in every mass point and a Breit-Wigner lineshape. The choice of the narrow width approach is suitable for the present search because any potential interference of a possible signal with the light Higgs and the ZZ background continuum is excluded. The various MC signal samples are detailed in Table 7.2.

Category	m_H (GeV)
ggF, VBF	140,150,160,170,180,190,200 220,240,260,280,300,320,340 360,380,400,420,440,460,480 500,520,540,560,580,600,650 700,750,800,850,900,950,1000
VH	140,145,150,160,165,170,175 180,185.190,195,200,220,240 260,280,300,320,340,360,380,400

Table 7.2: List of fully simulated signal MC for m_H

For every simulated signal mass point an $m_{4\ell}$ distribution is obtained. The statistical fluctuations on the shape are removed using the KEYS algorithm, following the same process with the variable binning and the 3rd order interpolation, as described on the irreducible background case. The final result is a smoothed PDF for every mass sample. At the mass points where signal samples do not exist, an interpolation [99] is performed using the shapes of samples on either side of mass point.

7.5 Acceptance

The signal acceptance is defined as ratio of the MC truth $H \to ZZ^{(*)} \to 4l$ events which pass all the selection and categorisation criteria, over all the generated MC $H \to ZZ^{(*)} \to 4l$ events. For the mass points where there is absence of signal MC, the acceptance is interpolated between yields from neighbouring samples. The acceptance is around 7% - 14% for each of the subchannels at the ggF category, around 30% for VBF and around 25% for VH, with a few % uncertainty. These acceptances are multiplied with the Standard Model Higgs cross section and branching ratio for the corresponding m_H to calculate an expected number of events as

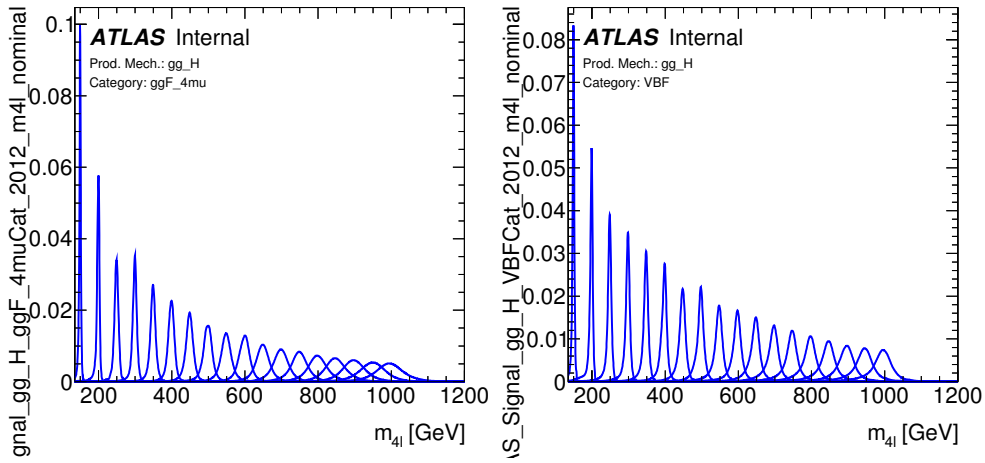

(a) ggF 4μ **(b)** VBF

Figure 7.4: Signal shapes as a function of m_H for the ggF and VBF production mechanisms. The pdf has unit normalisation.

input parameter for the fit. The expected signal yield for each category is shown on Figure 7.5

7.6 Systematic uncertainties

In the fit, for both signal and background, the experimental uncertainties are included as normalisation uncertainties, with a separate nuisance parameter for each. They are calculated separately for every mass point (m_H).

7.6.1 Signal uncertainties

For the signal samples, the uncertainties are evaluted by comparing the nominal expected event yield with the one regarding each uncertainty. An indicative table of the leading systematic uncertainties for a signal sample is shown in Table 7.4.

In figure 7.6 the most dominant signal normalisation uncertainties are shown as function of m_H of the simulated signal.

7.6.2 Background uncertainties

7.6.2.1 Irreducible background

The same experimental uncertainties affect also the irreducible background, $q\bar{q} \to ZZ^{(*)}$and $gg \to ZZ^{(*)}$. The most dominant uncertainties are listed on Table 7.3

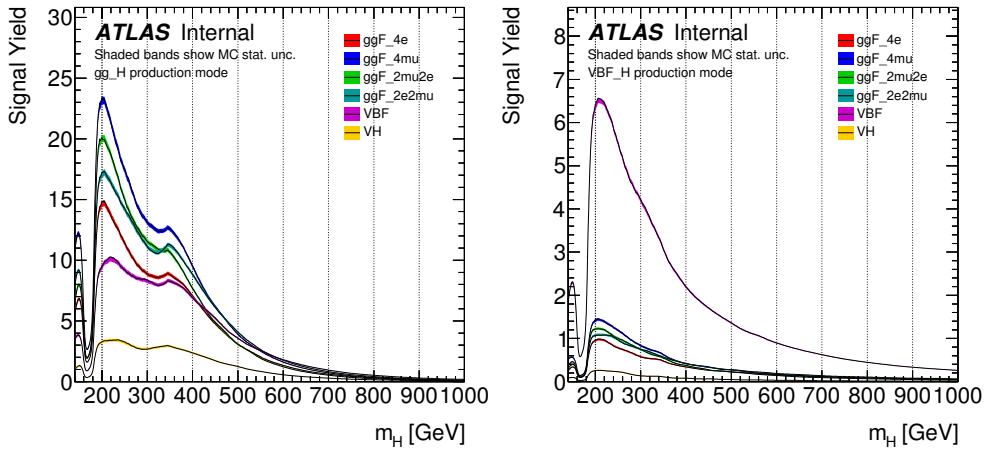

(a) ggF

(b) VBF

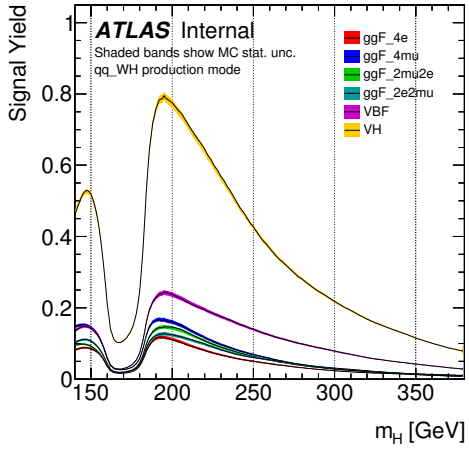

(c) WH

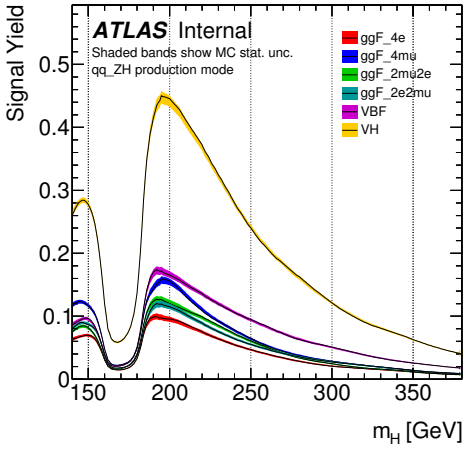

(d) ZH

Figure 7.5: Expected yields, assuming the SM cross sections and branching ratios, for the different production mechanisms and categories. The shaded band indicates the MC statistical uncertainty on the yield.

Table 7.3: Summary of experimental systematic uncertainties for the irreducible background. The maximum values for each category is stated.

Nuisance parameter	ggF	VBF	VH
el reco_id_eff	3.11%	1.28%	1.24%
μ reconstruction	1.66%	0.98%	1.02%
jet energy scale	0.28%	5.21%	3.12%

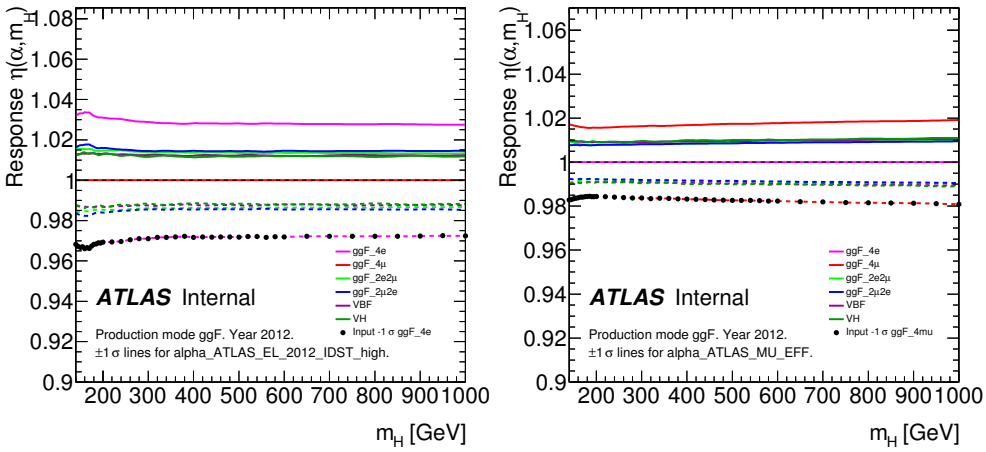

(a) el. id and reco.

(b) μ id and reco.

(c) Jet energy scale - flavour comp.

(d) Jet energy- eta modelling

Figure 7.6: Signal normalisation uncertainties as a function of m_H, expressed as a scale-factor applied to the nominal signal yield, for the uncertainties with highest effect. (a) electron identification, (b) muon efficiency, (c) jet flavour component, (d) jet eta model.

Table 7.4: Summary of experimental systematic uncertainties for a simulated signal samples on m_H = 400 GeV. The maximum values for each category are stated.

Nuisance parameter	ggF	VBF	VH
el reco_id_eff	2.97%	1.28%	1.24%
μ reconstruction	1.63%	0.91%	0.96%
jet energy scale	1.90%	5.40%	5.08%

7.6.2.2 Reducible background

For the reducible background, the normalisation uncertainties arise mainly from the different data-driven methods, the comparisons between MC generators, and the relative uncertainties on the transfer factors from control to signal region and the significantly from limited statistics. The total uncertainties of each category of the background are listed on Table 7.5.

Table 7.5: Summary of experimental systematic uncertainties for the reducible background. The value incorporates all the relevant uncertainties.

Background	ggF	VBF	VH
$\ell\ell + \mu\mu$	33%	94%	63%
$\ell\ell + ee$	24%	117%	113%

7.6.3 Theory Uncertainties

7.6.3.1 Signal model

For the acceptance of the signal model, the uncertainties are related to the modelling of the Higgs boson production. The variation of the generation parameters results in the corresponding theory uncertainty. Three variations are considered: 1) Varying up and down by a factor of two the QCD re-normalisation and factorisation scales. 2) Decreasing and increasing the amount of initial state radiation (ISR) and final state radiation (FSR) for jet emission. 3) Replacing the nominal PDF (CT10) with other PDFs. The summary of the signal theory uncertainties is listed on Table 7.6

Source	ggF MC production			VBF MC production		
	ggF-like	VBF-like	VH-like	ggF-like	VBF-like	VH-like
QCD scale	0.7%	1%	1%	1%	1%	2%
PDF	2%	2%	2.5%	1%	0.5%	2%
ISR/FSR	2-5%	7-10%	4-7%	1-2%	0.5-2%	1-5%

Table 7.6: Signal theory acceptance uncertainties applied on the full m_H range.

7.6.3.2 Underlying event

The acceptance of the categories is sensitive to the modelling of the underlying event and multiple parton interactions (MPI). For the calculation of this particular uncertainty, a $Z \to \mu^+\mu^-$ sample is used, with MPI either allowed or not, and then subjected to categorisation. The difference in truth level, after correcting detector defects, is considered as the systematic uncertainty. This approach yields an uncertainty of 6.6% for ggF events in the VBF category and 7.5% in the VH category. For VBF events, the uncertainty is 1.4% and 3.1% for VBF-like events in the VH category.

7.6.3.3 Background model

The uncertainties of the PDF and α_S on the background normalisation are applied as function of $m_{4\ell}$[88], and they yield 3% for $q\bar{q} \to ZZ^{(*)}$and 8% for $gg \to ZZ^{(*)}$. Additionally, the variation of the factorisation and re-normalisation QCD scales at the $q\bar{q} \to ZZ^{(*)}$background introduces an extra 4% normalisation uncertainty, affecting the acceptance of each category with 4% in ggF, 8% in VBF and 3% in VH. Lastly, when both Z bosons are on-shell, electroweak NLO corrections should be applied, introducing an uncertainty of 0.5% for ggF, 2.6% for VBF and 1.9% for VH.

For the $gg \to ZZ^{(*)}$background and the interference with the off-shell $gg \to h^* \to ZZ^*$ process, no higher-order QCD calculations exist. It has been shown [100] that higher-order

corrections affect $gg \rightarrow WW$ and $gg \rightarrow h^* \rightarrow WW$ similarly, within a 30% uncertainty on the interference term. This yields 60% uncertainty on the $gg \rightarrow WW$ and the same conclusion can be inferred for the ZZ^* state [100]. The gg-induced part of the off-shell light Higgs boson k-factor [101] can be applied to the $gg \rightarrow ZZ^{(*)}$background. The uncertainty of the k-factor depends on the ZZ^* invariant mass and is around 30%. Similar to WW case, the k-factor would introduce a 60% uncertainty in the $gg \rightarrow ZZ^{(*)}$process. However, for this analysis, an additional uncertainty of 100% is assigned to the $gg \rightarrow ZZ^{(*)}$background to cover the unknown validity of the uncertainties introduced by the k-factor.

The acceptance uncertainty of the categories for the $gg \rightarrow ZZ^{(*)}$background process is estimated by variation of the parton shower settings. Based on their different parton shower model, the difference in the acceptances calculated with SHERPA and MCFM is 92% for VBF, 91% for VH and 14% for ggF. Such large differences in the categories which contain jets are expected based on the different description of the jets, as it has been detailed previously.

All the theory uncertainties for the background, are summarised on the Table 7.7:

Background process	Category	PDF+α_S	QCD scale	Acceptance	NLO EW correction
$q\bar{q} \rightarrow ZZ$	ggF	3 %	4 %	4 %	0.5 %
	VBF	3 %	4 %	8 %	2.6 %
	VH	3 %	4 %	3 %	1.9 %
$gg \rightarrow ZZ$	ggF	8 %	100 %	14 %	-
	VBF	8 %	100 %	92 %	-
	VH	8 %	100 %	91 %	-

Table 7.7: Summary of theoretical normalisation uncertainties for the $q\bar{q} \rightarrow ZZ^{(*)}$ and $gg \rightarrow ZZ^{(*)}$ backgrounds: PDF+α_S, QCD scale, Acceptance and NLO Electroweak corrections.

7.7 Statistical treatment

The search for an additional Higgs boson is performed with an unbinned profile likelihood simultaneous fit on the four-leptons invariant mass distribution. The likelihood function comprises the product of a probability for observing n events, expressed through a Poisson term, with a weighted sum of signal and background PDFs calculated at all observed events. The equation for the likelihood function is given below:

$$\mathcal{L}(x_1..x_n|\mu) = \text{Pois}(n|\mu S + B)\left[\prod_{e=1}^{n} \frac{\mu S\, f_S(x_e) + B f_B(x_e)}{\mu S + B}\right] \tag{7.1}$$

In the likelihood equation, the terms f_s and f_b refer to the $m_{4\ell}$ PDF for signal and background, where for signal it depends only on the particular m_H. The term μ, which is the parameter of interest in the fit, is the signal strength showing the ratio of observed events to the

Standard Model expectation, defined as:

$$\mu = \frac{\sigma \times BR}{\sigma_{SM} \times BR_{SM}} \tag{7.2}$$

Both the signal and background models are described by the full set of nuisance parameters (θ_i). In all the nuisance parameters, gaussian constraints are applied based on their nominal values and uncertainties. Additionally, uncertainties from the overall normalisation and shape of the PDFs originating from the limited MC statistics are included into the fit for signal and background models. The variable binning, which was used based on the gaussian kernel, provides less statistical uncertainties to the PDF, independent to each other and between every bin.

The likelihood function therefore is a function of three parameters. The signal strength μ, the mass point m_H and the nuisance parameters θ_i. The best-fit value for each mass point is obtained by setting the m_H constant at the mass point, and obtain the values of μ and θ_i which maximise the likelihood function.

For each of the six categories of the search (VBF, VH, $ggF \rightarrow H \rightarrow 4\mu$, $ggF \rightarrow H \rightarrow 4e$, $ggF \rightarrow H \rightarrow 2\mu 2e$ and $ggF \rightarrow H \rightarrow 2e2\mu$), separate signal and background models are used, which enter the simultaneous fit. After the fit, the VBF and VH are treated as single category, with a single signal strength parameter μ_{VBFVH}.

7.7.1 Fit results

The best-fit values for the signal strengths of both categories are obtained in the full m_H range. Both signal strengths are considered as free parameters in the fit, greater than zero, in order to avoid nonphysical results due to the lack of events. Table 7.8 shows the results on the signal strength. As expected, all the results are comparable with zero within the uncertainties.

Secondary, the fit is performed on the background, forcing the signal strength values for ggF and VBF+VH to be zero. The pre- and post-fit results on the background are summarised on Table 7.9. In the ggF channel, after the fit there is a slight deficit in the background compared to the original expectation within 1-sigma uncertainty. This fluctuatation of the background is responsible for the excess observed in the ggF channel. Overall, the total background yield is reduced by approximately 4% with a significantly lower uncertainty due to the fit constrains of the large theory uncertainties.

Figure 7.7 shows the post-fit plots in the ggF,VBF and VH categories for $m_H = 200$ GeV. For each category, the shown signal is scaled to a cross-section corresponding to five times the observed cross section limit for the category. The irreducible background is normalised to the expectation and the reducible background is scaled to the data-driven calculation.

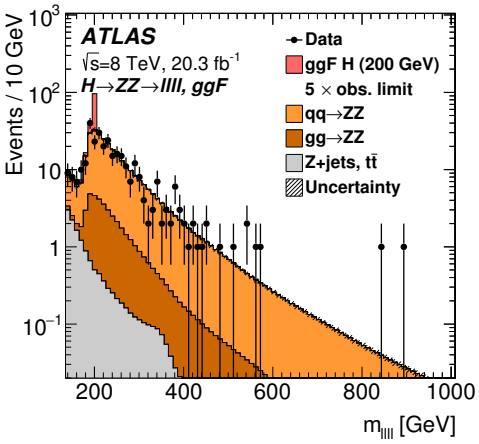

(a) ggF

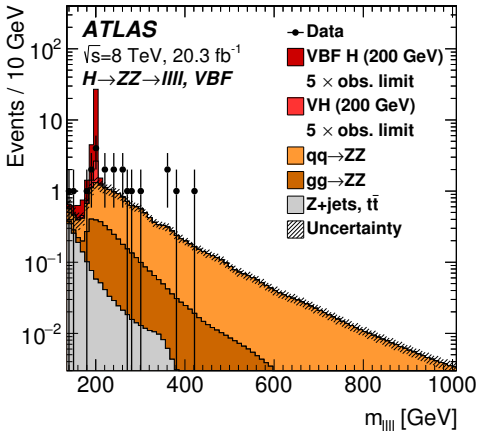

(b) VBF

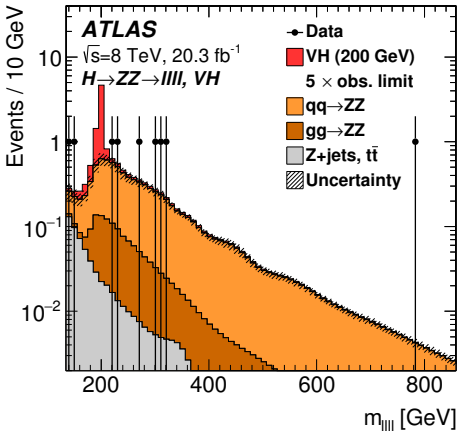

(c) VH

Figure 7.7: Post-fit $m_{4\ell}$ distributions for $m_H = 200$ GeV for the, (a) ggF, (b) VBF and (c) VH categories. The expected signal for each category is normalised to a cross-section corresponding to five times the observed limit. No significant excess from the expected background is observed.

m_H [GeV]	$\hat{\mu}_{ggF}$	$\hat{\mu}_{VBF}$
150	0.00±0.15	0.54±0.56
200	0.00±0.07	0.35±0.29
250	0.00±0.04	0.00±0.16
300	0.06±0.09	0.00±0.47
350	0.00±0.03	0.00±0.21
400	0.00±0.05	0.00±0.41
450	0.00±0.13	0.00±0.38
500	0.00±0.04	0.00±0.25
550	0.11±0.15	0.00±0.61
600	0.00±0.08	0.00±0.36
650	0.00±0.09	0.00±0.39
700	0.00±0.13	0.00±0.46
750	0.00±0.35	0.00±0.65
800	0.55±0.68	0.00±0.94
850	0.60±0.93	0.00±1.68
900	1.22±1.29	0.00±2.45
950	0.00±0.96	0.00±1.17
1000	0.00±0.92	0.00±1.12

Table 7.8: Best-fit μ values observed in data in a fit where both μ_{ggF} and μ_{VBF} are free in the fit and are required to be ≥ 0.

	Pre-fit				
Channel	$q\bar{q} \to ZZ^{(*)}$	$gg \to ZZ^{(*)}$	Reducible	Total	Observed
ggF $4e$	52.5 ± 3.8	9.6 ± 8.1	2.5 ± 0.6	64.6 ± 8.6	56
ggF 4μ	88.1 ± 6.0	14.9 ± 12.5	3.6 ± 1.2	106.6 ± 13.2	92
ggF $2e2\mu$	64.9 ± 4.4	11.3 ± 9.6	3.1 ± 1.0	79.3 ± 10.0	98
ggF $2\mu2e$	69.6 ± 4.7	12.5 ± 10.5	2.6 ± 0.6	84.6 ± 11.0	70
All ggF	275 ± 18.8	48.3 ± 40.7	11.8 ± 2.5	335.1 ± 42.5	316
VBF	14.6 ± 1.9	4.9 ± 5.4	1.1 ± 0.8	20.7 ± 5.9	22
VH	7.38 ± 1.04	1.6 ± 1.7	0.5 ± 0.3	9.4 ± 2.1	9
All 4l	297 ± 19.8	54.8 ± 45.6	13.3 ± 3.5	365.2 ± 47.2	347
	Post-fit				
Channel	$q\bar{q} \to ZZ^{(*)}$	$gg \to ZZ^{(*)}$	Reducible	Total	Observed
ggF $4e$	51.2 ± 3.1	7.9 ± 3.5	2.6 ± 0.5	61.7 ± 3.3	56
ggF 4μ	85.8 ± 4.8	12.2 ± 5.4	4.3 ± 1.4	102.4 ± 5.0	92
ggF $2e2\mu$	63.3 ± 3.5	9.3 ± 4.1	3.7 ± 1.1	76.3 ± 3.7	98
ggF $2\mu2e$	67.9 ± 3.8	10.3 ± 4.5	2.7 ± 0.5	80.8 ± 4.0	70
All ggF	268.2 ± 14.9	39.8 ± 17.4	13.3 ± 2.6	321.2 ± 15.3	316
VBF	14.1 ± 1.6	5.1 ± 3.3	1.5 ± 0.9	20.7 ± 3.3	22
VH	7.1 ± 0.9	1.6 ± 1.0	0.6 ± 0.3	9.3 ± 1.2	9
All 4l	289.3 ± 16.0	46.5 ± 19.4	15.4 ± 3.7	351.2 ± 16.6	347

Table 7.9: Expected background yields after the fit. The signal strength for both ggF and VBF are set to zero and only the backgrounds are included in the fit. The uncertainties correspond only to systematic ones while the statistical uncertainties are negligible.

7.7.2 Limit setting

Given the absence of excesses in the mass search, upper limits are set on the production cross-section times branching ratio for a heavy Higgs. The relative ratio of ggF to VBF+VH production is unknown so the limits are independent of model assumptions. In addition, when setting limits on a particular signal strength, the signal strength of the "other" category is a free parameter. Furthermore, since the parameter of interest is the signal strength, the upper limits are multiplied with the SM cross-section times branching ratio to cancel out their presence in the signal strength, and obtain SM-independent limits.

The limits are computed with using the modified frequentist method [91] at 95% confidence level, with the use of the $\tilde{q}_\mu$ test statistic in the asymptotic approximation ("Asimov" dataset) [90]. The expected limit is extracted from a representative dataset which contains the median expectation of the result with the expected statistical variation.

In the generation of the dataset for the background-only hypothesis, the signal strength for both ggF and VBF production takes a zero value and the nuisance parameters take the best-fit values, which maximise the likelihood on the observed data. For the calculation of the observed limit, prior to the generation of the background only dataset, the cross-section of the production mechanism which is not being tested is set to best-fit value from the observed data.

The limits are presented on Figure 7.8. No significant variation are observed compared with the background-only expectations.

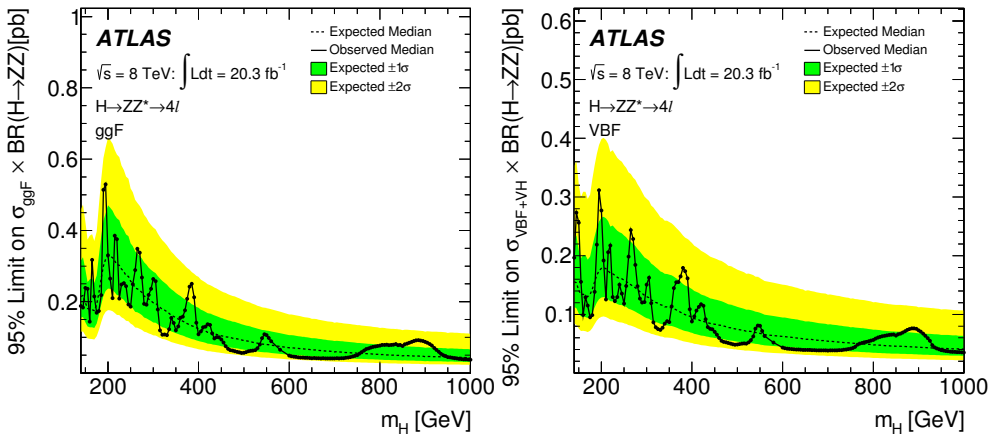

(a) ggF **(b)** VBF+VH

Figure 7.8: Upper limits on the production of an additional heavy Higgs boson. The solid curve shows the observed 95% CL limits on $\sigma \times BR(H \to ZZ)$. The dashed curve shows the expected limit and the coloured bands the 1- and 2-σ ranges around the expected limit. (a) ggF mode. (b) VBF mode.

Chapter 8

Summary

The thesis has presented two physics analyses in four lepton final state and also reconstruction of forward muons. All the data used in the analyses are contained in the 2012 Run 1 ATLAS dataset corresponding to 20.3 fb^{-1}at LHC beam energy of $\sqrt{s}$ = 8 TeV. All the presented results benefit from the exemplary performance of the ATLAS sub-detector systems. For every presented result, additional remarks regarding future prospects are included.

The reconstruction of muons in the forward region $2.5 < |\eta| < 2.7$ of ATLAS was detailed in Chapter 4. The analysis method assumes similar behaviour of muon reconstruction in the neighbouring region of $2.2 < |\eta| < 2.5$ where the full instrumentation of the Muon Spectrometer is used. A comparison between data and MC simulation takes place in these two regions and a double ratio is extracted and used as scale factor on the simulation to match the data behaviour in the forward region. The scale factor varies between ≈ 0.97 to ≈ 1.01, depending on the p_{T} of the forward muon. The MC efficiency of the forward region is calculated in truth level by comparing muons which satisfy selection cuts over all the generated muons in this region. The scale factors are multiplied to the MC efficiency and the reconstruction efficiency of data is extracted, for various p_{T} groups from 10 to 120 GeV) of the forward muons. The data reconstruction efficiency in the forward region is found to be $> 95\%$ for all p_{T} bins. During the Run 2 of ATLAS, the particle flux in the forward region will increase. Therefore, a highly efficient reconstruction would be needed in this region, in order to increase the acceptance of analyses by employing forward muons.

A reconstruction algorithm of non-collinear (far) QED radiation from leptons on $Z \to \ell\ell$ decays was presented in Chapter 5. Photons with angular separation $\Delta R > 0.15$ are selected which pass tight photon identification and have calorimeter cluster transverse energy $E_{\mathrm{T}} > 10GeV$. The far FSR reconstruction has an efficiency of $\approx 60\%$ and purity $> 95\%$. After successful recovery, the photon is added to the dilepton system to correct the measured mass. The correction in the invariant mass of the $\ell\ell\gamma$ system at $Z \to e^+e^-$ and $Z \to \mu^+\mu^-$ decays, shows excellent agreement between data and simulation. The recovery is used in the $H \to ZZ^{(*)} \to 4l$ analysis improving the mass measurement and resolution. Applied on data, 2 out of 30 Higgs

candidates in the signal region (120 - 130 GeV) were corrected due to far FSR. The FSR correction will be essential for the future Higgs studies in the four lepton channel at $\sqrt{s}$ = 13 and $\sqrt{s}$ = 14 TeV. Optimisations on the reconstruction and recovery algorithm could be performed in order to account for the increased pileup at higher luminosities.

A study on the Double Drell-Yan process is presented in Chapter 6. The exclusive cross-section $\sigma_{\mathrm{DPI}\to\mathrm{Z+Z}\to 4\ell}$ was extracted in the phase-space of two Z bosons with masses between 50 - 106 GeV decaying into four leptons (electrons,muons) with $p_{\mathrm{T}} > 3$ GeV and $|\eta|$ ¡ 5. The cross-section was measured $0.74^{+0.51}_{-0.44}(\mathrm{stat.})^{+0.21}_{-0.14}(\mathrm{syst.})$ fb. Due to the large relative uncertainties, an upper limit in the cross-section is set to 1.54 fb . The upper limit is translated into a lower limit for the phenomenological factor $\sigma_{\mathrm{eff}} >$ 0.38 mb. The Double-Drell Yan process was expected to have a negligible impact as background source at the Higgs signal region, with an upper limit of 0.95 events at 95% CL. At the future runs of LHC, a more precise measurement with selection optimisations would be possible. Also, future studies regarding the universality of σ_{eff} would assist for a better understanding of the underlying mechanism of Double Parton Interactions. The real nature and interpratation of σ_{eff} will be a subject of future analyses where more data will become available.

In chapter 7 the search for an additional heavy Higgs boson in the four lepton final state is described. The search was performed in the mass range between 140 - 1000 GeV, assuming SM-like properties for the additional heavy Higgs. No significant excess between data and background-only expectations is observed, therefore upper limits at 95% on cross-section times branching ratio are set. In the gluon-gluon fusion channel, assuming a mass of 200 GeV an upper limit is of 330with an expected limit of 329 fb. For an assumed mass of 1000 GeV the upper limit is 38 fb with an expectation of 43 fb and expected limit 38 fb. In the vector-boson fusion channel, the observed limit is 227 fb, with an expected of 179 fb for a mass of 200 GeV, whereas for 1 TeV the observed limit is 35 fb, with an expected of 41 fb. The difference compared to the background only expectations are is not significant enough in order to indicate the presence of an additional Higgs boson.

At higher energies and luminosities, more data would be available in order to search for an additional heavy Higgs boson. With the new studies it would be possible to investigate extensions of the Standard Model and understand better the role of the low mass SM Higgs boson.

Appendix

List of variables which are used for electron/photon reconstruction and identification:

Type	Description	Particle	Name
Hadronic leakage	Ratio of E_{T} in the first layer of the hadronic calorimeter to E_{T} of the EM cluster (used over the range $\lvert\eta\rvert < 0.8$ or $\lvert\eta\rvert > 1.37$)	e/γ	$\mathrm{R_{Had1}}$
	Ratio of E_{T} in the hadronic calorimeter to E_{T} of the EM cluster (used over the range $0.8 < \lvert\eta\rvert < 1.37$)	e/γ	$\mathrm{R_{Had}}$
Back layer of EM calorimeter	Ratio of the energy in the back layer to the total energy in the EM accordion calorimeter	e/γ	f_3
Middle layer of EM calorimeter	Lateral shower width, $\sqrt{(\Sigma E_i \eta_i^2)/(\Sigma E_i) - ((\Sigma E_i \eta_i)/(\Sigma E_i))^2}$, where E_i is the energy and η_i is the pseudorapidity of cell i and the sum is calculated within a window of 3×5 cells	e/γ	$W_{\eta 2}$
	Ratio of the energy in 3×7 cells over the energy in 7×7 cells centered at the electron cluster position	e/γ	R_η
	Ratio of the energy in 3×3 cells over the energy in 3×7 cells centered at the electron cluster position	e/γ	R_ϕ
Strip layer of EM calorimeter	Shower width, $\sqrt{(\Sigma E_i (i - i_{\mathrm{max}})^2)/(\Sigma E_i)}$, where i runs over all strips in a window of $\Delta\eta \times \Delta\phi \approx 0.0625 \times 0.2$, corresponding typically to 20 strips in η, and i_{max} is the index of the highest-energy strip	e/γ	w_{stot}
	Ratio of the energy difference between the largest and second largest energy deposits in the cluster over the sum of these energies	e/γ	E_{ratio}
	Ratio of the energy in the strip layer to the total energy in the EM accordion calorimeter	e/γ	f_1
	Shower width for three strips around strip with maximum energy deposit	γ	w_{s3}
	Energy outside core of three central strips but within seven strips divided by energy within the three central strips	γ	F_{side}
	Difference between the energy associated with the second maximum in the strip layer, and the energy reconstructed in the strip with the minimal value found between the first and second maxima	γ	ΔE
Track quality	Number of hits in the B-layer (discriminates against photon conversions)	e/γ	n_{Blayer}
	Number of hits in the pixel detector	e/γ	n_{Pixel}
	Number of total hits in the pixel and SCT detectors	e/γ	n_{Si}
	Transverse impact parameter	e/γ	d_0
	Significance of transverse impact parameter defined as the ratio of d_0 and its uncertainty	e/γ	σ_{d_0}
	Momentum lost by the track between the perigee and the last measurement point divided by the original momentum	e/γ	$\Delta p/p$
TRT	Total number of hits in the TRT	e/γ	n_{TRT}
	Ratio of the number of high-threshold hits to the total number of hits in the TRT	e/γ	F_{HT}
Track-cluster matching	$\Delta\eta$ between the cluster position in the strip layer and the extrapolated track	e/γ	$\Delta\eta_1$
	$\Delta\phi$ between the cluster position in the middle layer and the extrapolated track	e/γ	$\Delta\phi_2$
	Defined as $\Delta\phi_2$, but the track momentum is rescaled to the cluster energy before extrapolating the track to the middle layer of the calorimeter	e/γ	$\Delta\phi_{\mathrm{res}}$
	Ratio of the cluster energy to the track momentum	e/γ	E/p
Conversions	Veto electron candidates matched to reconstructed photon conversions	e/γ	isConv

The electron and identification methods use the following variables:

Type	Description	Variable name
	Loose cuts	
Acceptance of the detector	$\|\eta\| < 2.47$	
Hadronic leakage	Ratio of E_T in the first layer of the hadronic calorimeter to E_T of the EM cluster (used over the range $\|\eta\| < 0.8$ and $\|\eta\| > 1.37$) Ratio of E_T in the hadronic calorimeter to E_T of the EM cluster (used over the range $\|\eta\| > 0.8$ and $\|\eta\| < 1.37$)	R_{had1} R_{had}
Second layer of EM calorimeter	Ratio in η of cell energies in 3×7 versus 7×7 cells. Lateral width of the shower.	R_{η} $w_{\eta 2}$
	Medium cuts (includes Loose)	
First layer of EM calorimeter.	Total shower width. Ratio of the energy difference associated with the largest and second largest energy deposit over the sum of these energies	w_{stot} E_{ratio}
Track quality	Number of hits in the pixel detector (≥ 1). Number of hits in the pixels and SCT (≥ 7). Transverse impact parameter (<5 mm).	 d_0
Track matching	$\Delta\eta$ between the cluster and the track (< 0.01).	$\Delta\eta_1$
	Tight cuts (includes Medium)	
b-layer	Number of hits in the b-layer (≥ 1).	
Track matching	$\Delta\phi$ between the cluster and the track (< 0.02). Ratio of the cluster energy to the track momentum Tighter $\Delta\eta$ cut (< 0.005)	$\Delta\phi_2$ E/p $\Delta\eta_1$
Track quality	Tighter transverse impact parameter cut (<1 mm).	d_0
TRT	Total number of hits in the TRT. Ratio of the number of high-threshold hits to the total number of hits in the TRT.	
Conversions	Electron candidates matching to reconstructed photon conversions are rejected	

The electron identification criteria use the following variables:

Table 1: The variables used in the different selections of the electron identification menu.

	Cut-based				Likelihood		
Name	Loose	Medium	Tight	Multilepton	LooseLLH	MediumLLH	VeryTightLLH
$R_{\mathrm{Had(1)}}$	✓	✓	✓	✓	✓	✓	✓
f_3		✓	✓	✓	✓	✓	✓
$W_{\eta 2}$	✓	✓	✓	✓	✓	✓	✓
R_η	✓	✓	✓	✓	✓	✓	✓
R_ϕ					✓	✓	✓
w_{stot}	✓	✓	✓	✓	✓	✓	✓
E_{ratio}	✓	✓	✓	✓	✓	✓	✓
f_1					✓	✓	✓
n_{Blayer}		✓	✓	✓	✓	✓	✓
n_{Pixel}	✓	✓	✓	✓	✓	✓	✓
n_{Si}	✓	✓	✓	✓	✓	✓	✓
d_0		✓	✓			✓	✓
σ_{d_0}						✓	✓
$\Delta p/p$				✓	✓	✓	✓
n_{TRT}		✓	✓	✓			
F_{HT}		✓	✓	✓	✓	✓	✓
$\Delta\eta_1$	✓	✓	✓	✓	✓	✓	✓
$\Delta\phi_2$			✓				
$\Delta\phi_{\mathrm{res}}$				✓	✓	✓	✓
E/p			✓				
isConv			✓				✓

The photon identification methods use the following variables:

Category	Description	Name	Loose	Tight
Acceptance	$\|\eta\| < 2.37$, with $1.37 < \|\eta\| < 1.52$ excluded	–	✓	✓
Hadronic leakage	Ratio of E_{T} in the first sampling of the hadronic calorimeter to E_{T} of the EM cluster (used over the range $\|\eta\| < 0.8$ or $\|\eta\| > 1.37$)	R_{had_1}	✓	✓
	Ratio of E_{T} in the hadronic calorimeter to E_{T} of the EM cluster (used over the range $0.8 < \|\eta\| < 1.37$)	R_{had}	✓	✓
EM Middle layer	Ratio of energies in 3×7 $\eta \times \phi$ cells over 7×7 cells	R_η	✓	✓
	Lateral width of the shower	w_{η_2}	✓	✓
	Ratio of energies in 3×3 cells over 3×7 cells	R_ϕ		✓
EM Strip layer	Shower width calculated from three strips around the strip with maximum energy deposit	$w_{s\,3}$		✓
	Total lateral shower width	$w_{s\,\mathrm{tot}}$		✓
	Energy outside the core of the three central strips but within seven strips divided by energy within the three central strips	F_{side}		✓
	Difference between the energy associated with the second maximum in the strip layer and the energy reconstructed in the strip with the minimal value found between the first and second maxima	ΔE		✓
	Ratio of the energy difference associated with the largest and second largest energy deposits over the sum of these energies	E_{ratio}		✓

Bibliography

[1] *University of Zurich*. http://www.physik.uzh.ch/groups/serra/StandardModel.html. Accessed : 26th October 2015.

[2] S. L. Glashow. Partial-symmetries of weak interactions. *Nuclear Physics* 22.4 (1961), pp. 579 –588.

[3] S. Weinberg. A Model of Leptons. *Phys. Rev. Lett.* 19 (21 1967), pp. 1264–1266.

[4] A. Salam. Weak and electromagnetic interactions (1969). Proc. of the 8th Nobel Symposium on 'Elementary Particle Theory, Relativistic Groups and Analyticity', Stockholm, Sweden, 1968, edited by N. Svartholm, p. 367-377.

[5] D. J. Gross and F. Wilczek. Ultraviolet Behavior of Non-Abelian Gauge Theories. *Phys. Rev. Lett.* 30 (26 1973), pp. 1343–1346.

[6] H. D. Politzer. Reliable Perturbative Results for Strong Interactions? *Phys. Rev. Lett.* 30 (26 1973), pp. 1346–1349.

[7] D. J. Gross and F. Wilczek. Asymptotically Free Gauge Theories. 2. *Phys. Rev.* D9 (1974), pp. 980–993.

[8] D. J. Gross and F. Wilczek. Asymptotically Free Gauge Theories. 1. *Phys. Rev.* D8 (1973), pp. 3633–3652.

[9] E. Noether. Invariant variation problems. *Transport Theory and Statistical Physics* 1 (Jan. 1971), pp. 186–207.

[10] M. Lavelle and D. McMullan. Color charges and the antiscreening contribution to the interquark potential. *Phys. Lett.* B436 (1998), pp. 339–343.

[11] P. W. Higgs. Broken Symmetries and the Masses of Gauge Bosons. *Phys. Rev. Lett.* 13 (1964), pp. 508–509.

[12] F. Englert and R. Brout. Broken Symmetry and the Mass of Gauge Vector Mesons. *Phys. Rev. Lett.* 13 (9 1964), pp. 321–323.

[13] G. S. Guralnik, C. R. Hagen, and T. W. B. Kibble. Global Conservation Laws and Massless Particles. *Phys. Rev. Lett.* 13 (20 1964), pp. 585–587.

[14] Y. Nambu. Quasi-Particles and Gauge Invariance in the Theory of Superconductivity. *Phys. Rev.* 117 (3 1960), pp. 648–663.

[15] J. Goldstone. Field theories with « Superconductor » solutions. English. *Il Nuovo Cimento (1955-1965)* 19.1 (1961), pp. 154–164.

[16] J. Bardeen, L. N. Cooper, and J. R. Schrieffer. Theory of Superconductivity. *Phys. Rev.* 108 (5 1957), pp. 1175–1204.

[17] K. Olive et al. Review of Particle Physics. *Chin.Phys.* C38 (2014), p. 090001.

[18] ATLAS Collaboration. Observation of a new particle in the search for the Standard Model Higgs boson with the ATLAS detector at the LHC. *Phys. Lett.* B716 (2012), pp. 1–29.

[19] LHC Higgs Cross Section Working Group et al. Handbook of LHC Higgs Cross Sections: 3. Higgs Properties. *CERN-2013-004* (CERN, Geneva, 2013).

[20] ATLAS Collaboration. Measurements of Higgs boson production and couplings in diboson final states with the ATLAS detector at the LHC. *Phys. Lett.* B726 (2013). [Erratum: Phys. Lett.B734,406(2014)], pp. 88–119.

[21] A. Hill and J. J. van der Bij. Strongly interacting singlet-doublet Higgs model. *Phys. Rev. D* 36 (11 1987), pp. 3463–3473.

[22] G. C. Branco et al. Theory and phenomenology of two-Higgs-doublet models. *Phys. Rept.* 516 (2012), pp. 1–102.

[23] S. Goria, G. Passarino, and D. Rosco. The Higgs Boson Lineshape. *Nucl. Phys.* B864 (2012), pp. 530–579.

[24] R. P. Feynman. Very High-Energy Collisions of Hadrons. *Phys. Rev. Lett.* 23 (24 1969), pp. 1415–1417.

[25] A. D. Martin et al. Parton distributions for the LHC. *Eur. Phys. J.* C63 (2009), pp. 189–285.

[26] T. Gleisberg et al. Event generation with SHERPA 1.1. *JHEP* 02 (2009), p. 007.

[27] J. R. Gaunt et al. Probing double parton scattering with leptonic final states at the LHC. *2nd International Workshop on Multiple Partonic Interactions at the LHC (MPI@LHC 2010) Glasgow, United Kingdom, November 29-December 3, 2010*. 2011.

[28] C. Kom, A. Kulesza, and W. Stirling. Prospects for observation of double parton scattering with four-muon final states at LHCb. English. *The European Physical Journal C* 71.11, 1802 (2011).

[29] D. Treleani. Double parton scattering, diffraction and effective cross section. *Phys. Rev.* D76 (2007), p. 076006.

[30] K. Golec-Biernat and E. Lewandowska. Electroweak boson production in double parton scattering. *Phys. Rev. D* 90 (9 2014), p. 094032.

[31] ATLAS Collaboration. Measurement of hard double-parton interactions in W$\rightarrow l\nu$ + 2jets events at $\sqrt{s}$ = 7 TeV with the ATLAS detector. *New Journal of Physics* 15.3 (2013), p. 033038.

[32] ATLAS Collaboration. Observation and measurements of the production of prompt and non-prompt Jψ mesons in association with a Z boson in pp collisions at $\sqrt{s}$ = 8 TeV with the ATLAS detector. *The European Physical Journal C* 75.5, 229 (2015).

[33] ATLAS Collaboration. Observation and measurements of the production of prompt and non-prompt J/ψ mesons in association with a Z boson in pp collisions at $\sqrt{s}$ = 8 TeV with the ATLAS detector. *Eur. Phys. J.* C75.5 (2015), p. 229.

[34] S. D. Drell and T.-M. Yan. Massive Lepton-Pair Production in Hadron-Hadron Collisions at High Energies. *Phys. Rev. Lett.* 25 (5 1970), pp. 316–320.

[35] C. Goebel, F. Halzen, and D. M. Scott. Double Drell-Yan Annihilations in Hadron Collisions: Novel Tests of the Constituent Picture. *Phys. Rev.* D22 (1980), p. 2789.

[36] M. Mekhfi. Multiparton processes: An application to the double Drell-Yan mechanism. *Phys. Rev. D* 32 (9 1985), pp. 2371–2379.

[37] M. Diehl, D. Ostermeier, and A. Schafer. Elements of a theory for multiparton interactions in QCD. *JHEP* 03 (2012), p. 089.

[38] L. Evans and P. Bryant. LHC Machine. *Journal of Instrumentation* 3.08 (2008), S08001.

[39] *CERN Accelerator complex*. http://public-archive.web.cern.ch/public-archive/en/research/AccelComplex-en.html. Accessed : 01 June 2015.

[40] S. Chatrchyan et al. Observation of a new boson at a mass of 125 GeV with the CMS experiment at the LHC. *Phys. Lett.* B716 (2012), pp. 30–61.

[41] B Goddard and S Dubourg. *Proceeding of 5th Evian Workshop on LHC beam operation*. Geneva: CERN, 2014.

[42] M. Lamont. Status of the LHC. *Journal of Physics: Conference Series* 455.1 (2013), p. 012001.

[43] ATLAS Collaboration. Measurement of the Inelastic Proton-Proton Cross-Section at $\sqrt{s} = 7$ TeV with the ATLAS Detector. *Nature Commun.* 2 (2011), p. 463.

[44] G. e. a. Antchev. Luminosity-Independent Measurement of the Proton-Proton Total Cross Section at $\sqrt{s} = 8$ TeV. *Phys. Rev. Lett.* 111 (1 2013), p. 012001.

[45] *ATLAS Luminosity Public Results*. https://twiki.cern.ch/twiki/bin/view/AtlasPublic/LuminosityPublicResults. Accessed : 10th September 2015.

[46] A. D. Martin et al. Heavy-quark mass dependence in global PDF analyses and 3- and 4-flavour parton distributions. *Eur. Phys. J.* C70 (2010), pp. 51–72.

[47] http://www.hep.ph.ic.ac.uk/~wstirlin/plots/crosssections2013.jpg. Accessed : 16 September 2015.

[48] ATLAS Collaboration. The ATLAS Experiment at the CERN Large Hadron Collider. *JINST* 3 (2008), S08003.

[49] ATLAS Collaboration. ATLAS: letter of intent for a general-purpose pp experiment at the large hadron collider at CERN. Letter of Intent (1992).

[50] *ATLAS website*. http://www.atlas.ch. Accessed : 04 June 2015.

[51] M. Schott and M. Dunford. Review of single vector boson production in pp collisions at $\sqrt{s} = 7$ TeV. *Eur. Phys. J.* C74 (2014), p. 2916.

[52] http://atlas-computing.web.cern.ch/atlas-computing/links/buildDirectory/AtlasOffline/14.0.0/InstallArea/doc/TrkParameters/html/classTrk_1_1Perigee.html. Accessed : 14 September 2015.

[53] *N. van Eldik, Seminar on Muon Reconstruction*. https://iktp.tu-dresden.de/IKTP/Seminare/IS2012/eldik.pdf. Accessed : 1st September 2015.

[54] W Lampl et al. *Calorimeter Clustering Algorithms: Description and Performance*. Tech. rep. ATL-LARG-PUB-2008-002. ATL-COM-LARG-2008-003. Geneva: CERN, 2008.

[55] *M. Wielers, Talk on Electron Reconstruction and Identification*. https://www.royalholloway.ac.uk/physics/documents/pdf/events/particlephysicsseminars/14-15monikawielers14jan2015.pdf. Accessed : 1st September 2015.

[56] ATLAS Collaboration. Electron reconstruction and identification efficiency measurements with the ATLAS detector using the 2011 LHC proton–proton collision data. English. *The European Physical Journal C* 74.7, 2941 (2014).

[57] Electron efficiency measurements with the ATLAS detector using the 2012 LHC proton-proton collision data. ATLAS-CONF-2014-032 (2014).

[58] *Measurements of the photon identification efficiency with the ATLAS detector using 4.9 fb−1 of pp collision data collected in 2011*. Tech. rep. ATLAS-CONF-2012-123. Geneva: CERN, 2012.

[59] Measurement of the muon reconstruction performance of the ATLAS detector using 2011 and 2012 LHC proton–proton collision data. English. *The European Physical Journal C* 74.11, 3130 (2014).

[60] M. Cacciari, G. P. Salam, and G. Soyez. The Anti-k(t) jet clustering algorithm. *JHEP* 04 (2008), p. 063.

[61] ATLAS Collaboration. Jet energy measurement with the ATLAS detector in proton-proton collisions at $\sqrt{s}$ = 7 TeV. *Eur. Phys. J.* C73.3 (2013), p. 2304.

[62] http://cms.web.cern.ch/news/jets-cms-and-determination-their-energy-scale. Accessed : 1st September 2015.

[63] ATLAS Collaboration. Reconstruction and Calibration of Missing Transverse Energy and Performance in Z and W events in ATLAS Proton–Proton Collisions at $\sqrt{s}$ = 7 TeV (2011).

[64] ATLAS Collaboration. Search for strong production of supersymmetric particles in final states with missing transverse momentum and at least three b-jets at $\sqrt{s}$ = 8 TeV proton–proton collisions with the ATLAS detector. *JHEP* 1410 (2014), p. 24.

[65] S. Agostinelli et al. GEANT4: A simulation toolkit. *Nucl. Instrum. Meth.* A 506 (2003), pp. 250–303.

[66] ATLAS Collaboration. The ATLAS Simulation Infrastructure. English. *The European Physical Journal C* 70.3 (2010), pp. 823–874.

[67] ATLAS Collaboration. Measurement of the Higgs boson mass from the $H \to \gamma\gamma$ and $H \to ZZ^* \to 4\ell$ channels in pp collisions at center-of-mass energies of 7 and 8 TeV with the ATLAS detector. *Phys. Rev. D* 90 (5 2014), p. 052004.

[68] D Kyriazopoulos. *Performance of the muon identification and reconstruction with the ATLAS detector*. "https://cds.cern.ch/record/1743595". 2014.

[69] T. Melia et al. W^+W^-, WZ and ZZ production in the POWHEG BOX. *JHEP* 1111 (2011), p. 078.

[70] H.-L. Lai et al. New parton distributions for collider physics. *Phys. Rev.* D 82 (2010), p. 074024.

[71] S. Dittmaier and M. Huber. Radiative corrections to the neutral-current Drell-Yan process in the Standard Model and its minimal supersymmetric extension. *JHEP* 01 (2010), p. 060.

[72] R. K. Ellis, W. J. Stirling, and B. R. Webber. *QCD and Collider Physics*. Cambridge Books Online. Cambridge University Press, 1996.

[73] Reconstruction of collinear final-state-radiation photons in Z decays to muons in sqrts=7 TeV proton-proton collisions. (2012).

[74] M. L. Mangano et al. ALPGEN, a generator for hard multiparton processes in hadronic collisions. *JHEP* 07 (2003), p. 001.

[75] H.-L. Lai et al. New parton distributions for collider physics. *Phys. Rev.* D 82 (2010), p. 074024.

[76] T. Sjöstrand, S. Mrenna, and P. Skands. A brief introduction to {PYTHIA} 8.1. *Computer Physics Communications* 178.11 (2008), pp. 852 –867.

[77] P. Z. Skands. Tuning Monte Carlo Generators: The Perugia Tunes. *Phys. Rev.* D82 (2010), p. 074018.

[78] P. Golonka and Z. Was. PHOTOS Monte Carlo: A Precision tool for QED corrections in Z and W decays. *Eur. Phys. J.* C 45 (2006), pp. 97–107.

[79] ATLAS Collaboration. *Measurements of the properties of the Higgs-like boson in the four lepton decay channel with the ATLAS detector using 25 fb−1 of proton-proton collision data*. Tech. rep. ATLAS-CONF-2013-013. Geneva: CERN, 2013.

[80] J Alison et al. *Description and Performance of the Electron Likelihood Tool at ATLAS using 2012 LHC Data*. Tech. rep. ATL-COM-PHYS-2013-378. Geneva: CERN, 2013.

[81] Updated results and measurements of properties of the new Higgs-like particle in the four lepton decay channel with the ATLAS detector (2012).

[82] Measurements of the properties of the Higgs-like boson in the four lepton decay channel with the ATLAS detector using 25 fb−1 of proton-proton collision data (2013).

[83] N. Paver and D. Treleani. Multiquark scattering and large-pT jet production in hadronic collisions. English. *Il Nuovo Cimento A* 70.3 (1982), pp. 215–228.

[84] http://home.thep.lu.se/~torbjorn/pythia81html/ASecondHardProcess.html. Accessed : 4th December 2015.

[85] ATLAS Collaboration. *Summary of ATLAS Pythia 8 tunes*. Tech. rep. 2012.

[86] http://gg2VV.hepforge.org/.

[87] ATLAS Collaboration. Search for an additional, heavy Higgs boson in the $H \to ZZ$ decay channel at $\sqrt{s} = 8$ TeV in pp collision data with the ATLAS detector. *Eur. Phys. J.* C76.1 (2016), p. 45.

[88] LHC Higgs Cross Section Working Group et al. Handbook of LHC Higgs Cross Sections: 2. Differential Distributions. *CERN-2012-002* (CERN, Geneva, 2012).

[89] K. S. Cranmer. Kernel estimation in high-energy physics. *Comput. Phys. Commun.* 136 (2001), pp. 198–207.

[90] G. Cowan et al. Asymptotic formulae for likelihood-based tests of new physics. English. *The European Physical Journal C* 71.2, 1554 (2011).

[91] A. L. Read. Presentation of search results: the CL s technique. *Journal of Physics G: Nuclear and Particle Physics* 28.10 (2002), p. 2693.

[92] J. M. Campbell, R. K. Ellis, and C. Williams. Vector boson pair production at the LHC. *JHEP* 07 (2011), p. 018.

[93] M. W. Krasny and W. Placzek. The LHC excess of four-lepton events interpreted as Higgs-boson signal: Background from Double Drell-Yan process? *Acta Phys. Polon.* B45.1 (2014), pp. 71–87.

[94] B. P. Roe et al. Boosted decision trees as an alternative to artificial neural networks for particle identification. *Nuclear Instruments and Methods in Physics Research A* 543 (May 2005), pp. 577–584.

[95] F. Cascioli et al. ZZ production at hadron colliders in NNLO QCD. *Phys. Lett.* B735 (2014), pp. 311–313.

[96] S. Gieseke, T. Kasprzik, and J. H. Kühn. Vector-boson pair production and electroweak corrections in HERWIG++. *Eur. Phys. J.* C74.8 (2014), p. 2988.

[97] J. Alwall et al. MadGraph/MadEvent v4: The New Web Generation. *JHEP* 09 (2007), p. 028.

[98] ATLAS Collaboration. Constraints on the off-shell Higgs boson signal strength in the high-mass ZZ and WW final states with the ATLAS detector. *The European Physical Journal C* 75.7, 335 ().

[99] M. Baak et al. *Interpolation between multi-dimensional histograms using a new non-linear moment morphing method*. Tech. rep. CERN-OPEN-2014-050. NIMA57112. Geneva: CERN, 2014.

[100] M. Bonvini et al. Signal-background interference effects for $gg \to H \to W^+W^-$ beyond leading order. *Phys. Rev.* D88.3 (2013), p. 034032.

[101] G. Passarino. Higgs CAT. *Eur. Phys. J.* C74 (2014), p. 2866.